# HIDRAULICA

HYDRAULICS-PNEUMATICS-TRIBOLOGY-ECOLOGY-SENSORICS-MECHATRONICS

2023
March
No. 1

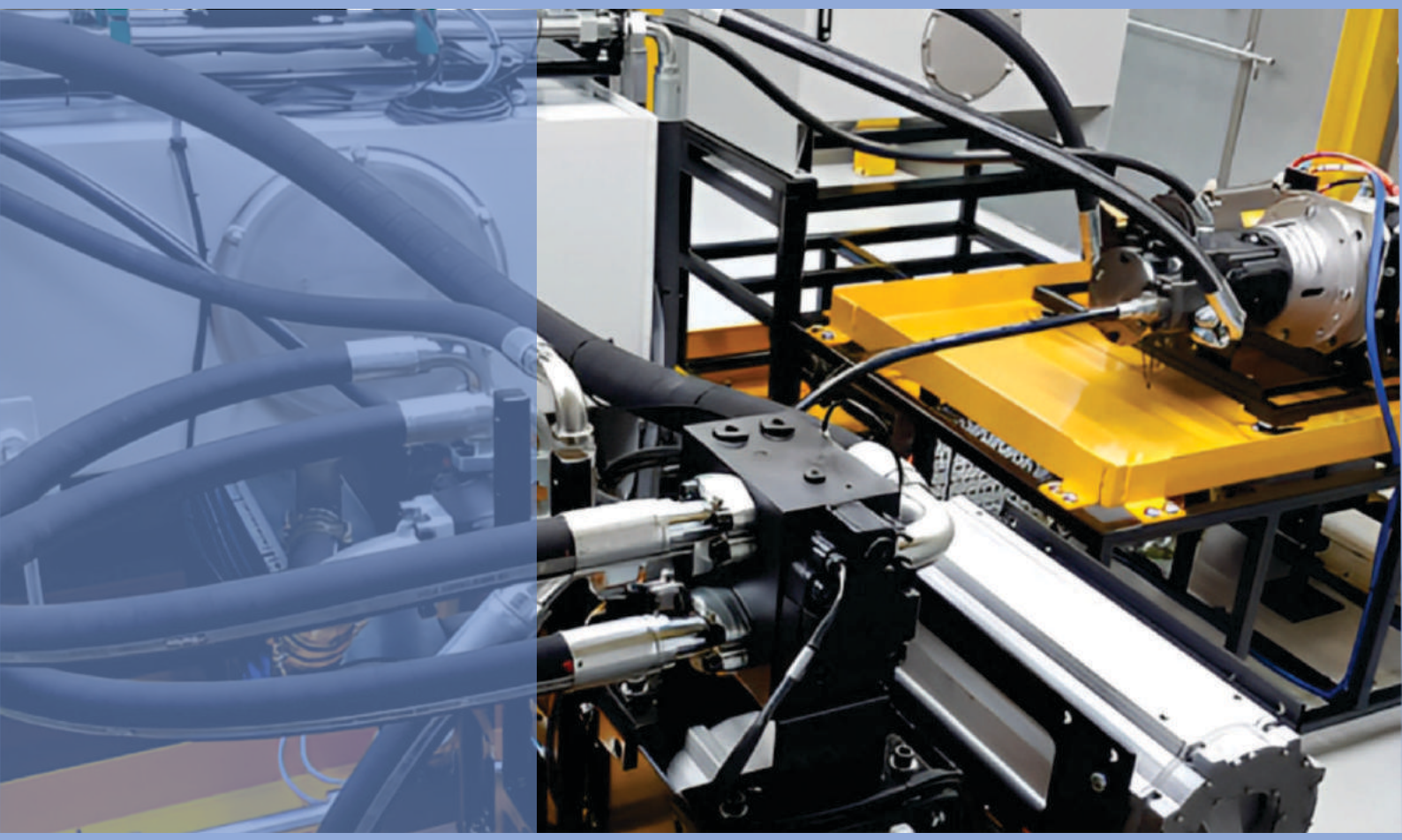

ISSN 1453 - 7303
ISSN-L 1453 - 7303

https://hidraulica.fluidas.ro

## CONTENTS

***Published by:***
***Hydraulics and Pneumatics Research Institute, Bucharest-Romania***
Address: 14 Cuţitul de Argint, district 4, Bucharest, 040558, Romania
Phone: +40 21 336 39 91; Fax: +40 21 337 30 40; e-Mail: ihp@fluidas.ro; Web: www.ihp.ro
***with support from:***
***National Professional Association of Hydraulics and Pneumatics in Romania - FLUIDAS***
e-Mail: fluidas@fluidas.ro; Web: www.fluidas.ro

**HIDRAULICA Magazine** is indexed by international databases

**ISSN 1453 – 7303; ISSN – L 1453 – 7303**

## EDITORIAL

# Îmbătrânirea cercetării - avantaj, dezavantaj sau fără importanță?

Dr. Ing. Petrin DRUMEA
DIRECTOR PUBLICAȚIE

În ultimii ani se constată o permanentă creștere a vârstei medii a lucrătorilor din cercetare, problemă pe care am evitat să o discut până acum, dată fiind situația în care mă aflu și eu, ca angajat într-o unitate de cecetare, deși am depășit vârsta pensionării. Analizând câteva din situațiile pe care le cunosc, pot face câteva aprecieri, care cu siguranță nu reprezintă un adevăr absolut ci doar o variantă parțială a unei realități puțin discutate cu seriozitate.

Prima situație este că multe din temele noi care apar în programele de cercetare sunt propuse și conduse de persoane cu vârste de peste 50 de ani. Același lucru se verifică și în zona brevetelor de invenție.

A doua situație este că se constată că majoritatea tinerilor specialiști se simt foarte bine când își verifică ideile cu specialiști în vârstă și nu cu tineri sau cu specialiști cu vârste medii (30-50 de ani).

O a treia situație este că în domeniul cercetării aplicative firmele beneficiare doresc, de obicei, să discute cu persoane mai în vârstă aproape toate datele activităților comune și, mai ales, ale activităților referitoare la asimilarea produselor.

O a patra situație este că se constată că specialiștii în vârstă sunt mai disciplinați și mai prezenți la locul de muncă, deși uneori sănătatea le creează anumite probleme.

Mai sunt și alte elemente care ne indică existența unei probleme a îmbătrânirii cercetării, dar pentru o primă analiză sunt suficiente situațiile prezentate.

În aceste condiții, problema care s-a pus - dacă este rău sau nu faptul că vârsta cercetătorilor a crescut semnificativ - poate căpăta un prim răspuns. Acesta - care poate fi o primă concluzie a mea - este că existența în cercetare a persoanelor în vârstă este binevenită, cu condiția existenței unui număr de specialiști tineri suficient de mare care să permită o funcționare corectă a unei unități viabile. Avantajul de a avea niște specialiști experimentați trebuie folosit cu mare atenție pentru a nu se transforma în dezavantaj prin eliminarea tinerilor din zonele de decizie. Este extrem de important ca soluțiile și ideile tinerilor să fie acceptate și luate în considerare, chiar dacă au nevoie de unele intervenții de corectare și îmbunătățire.

În final, trebuie făcută precizarea că nu vârsta specialiștilor, ci lipsa fondurilor suficiente poate distruge cercetarea și, ca urmare, perspectivele de dezvoltare.

## EDITORIAL

### Research is getting old - Is it an advantage, a disadvantage, or is it irrelevant?

Ph.D.Eng. Petrin DRUMEA
MANAGING EDITOR

In recent years there has been a permanent increase in the average age of research workers, a problem I have avoided discussing until now, given the situation I find myself in, as an employee in a research unit, although I am past retirement age. Analyzing several situations I know, I can make some judgments, which certainly do not represent the absolute truth, but are merely a partial version of a reality that is rarely addressed in a serious manner.

The first situation is that many of the new topics emerging under research programmes are proposed and managed by people aged over 50 years. The same can be noted in the area of patents.

The second situation is that it has been found that most young specialists feel very comfortable when they check their ideas with older specialists and not with young or middle-aged (30-50 years old) specialists.

A third situation is that in the field of applied research the beneficiary companies usually like to discuss with older people almost all the data of the joint activities, and, above all, the details of the activities related to the assimilation of the products.

A fourth situation is that older specialists are found to be more disciplined and present at work, although sometimes they face certain health issues.

There are other elements, too, that point to an issue related to the aging of research specialists, but for a first analysis, the above-mentioned situations could serve.

Under these circumstances, the question that has been raised - whether it is bad or not that the age of research specialists has increased significantly - can get a first answer. This answer - which could be a first conclusion of mine - is that the presence of older people in the field of research is welcome, provided there are a large enough number of young specialists to allow a viable unit to function properly. The advantage of having experienced specialists must be used very carefully so as not to turn the situation into a disadvantage by casting out young people from decision-making areas. It is extremely important that young people's solutions and ideas are accepted and taken into account, even if sometimes they need adjustment and improvement interventions.

Finally, it should be stated that it is not the age of specialists, but the lack of sufficient funds that can destroy research and, as a result, the prospects for development.

# Influence of Temperature Variations on the Operating Characteristics of the Hydro-Pneumatic Accumulators

Prof. PhD Eng. **Anca BUCUREȘTEANU**[1,*]

[1] University POLITEHNICA of Bucharest
* ancabucuresteanu@gmail.com

***Abstract:*** *In this paper, the authors present the mathematical models that can be used to determine the correlation between the variations of temperature and pressure in the industrial hydraulic units equipped with hydro-pneumatic accumulators. Two real cases of utilization of these systems are shown. First of all, the hydraulic units in which the oil volume in the accumulator circuit is negligible (as in the case of machine-tools and constructions equipment) are presented. The second case is the one of the units where the oil volume in the accumulator circuit is much higher than the accumulator volume, as in the case of the heavy-duty hydraulic presses, for example.*

***Keywords:*** *Hydro-pneumatic accumulators, heating of hydraulic units, mathematical models*

## 1. Introduction

Accumulators are hydraulic components that allow the reception, storage and transmission of the hydrostatic energy in the form of volumes of oil under pressure [1, 2, 3].
The low degree of compressibility of the liquids makes it difficult to store energy in small volumes, but allows the transmission of high efforts. Unlike liquids, gases have great possibilities in terms of compressibility, which enable them to store large energies in small volumes. The association of liquids and gases within special constructions led to the making of hydro-pneumatic accumulators.
Diaphragm or bladder accumulators achieve a perfect gas - liquid separation.
For small volumes of liquid (less than 10 l), the separation is made by a flexible rubber diaphragm placed between the two chambers of the accumulator as in Figure 1.

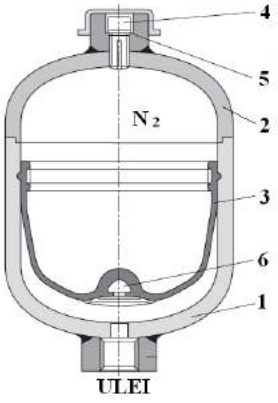


**Fig. 1.** Hydro-pneumatic accumulator with diaphragm

The following denotations were used in the figure above: 1 and 2 represent two parts that determine (by welding) the total volume of the accumulator; 3 – diaphragm; 4 and 5 - elements through which the nitrogen loading is performed. To prevent extrusion at total emptying, there is a metal part 6 in the center of the diaphragm.
The material of the diaphragm must meet specific requirements, like: to be resistant to oil and gas, to be less sensitive to wear and tear, less sensitive to fatigue, to have good elasticity.
The advantages of using this type of accumulator are the following ones: there are no frictional forces; the sealing is perfect; it is possible to operate at pressure of 500 - 600 daN/cm$^2$.

Disadvantages include: firstly, the reduced capacity and secondly the fact that the elastomer cannot be used at temperatures below 25 $^0$C.
If a bladder made of the same material is used instead of the diaphragm, the volume of the accumulator increases a lot, reaching volumes larger than 50 l. Such an accumulator is shown in Figure 2 and is formed of: 1 - one-piece body; 2 - bladder; 3 – nitrogen charging valve; 4 - shut-off valve.

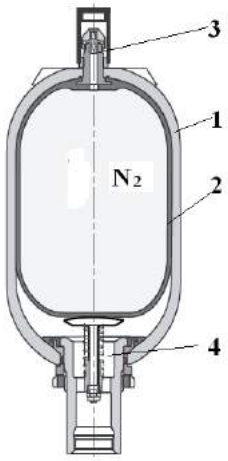


**Fig. 2.** Hydro-pneumatic accumulator with bladder

The liquid passes from the accumulator to the hydraulic unit and inversely through the holes under the valve 4. In the case of a complete discharge of the accumulator, the valve 4 protects against the extrusion of the bladder and does not allow the clogging of the accumulator inside part.
The installation of the accumulator (or accumulators in parallel) is usually done according to the diagram in Figure 3.

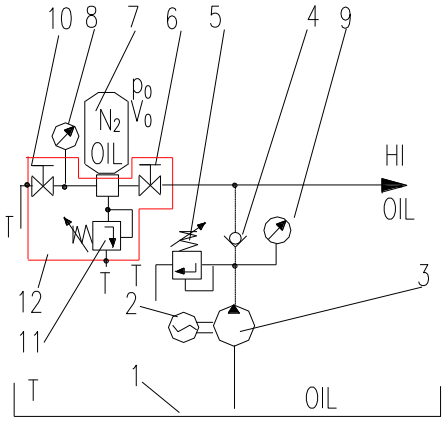


**Fig. 3.** Installing the accumulator

Pump 3, driven by the electric motor 2, sucks the oil from the tank 1 (T). The oil is sent to the hydraulic unit IH but also to the accumulator 7 via the check valve 4. This valve does not allow the accumulator to be discharged through the pump. The maximum pressure in the unit is adjusted by means of the pressure valve 5. The oil enters the accumulator through the valve 6. The supply pressure (at the pump) is displayed on the manometer 9, while the pressure in the accumulator is displayed on the manometer 8. For the discharge of the accumulator, the valve 10 should be opened. As shown below, it is preferable to have also a safety valve 11, set at a pressure value higher than the pressure of the valve 5. In most cases, the elements 6, 8, 10 and 11 are mounted on a block 12, called a safety block.

Accumulator 7 has the volume $V_0$ and is charged with nitrogen at the pressure $p_0$, this one depending on its role in the unit [2, 3]. If the unit operates at a pressure ranging from the minimum value ($p_m$) and the maximum value ($p_M$), then the volume of nitrogen will evolve accordingly between the maximum value ($V_M$) and the minimum value ($V_m$). Under these limitations, at any moment, if the ambient temperature t does not change, the nitrogen has volume V and pressure p so that the conditions are met:

$$p_0 V_0 = p_M V_m \tag{1}$$

$$p_M V_m^n = p V^n = p_m V_M^n \tag{2}$$

Relation (1) represents the first charge of the accumulator in the circuit, considered as isothermal.
Relations (2) describe the transformations of nitrogen between its states. In the case of nitrogen, the polytropic coefficient n changes between the values 1 at the isothermal transformation and 1.4 at the adiabatic transformation [3, 4].
The transformations undergone by nitrogen, in conformity with the relations above, were represented in Figure 4.

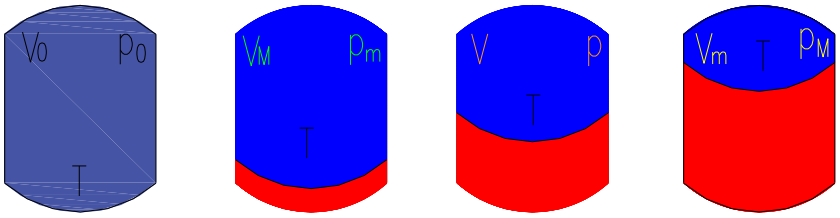


a. b. c. d.

**Fig. 4.** Nitrogen state transformations

Initially,according to Figure 4a, the nitrogen at pressure $p_0$ takes the entire available volume $V_0$. When the minimum pressure $p_m$ is reached, the occupied volume is the maximum one $V_M$, as in Figure 4b. At any time during operation, the nitrogen is characterized by pressure p and fills the volume V, according to Figure 4c. When the maximum value of the pressure $p_M$ is reached, as in Figure 4d, the volume of nitrogen has the minimum value $V_m$.

## 2. Heating of the Hydraulic Units – the Cause of the Pressure Increasein the Units Equipped with Hydro-pneumatic Accumulators

### 2.1 Hydraulic Units with a Negligible Volume of Oil in the Accumulator Circuit

A unit with accumulator that supplies small consumers (cylinders) through pipes of negligible volume is taken into consideration. In the case of a unit for tool clamping/unclamping or saddle locking/unlocking, if the accumulator is in the state shown in Figure 4c, the pressure increases after a while (as indicated by the manometer of the accumulator) because of the heating, even if the pressure at the pump is zero, such as in the case of the pre-control systems [3, 5].
For the gas in the accumulator, if the expansionsof the accumulator, pipes and oil are neglected, it can be considered:

$$\frac{pV}{T} = \frac{(p+\Delta p)(V+\Delta V)}{T+\Delta T} \tag{3}$$

In the relation (3) it was denoted: ΔV - variation of the gas volume; ΔT - increase of temperature and Δp - increase of pressure.
From the relation (3) it is obtained:

$$\Delta p = p\left(\frac{\Delta T}{T} - \frac{\Delta V}{V}\right) \tag{4}$$

When the oil is considered incompressible ($E_{Oil} \rightarrow \infty$, where $E_{Oil}$ represents the modulus of elasticity of oil), for the gas it can be considered that this one undergoes an isochoric transformation, reaching the state shown infigure 5.

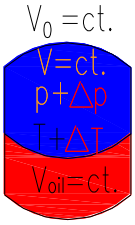


**Fig. 5.** Isochoric transformation due to temperature increase if oil compressibility is neglected

In this case, the pressure increase Δp will be:

$$\Delta p = p\frac{\Delta T}{T} \tag{5}$$

If the oil compressibility is taken into account, the gas no longer undergoes a constant volume transformation, increasing its volume by the quantity ΔV equal to the compression of oil, as shown in Figure 6.

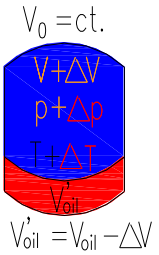


**Fig. 6.** Gas transformation due to temperature increase if oil compressibility is not neglected

In this case, from the relations above it is obtained:

$$\Delta p = \frac{p}{1+\frac{p(V_0-V)}{E_{Oil}V}}\frac{\Delta T}{T} \tag{6}$$

To see the influence of oil compressibility on the variation of pressure, the following example was taken into consideration: $V_0$ = 10 l, $p_0$ = 90 bar, $p_M$ = 200 bar, $p_m$ = 100 bar, $T_0$ = 293 K (20$^0$C), increase of temperature ΔT = 40 $^0$C. The heating started when p = $p_M$, the circuit is without losses and the modulus of elasticity of the oil is $E_{Oil}$ = 1.5 x $10^4$ daN/cm$^2$. If the compressibility is not taken into consideration, Δp = 27.3 bar is obtained. By compressing the oil, the nitrogen occupies a larger volume, in which case the over pressure Δp = 26.86 bar. Therefore, there is a difference of ~0.5 bar or ~2%, which can be neglected, because it is an error that does not impede operation in most cases; moreover, it is even imperceptible on the usual manometers.
If it is considered that Δp ~ 25 bar at a reference pressure of 200 bar, an increase of over 10% can be noticed, which is not negligible at all.
In general, in the case of machine-tools, the equipment used for such units operates at pressures of 300 bar at the most.
Under these conditions and taking into account the relations above mentioned, the characteristic of the over pressure Δp can be drawn as a function of the temperature increase ΔT like in Figure 7.
The reference temperature is t = 20 $^o$C (293 K) and there are not allowedoil temperatures higher than $t_{Max}$ = 60 $^o$C (333K), which means a maximum heating of Δt = 40 $^o$C.

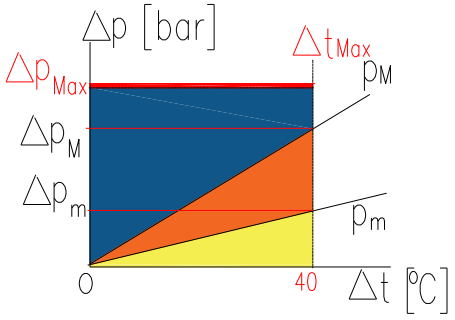


**Fig. 7.** Characteristic of the over pressure Δp

Another condition imposed in Figure 7 is the one regarding the working pressures: the maximum working pressure $p_M$ added to the pressure increase Δp must not exceed the maximum pressure allowed by the equipment, $p_{Max}$, which means:

$$\Delta p_{Max} \leq p_{Max} - p_M \tag{7}$$

The heating of the unit occurs with the accumulator at a pressure p which validates:

$$p_m \leq p \leq p_M \tag{8}$$

Under these conditions, according to the characteristic in Figure 7, it results:

$$\Delta p \in [\Delta p_m, \Delta p_M] \tag{9}$$

If the pressure increase Δp is higher than $\Delta p_{Max}$ there is the risk of destruction of some components because the pressure valve 5 in Figure 3 does not affect the circuit of the accumulator which heats up and is isolated by the check valve 4. The safety block 12 was provided to protect the circuit. This block includes the pressure valve 11 which is set to the necessary value that is higher than the one set at the pressure valve 5. Figure 8 shows a safety block in which the accumulator is coupled/uncoupled manually.

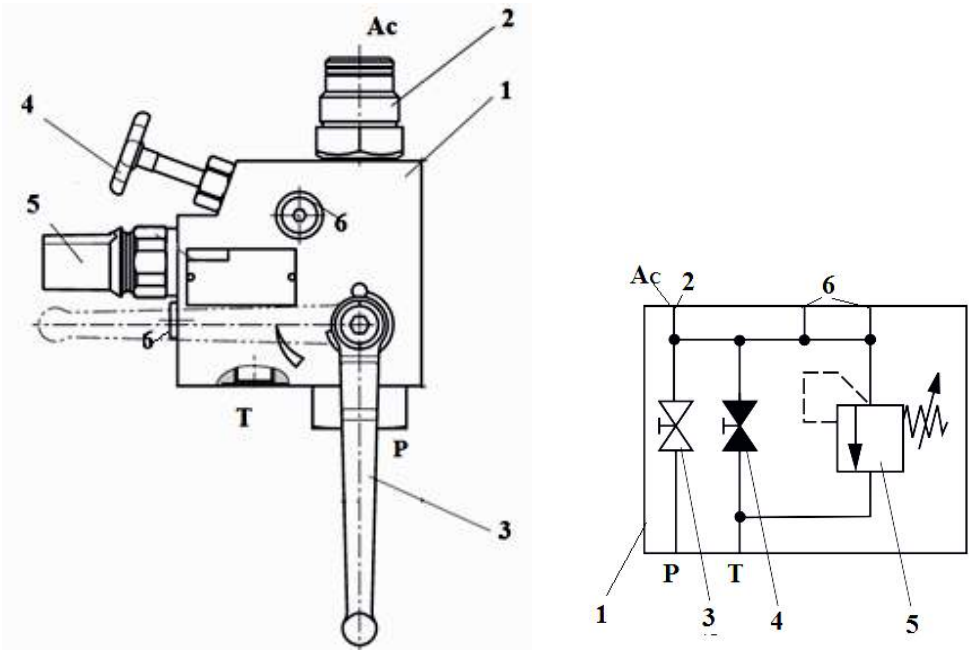


**Fig. 8.** Manually operated safety block

The fitting 2 for the accumulator Ac is fixed in body 1. The lever 3 makes the coupling and uncoupling of the accumulator to the source (P). Valve 4 discharges the accumulator directly to the tank (T). The intended pressure is set at pressure valve 5. Pressure value can be read on a manometer connected to any of the fittings 6.
The safety block eliminates the risks resulted from the pressure increase caused by the heating. A simulation of the running of a system with and without safety block was used to show how the safety block operates [6, 7]. The results of the simulation are presented in Figure 9.

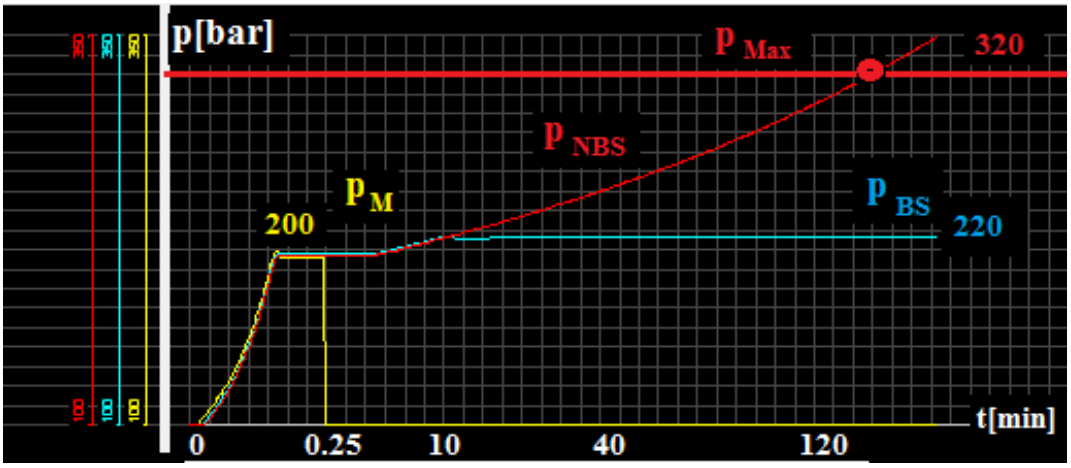


**Fig. 9.** Simulation of the operation of a system with and without safety block

It was considered that a constant flow pump supplies alternatively two circuits with accumulator at the maximum pressure $p_M$ = 200 bar. The circuits are equipped with pre-control systems [1, 3, 8] which discharge the pump to the tank when maximum pressure is reached. One circuit is provided with safety block adjusted to the safety pressure $p_{BS}$ = 220 bar. The second circuitis not equipped with safety block and the pressure $p_{NBS}$ develops in the accumulator. The maximum pressure allowed by the componentsis $p_{Max}$ = 320 bar. In the case of the circuit provided with safety block, the valve ensures the discharge when the pressure value $p_{BS}$ = 220 bar is reached after approximately 10 minutes of operation, but in the circuit without block it is noticed that after about 150 minutes the risk of unit destruction occurs.

### 2.2 Hydraulic Units with Large Volume of Oil in the Circuit of the Accumulator

This time, a unit with accumulator that supplies big consumers (cylinders) through large DN pipes is taken into consideration. For example, a unit from a heavy press. In this case, if the accumulator is in the state shown in Figure 10a, after a while it is observed that the pressure increases at the manometer of the accumulator due to heating, even if the manometer of the pumps hows that the pressure is zero; because of the heating, it will be reached the state in Figure 10b.

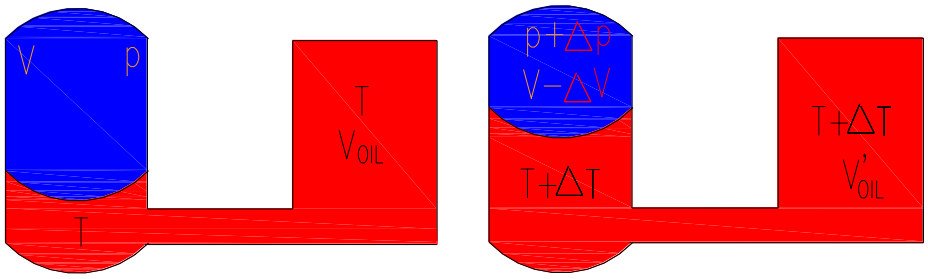


a. b.

**Fig. 10.** Increase of the pressure due to oil heating in a circuit with accumulator

By heating, the large amount of oil expands and reduces the volume of nitrogen in the accumulator, increasing its pressure. It is considered that the oil is incompressible and its expansion is done by compressing the gas [3, 8]. The expansion of the accumulator is neglected. Consider the initial volume of oil $V_{Oil}$ at temperature T. After its heating, the volume becomes$V'_{Oil}$. In these conditions, the following relations are found out:

$$\frac{pV}{T} = \frac{(p+\Delta p)(V-\Delta V)}{T+\Delta T} \tag{10}$$

$$\Delta p = p\left(\frac{\Delta T}{T} + \frac{\Delta V}{V}\right) \tag{11}$$

$$\Delta V = V'_{Oil} - V_{Oil} \tag{12}$$

$$V'_{Oil} = V_{Oil}(1 + \gamma_{Oil}\Delta T) \tag{13}$$

In the above relation, $\gamma_{Oil}$ denotes the coefficient of volume expansion of the oil ($\gamma_{Oil}$ = 0.00065 $K^{-1}$). Finally, the value of overpressure is obtained as:

$$\Delta p = p\frac{\Delta T}{T}\left(1 + \frac{V_{Oil}T\gamma_{Oil}}{V}\right) \tag{14}$$

Relation (14) can be approximated with the expression:

$$\Delta p = p\frac{\Delta T}{T}\left(1 + p\frac{V_{Oil}T\gamma_{Oil}}{V_0 p_0}\right) \tag{15}$$

In this case, the pressure increase has, in addition to the component given by the heating of the nitrogen, another term proportional to the volume of heated oil. Thus, for a volume of oil $V_{oil}$ + 20 l heated with Δt = 40 °C, starting from the maximum pressure $p_M$ = 200 bar, a final pressure higher than 250 bar is reached. The pressure increase can influence the value of the charging/discharging times of the accumulators [9].

## 3. Conclusions

The hydro-pneumatic accumulators are used in most hydraulic units of machine-tools: counter balance units, locking/unlocking systems, clamping/unclamping systems and even the hydrostatic lubrication systems. In most cases, the accumulator sizing or checking calculation is made considering the ambient temperature as constant and, in this situation, the gas undergoes isothermal or adiabatic transformations. In reality, the temperature of the hydraulic environment and also the temperature of the unit is not constant. During operation, the temperature rises, so that in some cases it is even necessary to provide cooling systems. Usually, for machine-tools the reference temperature of the environment is 20 $^0$C, while the maximum temperature allowed in the hydraulic units does not exceed 60 $^0$C. Therefore, theoretically, the heating by 40 $^0$C is possible. This heating affects the gas state transformations in the accumulator, but can also entail large variations in the volume of oil. All this can lead to significant increases of the pressure in the unit that can exceed the value set at the pressure valve, causing the destruction of the unit. In these conditions, it is recommended (in addition to the usual calculations) to check also the overpressure that appears because of the heating. The usual accumulators work at 320 bar at the most, but there are also special accumulators that can operate up to 700 bar.
To protect the systems with accumulators, it is appropriate to use safety blocks manufactured by specialized companies. The pressure valves in these safety blocks must be set at values that do not endanger the unit. These values will be higher than the pressures developed during operation. It is recommended to limit the access to these valves and even to seal them.
The use of the simulation programs for checking the operation of the unit in the design stage is very helpful.

**References**

[1] Prodan, Dan. *Hydraulics of Production Systems/Hidraulica sistemelor de productie*. Bucharest, Printech Publishing House, 2011.
[2] ***. HYDAC, FOX, PARKER, and BOSCH REXROTH Catalogues and leaflets.
[3] Bucureşteanu, Anca. *Hydro-Pneumatic Accumulators. Use and Modeling/Acumulatoare pneumohidraulice. Utilizare si modelare*. Bucharest, Printech Publishing House, 2001.
[4] Moran, Michael J., Howard N. Shapiro, Daisie D. Boettner, and Margaret B. Bailey. *Fundamentals of Engineering Thermodynamics*. Wiley John Wiley & Sons, Inc., U.S.A, 2012.
[5] Prodan, Dan, Emilia Balan, and Anca Bucureşteanu. "Machine-Tools Hydraulic Systems for Tool-Holders Clamping-Unclamping." *Academic Journal of Manufacturing Engineering (AJME)*, no. 1 (March 2013): 102-107.
[6] Prodan, Dan. *Machine Tools. Modeling and Simulation of Hydrostatic Elements and Systems/Maşini-Unelte. Modelarea şi Simularea Elementelor şi Sistemelor Hidrostatice*. Bucharest, Printech Publishing House, 2006.
[7] ***. AUTOMATION STUDIO Software package.
[8] Guibert, Ph. *Applied Industrial Hydraulics/Hydraulique industrielle appliquee*. Université de Metz, 1991.
[9] Prodan, Dan, and Anca Bucureşteanu. "Determining the Times of Charging and Discharging of Hydro-pneumatic Accumulators." *Hidraulica Magazine*, no. 1 (March 2017): 14-20.

# Research on the Behaviour of a Toroidal LPG Storage Tank under Uniaxial Traction Loads

Assistant professor PhD. Eng. **Petre OPRIŢOIU**[1,*]

[1] Technical University of Cluj-Napoca, Department of MTC, Observatorului Street, no. 72-74, Cluj-Napoca, 400363, Cluj county, Romania.

* petre.opritoiu@mtc.utcluj.ro

***Abstract:*** *A numerical model has been developed to reproduce the uniaxial traction loads on the three-dimensional (3-D) geometry of a hexagonal toroid with regular hexagonal cross-section used in the manufacturing of liquefied petroleum gas (LPG) storage tanks from the automotive industry. Several numerical applications are presented, with an optimization procedure, addressing the influence of affecting factors (temperature, corrosion and traction loads). Internal state stress and strains were also modeled using the finite-element method (FEM). The obtained results highlight the effectiveness of the proposed approach in correlating LPG) storage tank structure with external traction loads. The relationship between the strains, stresses, and the applied traction load noticeably deviates from linearity. This approach based on the FEM method can improve the simulation accuracy and to fully explore the design parameters (size, weight, shape, materials, mechanical properties, etc.) of the product early in the development process, while greatly reduce the computing cost.*

***Keywords:*** *3-D hexagonal toroidal LPG fuel tank, automotive industry, industrial engineering design, optimization methods*

## 1. Introduction

Over the past two decades, the current reality of the global competitive market has forced many companies to apply Computer-aided design (CAD) / Computer-aided manufacturing (CAM) systems [1-3] to become more efficient and to develop innovative solutions [4-6], in manufacturing of a high-quality product [7-9].
In storage tanks, manufacturing a well-designed production process based on the optimization techniques is applied to increase productivity and improve quality [10, 11].
To simulate complex parametric models of storage tanks [12-14], which work under different operating conditions, in an industrially acceptable time, various dedicated parametric modeling software [15-17], with a high level of flexibility and adaptability, are used [18-20].
From an industrial standpoint, the feature-based parametric CAD is currently the industry standard technology to create geometric models and assemblies and is used in the manufacturing of LPG storage tanks from the automotive industry [21-23].
Problems related to modeling strategies of LPG storage tanks, identifying the most appropriate modeling practice for a particular design situation and understanding how the design tree can be structured are major factors to guarantee success and to ensure an efficient functional model and to minimize the time and effort in the design process [24-26].
Various variants of LPG storage tanks with good technical-functional characteristics can be designed using virtual prototypes with specific modeling procedures, based on descriptive geometry concepts [27-29], and formal CAD strategies for creating robust and reusable parametric CAD models with a lower cost of production [30, 31].
Finite element analysis (FEA) is a computer-based process used for modeling complex products [32-34] and failure analysis which provides various advantages to complement laboratory experiments finding a series of solutions to engineering complex problems [35-37].
In the scientific literature, there are proposed for the design and improvement of these storage tanks different CFD (Computational Fluid Dynamics) models that could be used as a flexible modelling tool in CFD simulations. The life of LPG storage tank is determined by a number of variables such as the load efforts, position, mass, the tank material, the corrosion process etc.

This paper studies the influence of uniaxial traction loads applied normally on the parallel sides of the 3-D hexagonal toroid with regular hexagonal cross-section used in the manufacturing of LPG storage tanks using the finite element analysis.

## 2. Design methodology

### 2.1. Basic geometry of the parametric 3-D model

Let's consider the parametric 3-D model generated by revolving of a closed generating curve $C_G$ (a hexagon with rounded corners) along a closed guiding curve $C_D$ (a hexagon with rounded corners) as shown in figs. 1 and 2 [14].
The following parameters were applied as input parameters to the 3-D parametric model (figs. 1 and 2): a) a closed generating curve CG (a hexagon with a side value L = 175 mm, with rounded corners, radius R = 50 mm), and b), the guiding curve CD (a hexagon with a side value L = 430 mm, with rounded corners, radius R = 180 mm), and the thickness = 10 mm.

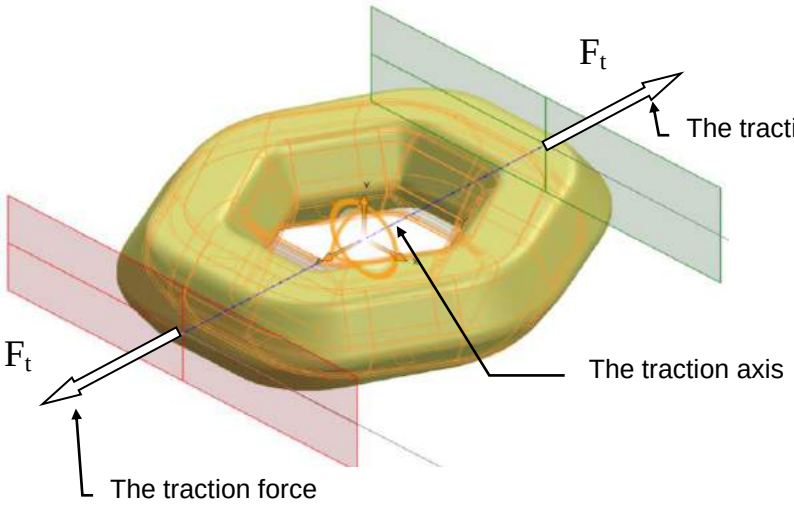


**Fig. 1.** The isometric representation of 3-D model, not deformed, before the uniaxial traction

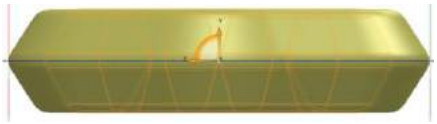

**Fig. 2.** The lateral representation of 3-D model not deformed, before the uniaxial traction

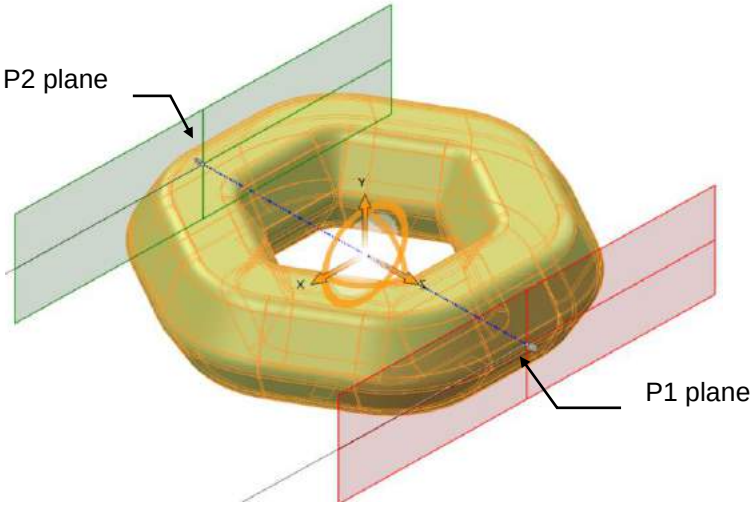


**Fig. 3.** The isometric representation of 3-D model, deformed, after the uniaxial traction

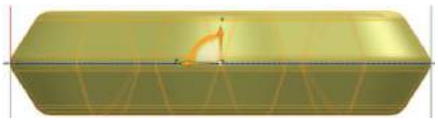

**Fig. 4.** The lateral representation of 3-D model deformed, after the uniaxial traction

The deformation of the shape of the 3-D model is made as a result of the displacement of the point of application of force over a distance $\Delta L_t$ = 1.33% from the value of the median diameter of the model measured in the direction of the traction axis.

As a result of the applied forces, a decrease of the cross-sectional area appears, simultaneously with the elongation of the shape of the model in the forces direction.
The uniaxial displacement under traction loads is noted with $L_c$.

### 2.2. Numerical analysis of the parametric 3-D model

Based on the physical model, the modeling was done in the AutoCAD Autodesk 2020 software and the numerical analysis was performed with SolidWorks 2020 software with the Static, Thermal and Design Study modules. The design data used were:

- the tank material is AISI 4340 steel;
- the maximum hydraulic test pressure: $p_{max}$ = 30 bar;
- the working temperature between the limits: T = -30 $^0$C up to T = 60 $^0$C;
- supporting surfaces located on the inferior side;
- the duration of the tank exploitation: $n_a$ = 15 years;
- the corrosion rate of the material: $v_c$ = 0.07 mm/year.

Numerical calculations were performed for: mesh standard type, solid mesh, curvature-based mesh with quality high, Jacobian in 16 points, element size 11 mm, number of nodes 30628, number of elements 15368.
The parameterized 3-D model used in calculus is a section of ½ (fig. 5) from the initial physical model and the corresponding surfaces to which the constraints and restrictions are applied are shown in fig. 5. The finite element discretization for the 3-D parametric model is shown in fig. 6.

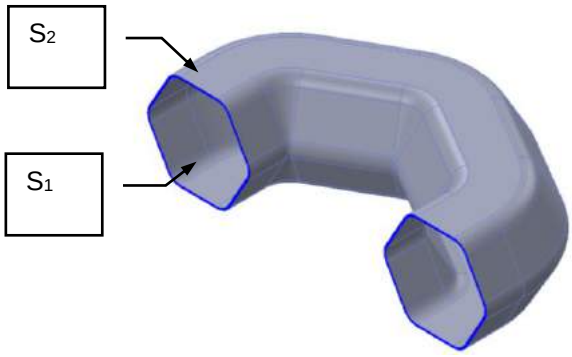


**Fig. 5.** The surfaces to which the constraints were applied.

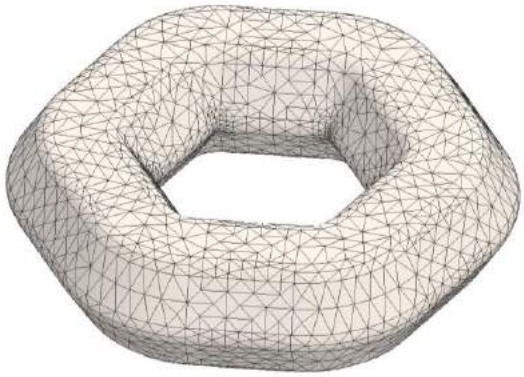

**Fig. 6.** The discretization of the model

The design data used in this analysis for the tank lateral cover are:
- the maximum pressure $p_{max}$ = 3 N/mm$^2$ on the inner surface $S_1$;
- the working temperature between the limits: T = -30 $^0$C to T = 60 $^0$C on the exterior surface $S_2$;
- the fixation of the tank on the six tank supports located at the inferior part of the tank.

The values of the state of stress Von Mises determined by the finite element method for $n_a$ = 0, 5, 10 and 15 years are shown in table 1.

**Table 1:** The Von Misess resultant effort for $n_a$= 0, 5, 10 and 15 years

| Lc [mm] | T [$^0$C] | | | | T [$^0$C] | | | |
|---|---|---|---|---|---|---|---|---|
| | -30$^0$ | 0$^0$ | 30$^0$ | 60$^0$ | -30$^0$ | 0$^0$ | 30$^0$ | 60$^0$ |
| | $n_a$ = 0 [years] | | | | $n_a$ = 5 [years] | | | |
| | $\sigma_t$ [MPa] | | | | $\sigma_t$ [MPa] | | | |
| 0 | 665.40 | 565.66 | 479.29 | 527.43 | 610.22 | 514.24 | 511.09 | 560.58 |
| 1 | 545.22 | 470.35 | 485.68 | 541.97 | 593.51 | 502.09 | 506.01 | 563.14 |
| 2 | 505.58 | 443.67 | 466.81 | 527.46 | 534.81 | 472.72 | 510.20 | 556.49 |
| 3 | 521.01 | 448.29 | 487.10 | 540.16 | 584.30 | 502.98 | 514.43 | 571.78 |
| 4 | 531.82 | 457.71 | 473.33 | 527.49 | 546.24 | 474.59 | 525.31 | 588.70 |
| 5 | 529.59 | 455.52 | 488.13 | 546.48 | 565.15 | 486.81 | 500.36 | 558.24 |
| 6 | 524.46 | 492.94 | 474.49 | 531.09 | 602.07 | 524.28 | 521.33 | 578.30 |

| | | | | | | | | |
|---|---|---|---|---|---|---|---|---|
| 7 | 657.82 | 559.64 | 485.78 | 538.97 | 576.45 | 494.93 | 478.15 | 522.33 |
| 8 | 619.07 | 524.38 | 468.05 | 468.05 | 704.33 | 604.23 | 505.07 | 559.88 |
| 9 | 523.90 | 446.61 | 466.19 | 521.03 | 691.79 | 591.13 | 502.17 | 556.59 |
| 10 | 522.72 | 444.74 | 470.08 | 527.07 | 589.18 | 514.04 | 507.66 | 568.22 |
| | $n_a$ = 10 [years] | | | | $n_a$ = 15 [years] | | | |
| 0 | 716.26 | 615.97 | 591.97 | 641.72 | 754.50 | 655.70 | 636.94 | 688.12 |
| 1 | 718.61 | 623.72 | 586.50 | 632.99 | 680.88 | 589.79 | 591.14 | 638.86 |
| 2 | 585.76 | 509.56 | 535.62 | 587.22 | 760.61 | 669.24 | 628.56 | 679.21 |
| 3 | 591.81 | 516.25 | 567.98 | 623.54 | 657.33 | 583.00 | 643.56 | 708.33 |
| 4 | 722.39 | 623.49 | 525.83 | 545.65 | 640.55 | 566.19 | 600.51 | 644.61 |
| 5 | 602.64 | 531.32 | 576.29 | 642.99 | 660.04 | 586.78 | 622.83 | 658.88 |
| 6 | 737.04 | 738.28 | 740.10 | 742.49 | 602.60 | 572.32 | 634.55 | 700.08 |
| 7 | 587.54 | 510.56 | 528.33 | 559.51 | 636.33 | 567.02 | 565.91 | 573.71 |
| 8 | 683.04 | 585.06 | 555.56 | 609.76 | 695.16 | 592.73 | 556.54 | 591.79 |
| 9 | 584.59 | 509.34 | 584.59 | 585.40 | 789.42 | 683.81 | 579.95 | 597.50 |
| 10 | 581.63 | 505.67 | 511.08 | 561.02 | 735.27 | 637.78 | 542.83 | 590.54 |

The graphs corresponding to the Von Mises resultant efforts $\sigma_t$ ($L_c$, T) taking into account the results from table 1 are graphically shown in figs. 7-10, respectively.

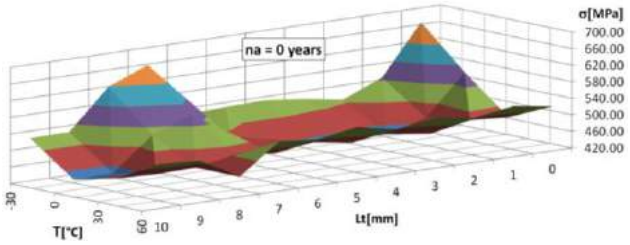


**Fig. 7.** The graphs of $\sigma = f(L_c, T)$ for $n_a$ = 0 years

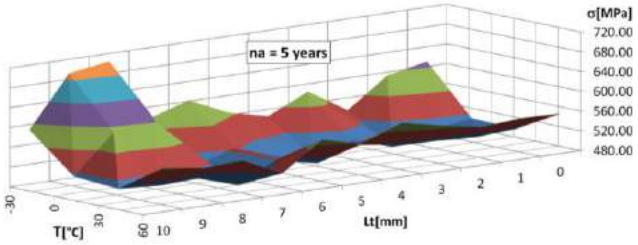


**Fig. 8.** The graphs of $\sigma = f(L_c, T)$ for $n_a$ = 5 years

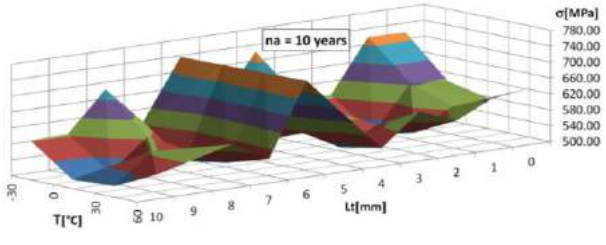


**Fig. 9.** The graphs of $\sigma = f(L_c, T)$ for $n_a$ = 10 years

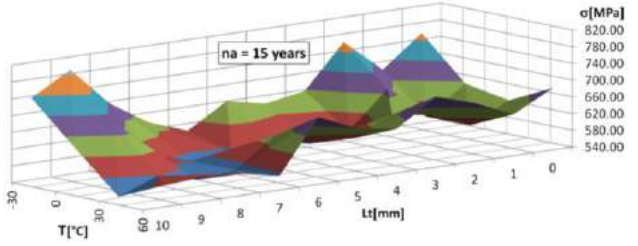


**Fig. 10.** The graphs of $\sigma = f(L_c, T)$ for $n_a$ = 15 years

The graphs of curves corresponding to the Von Mises resultant efforts $\sigma_t$ ($L_c$, T) for $n_a$ = {0, 5, 10, and 15 years}, are graphically shown in fig. 11.

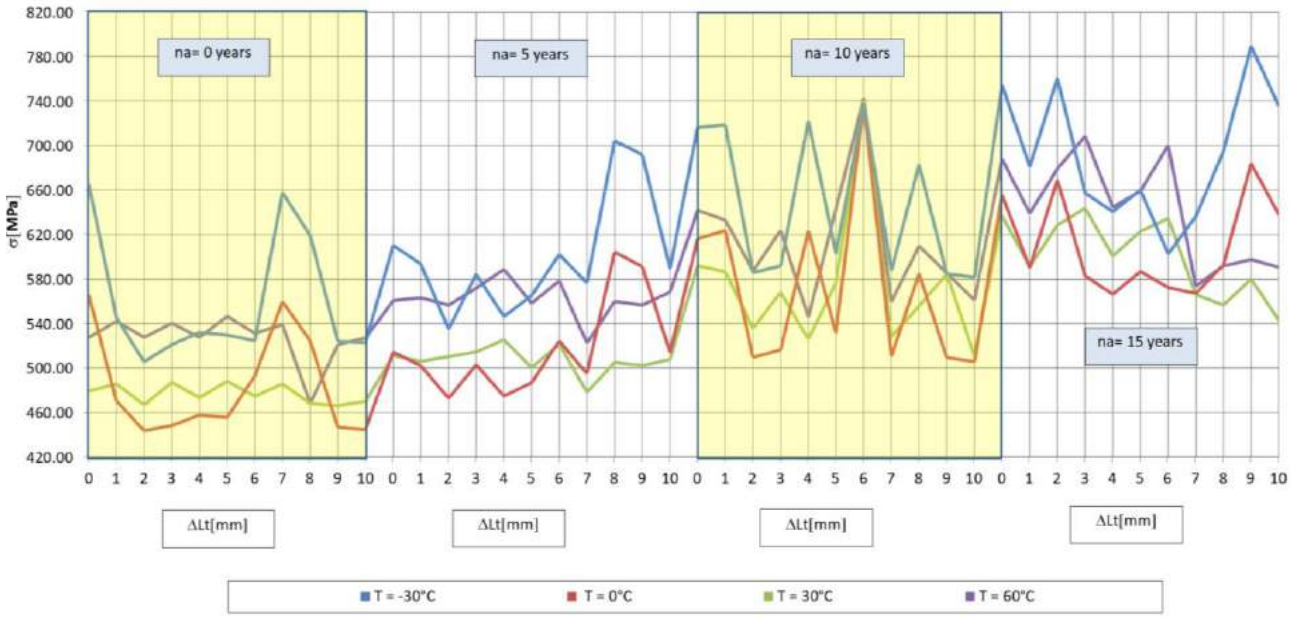


**Fig. 11.** The graphs of $\sigma_t$ ($L_c$, T) for: T = {-30 $^0$C, 0 $^0$C, 30 $^0$C, 60 $^0$C} and $n_a$= {0, 5, 10 and 15 years}

The results show the Von Mises resultant efforts has a maximum value corresponding for T = -30 $^0$C. It was calculated the percentage variation of the Von Mises effort $\Delta\sigma_t$ ($L_c$, T) versus the resulting stress state of the non-deformed tank (for $L_c$ = 0), using the following formula:

$$\Delta\sigma_t = \frac{(\sigma_{Lc=0} - \sigma)}{\sigma_{Lc=0}} \cdot 100\ [\%] \quad (1)$$

The percentage variation of Von Mises resultant effort $\Delta\sigma_t$ in relation to the initial effort status (computed in table 2) and the corresponding graphs (in 2-D) are shown in fig. 12, while the corresponding graphs (in 3-D) are shown in figs. 13-16.

**Table 2:** The percentage variation of Von Mises resultant effort for $n_a$= 0, 5, 10 and 15 years

| Lc [mm] | T [$^0$C] | | | | T [$^0$C] | | | |
|---|---|---|---|---|---|---|---|---|
| | -30$^0$ | 0$^0$ | 30$^0$ | 60$^0$ | -30$^0$ | 0$^0$ | 30$^0$ | 60$^0$ |
| | $n_a$ = 0 [years] | | | | $n_a$ = 5 [years] | | | |
| | $\Delta\sigma_t$ [%] | | | | $\Delta\sigma_t$ [%] | | | |
| 1 | -18.06 | -16.85 | 1.33 | 2.76 | -2.74 | -2.36 | -0.99 | 0.46 |
| 2 | -24.02 | -21.57 | -2.60 | 0.01 | -12.36 | -8.07 | -0.18 | -0.73 |
| 3 | -21.70 | -20.75 | 1.63 | 2.41 | -4.25 | -2.19 | 0.65 | 2.00 |
| 4 | -20.08 | -19.08 | -1.24 | 0.01 | -10.49 | -7.71 | 2.78 | 5.02 |
| 5 | -20.41 | -19.47 | 1.84 | 3.61 | -7.39 | -5.33 | -2.10 | -0.42 |
| 6 | -21.18 | -12.86 | -1.00 | 0.69 | -1.34 | 1.95 | 2.00 | 3.16 |
| 7 | -1.14 | -1.06 | 1.35 | 2.19 | -5.54 | -3.76 | -6.44 | -6.82 |
| 8 | -6.96 | -7.30 | -2.34 | -11.26 | 15.42 | 17.50 | -1.18 | -0.12 |
| 9 | -21.27 | -21.05 | -2.73 | -1.21 | 13.37 | 14.95 | -1.75 | -0.71 |
| 10 | -21.44 | -21.38 | -1.92 | -0.07 | -3.45 | -0.04 | -0.67 | 1.36 |
| | $n_a$ = 10 [years] | | | | $n_a$ = 15 [years] | | | |
| | $\Delta\sigma_t$ [%] | | | | $\Delta\sigma_t$ [%] | | | |
| 1 | 0.33 | 1.26 | -0.92 | -1.36 | -9.76 | -10.05 | -7.19 | -7.16 |
| 2 | -18.22 | -17.27 | -9.52 | -8.49 | 0.81 | 2.06 | -1.32 | -1.30 |
| 3 | -17.38 | -16.19 | -4.05 | -2.83 | -12.88 | -11.09 | 1.04 | 2.94 |
| 4 | 0.85 | 1.22 | -11.17 | -14.97 | -15.10 | -13.65 | -5.72 | -6.32 |

| | | | | | | | | |
|---|---|---|---|---|---|---|---|---|
| 5 | -15.86 | -13.74 | -2.65 | 0.20 | -12.52 | -10.51 | -2.21 | -4.25 |
| 6 | 2.90 | 19.86 | 25.02 | 15.70 | -20.13 | -12.72 | -0.37 | 1.74 |
| 7 | -17.97 | -17.11 | -10.75 | -12.81 | -15.66 | -13.52 | -11.15 | -16.63 |
| 8 | -4.64 | -5.02 | -6.15 | -4.98 | -7.87 | -9.60 | -12.62 | -14.00 |
| 9 | -18.38 | -17.31 | -1.25 | -8.78 | 4.63 | 4.29 | -8.95 | -13.17 |
| 10 | -18.80 | -17.91 | -13.66 | -12.58 | -2.55 | -2.73 | -14.78 | -14.18 |

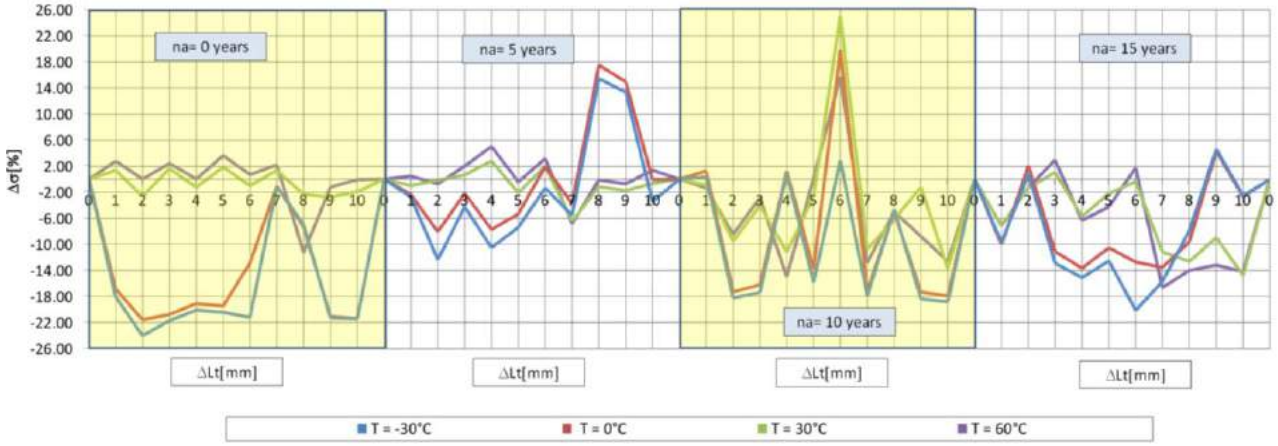


**Fig. 12.** The graphs of $\Delta\sigma$ ($L_c$, T) for: T = {-30 $^0$C, 0 $^0$C, 30 $^0$C, 60 $^0$C } and $n_a$= {0, 5, 10 and 15 years}

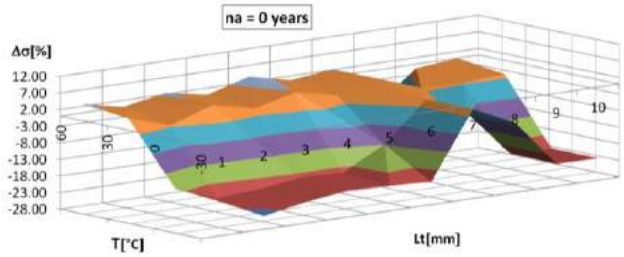


**Fig. 13.** The graphs of $\Delta\sigma$ ($L_c$, T) for $n_a$ = 0 years

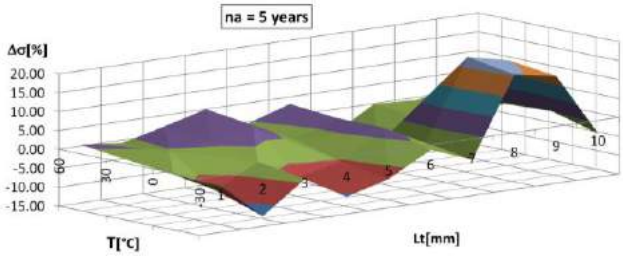


**Fig. 14.** The graphs of $\Delta\sigma$ ($L_c$, T) for $n_a$ = 5 years

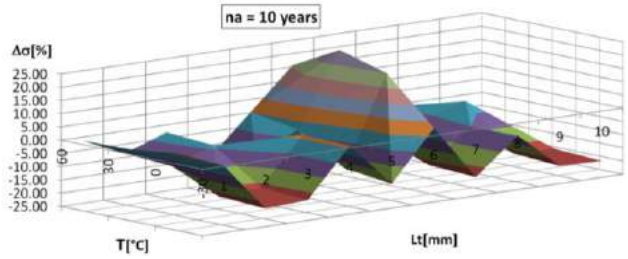


**Fig. 15.** The graphs of $\Delta\sigma$ ($L_c$, T) for $n_a$ = 10 years

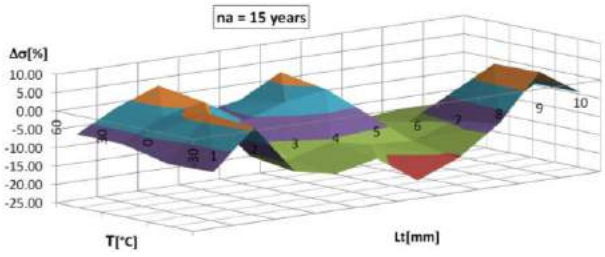


**Fig. 16.** The graphs of $\Delta\sigma$ ($L_c$, T) for $n_a$ = 15 years

For the most important cases of the uniaxial traction loads, the Von Mises resultant efforts $\sigma_t$ ($L_c$, T) was calculated taking into account the results from table 3, while the corresponding graphs are shown in figs. 17-20.

**Table 3:** The particular cases for graphical representation of the Von Mises resultant effort

| No. case | $n_a$ [years] | Lc [mm] | T [°C] | $\sigma_t$ [MPa] | u [mm] |
|---|---|---|---|---|---|
| 1 | 0 | 8 | -30 | 468.05 | 0.598 |
| 2 | 5 | 6 | 0 | 524.28 | 0.682 |
| 3 | 10 | 6 | 30 | 740.10 | 0.741 |
| 4 | 15 | 4 | 60 | 644.61 | 0.849 |

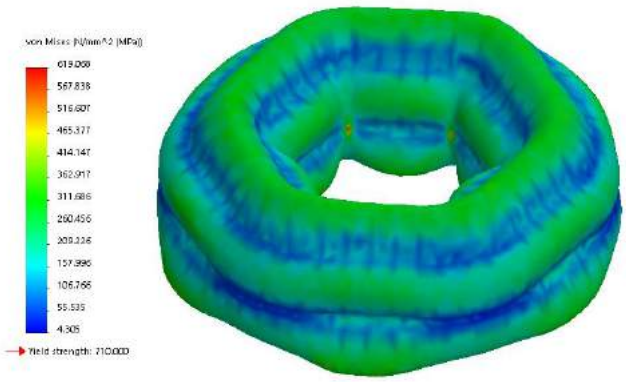

**Fig. 17.** The graphs of $\sigma = f(L_c, T)$ for case 1

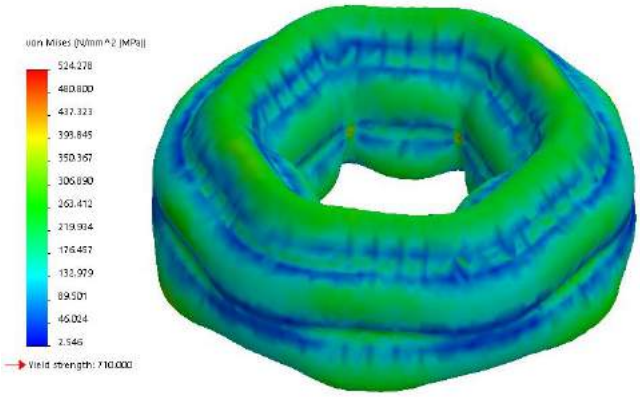

**Fig. 18.** The graphs of $\sigma = f(L_c, T)$ for case 2

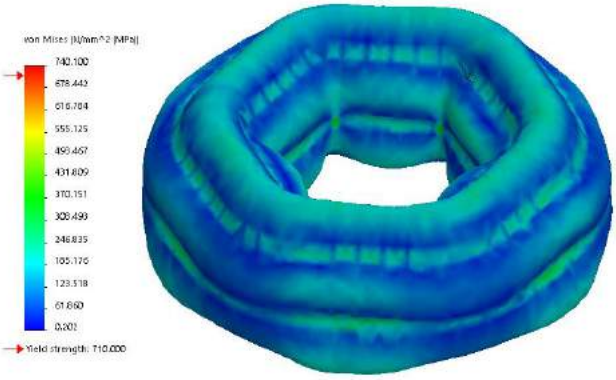

**Fig. 19.** The graphs of $\sigma = f(L_c, T)$ for case 3

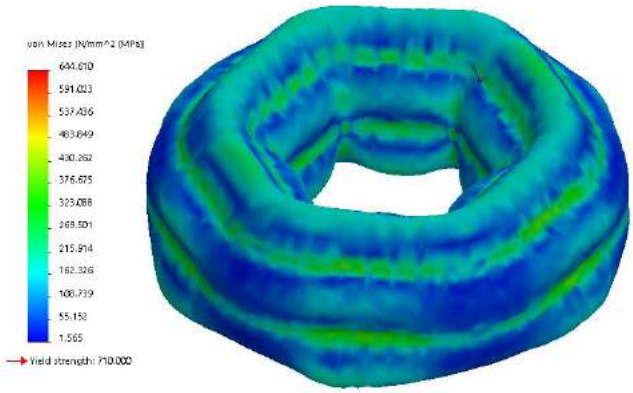

**Fig. 20.** The graphs of $\sigma = f(L_c, T)$ for case 4

The values of the resultant linear deformation *u* determined by the finite element method for $n_a$= {0, 5, 10 and 15 years} are shown in table 4.

**Table 4:** The resultant linear deformation for $n_a$= {0, 5, 10 and 15 years}

| Lc [mm] | T [$^0$C] | | | | T [$^0$C] | | | |
|---|---|---|---|---|---|---|---|---|
| | -30$^0$ | 0$^0$ | 30$^0$ | 60$^0$ | -30$^0$ | 0$^0$ | 30$^0$ | 60$^0$ |
| | $n_a$ = 0 [years] | | | | $n_a$ = 5 [years] | | | |
| | $u_c$ [mm] | | | | $u_c$ [mm] | | | |
| 0 | 0.869 | 0.837 | 0.805 | 0.777 | 0.938 | 0.904 | 0.871 | 0.841 |
| 1 | 0.652 | 0.660 | 0.671 | 0.685 | 0.709 | 0.715 | 0.724 | 0.733 |
| 2 | 0.596 | 0.603 | 0.612 | 0.622 | 0.675 | 0.683 | 0.693 | 0.705 |
| 3 | 0.619 | 0.628 | 0.638 | 0.651 | 0.672 | 0.678 | 0.686 | 0.695 |
| 4 | 0.622 | 0.631 | 0.642 | 0.656 | 0.700 | 0.711 | 0.723 | 0.736 |
| 5 | 0.624 | 0.628 | 0.634 | 0.641 | 0.685 | 0.692 | 0.700 | 0.711 |
| 6 | 0.618 | 0.626 | 0.637 | 0.650 | 0.675 | 0.682 | 0.691 | 0.703 |
| 7 | 0.618 | 0.624 | 0.634 | 0.646 | 0.644 | 0.636 | 0.632 | 0.639 |

| | | | | | | | | |
|---|---|---|---|---|---|---|---|---|
| 8 | 0.598 | 0.604 | 0.611 | 0.611 | 0.671 | 0.679 | 0.689 | 0.700 |
| 9 | 0.602 | 0.609 | 0.617 | 0.629 | 0.698 | 0.701 | 0.707 | 0.713 |
| 10 | 0.614 | 0.621 | 0.631 | 0.642 | 0.699 | 0.703 | 0.710 | 0.717 |
| | $n_a$ = 10 [years] | | | | $n_a$ = 15 [years] | | | |
| 0 | 1.011 | 0.974 | 0.944 | 0.916 | 1.106 | 1.076 | 1.047 | 1.020 |
| 1 | 0.840 | 0.842 | 0.845 | 0.851 | 0.872 | 0.869 | 0.867 | 0.794 |
| 2 | 0.711 | 0.715 | 0.721 | 0.729 | 0.788 | 0.791 | 0.797 | 0.805 |
| 3 | 0.737 | 0.748 | 0.761 | 0.776 | 0.777 | 0.787 | 0.799 | 0.812 |
| 4 | 0.731 | 0.729 | 0.735 | 0.743 | 0.834 | 0.837 | 0.842 | 0.849 |
| 5 | 0.754 | 0.761 | 0.770 | 0.780 | 0.829 | 0.835 | 0.843 | 0.851 |
| 6 | 0.748 | 0.744 | 0.741 | 0.739 | 0.808 | 0.813 | 0.820 | 0.830 |
| 7 | 0.708 | 0.710 | 0.714 | 0.722 | 0.792 | 0.783 | 0.774 | 0.768 |
| 8 | 0.755 | 0.752 | 0.759 | 0.769 | 0.805 | 0.804 | 0.806 | 0.812 |
| 9 | 0.799 | 0.788 | 0.799 | 0.769 | 0.812 | 0.805 | 0.802 | 0.800 |
| 10 | 0.761 | 0.763 | 0.766 | 0.771 | 0.842 | 0.836 | 0.830 | 0.824 |

The graphs of curves (in 2-D) corresponding to the resultant linear deformation $u$ = ($L_c$, T) for $n_a$ = {0, 5, 10 and 15 years}; are graphically shown in fig. 21, while the corresponding graphs (in 3-D) are shown figs. 22-25.

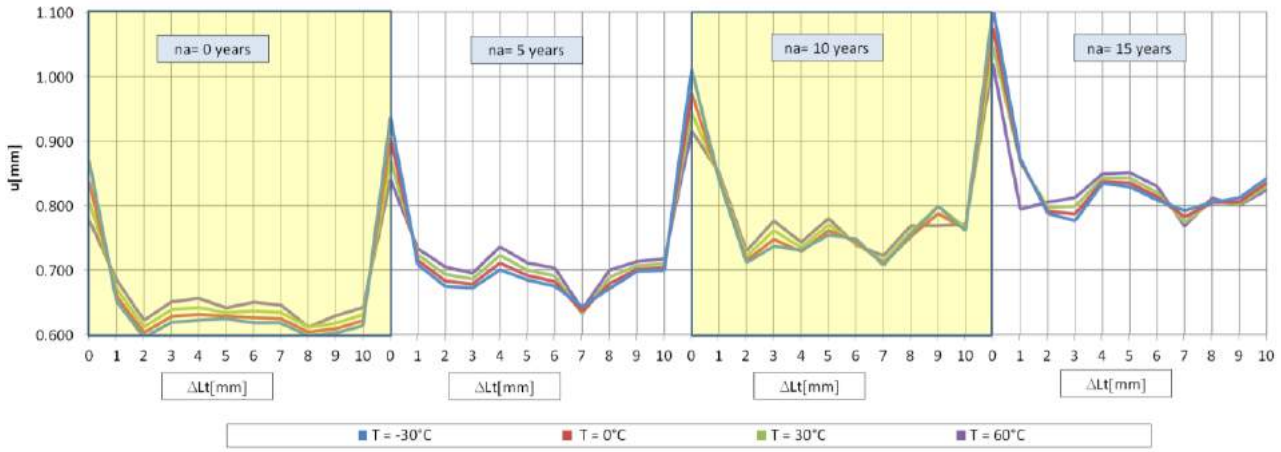


**Fig. 21.** The graphs of $u$ = ($L_c$, T) for: T = {-30 $^0$C, 0 $^0$C, 30 $^0$C, 60 $^0$C} and $n_a$= {0, 5, 10 and 15 years}

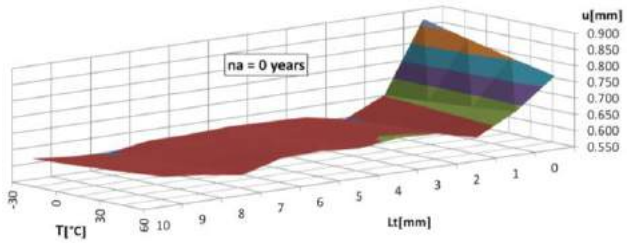


**Fig. 22.** The graphs of u ($L_c$, T) for $n_a$ = 0 years

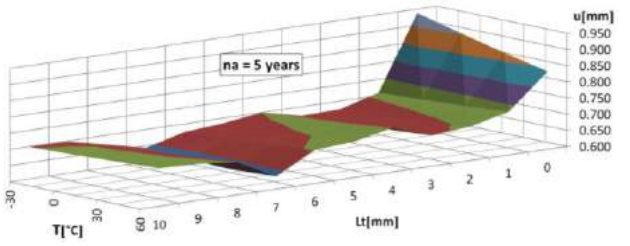


**Fig. 23.** The graphs of u ($L_c$, T) for $n_a$ = 5 years

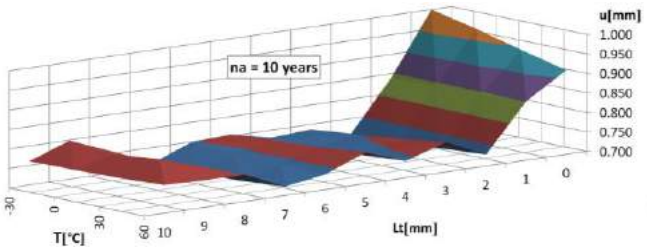


**Fig. 24.** The graphs of u = f($L_c$, T) for $n_a$ = 10 years

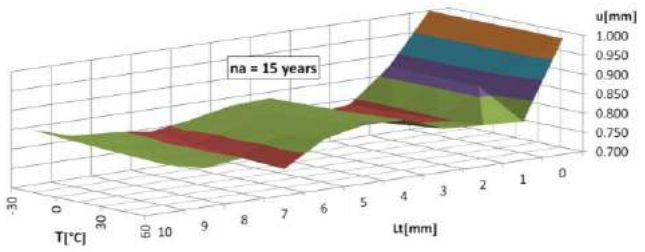


**Fig. 25.** The graphs of u = f($L_c$, T) for $n_a$ = 15 years

For the most important cases of the uniaxial traction loads, the resultant linear deformation *u* = ($L_c$, T) was calculated taking into account the results from table 3, while the corresponding graphs are shown in figs. 26-29.

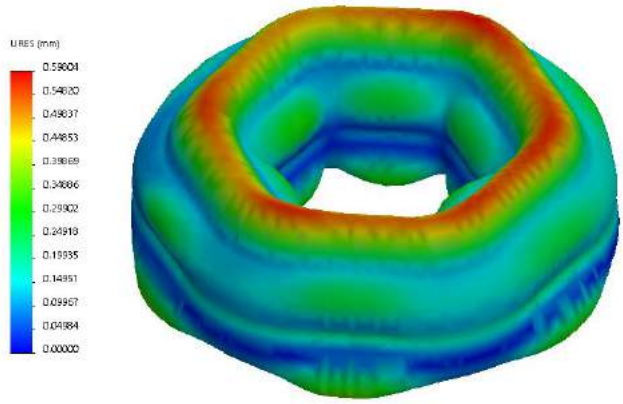


**Fig. 26.** The graphs of u = f($L_c$, T) for case 1

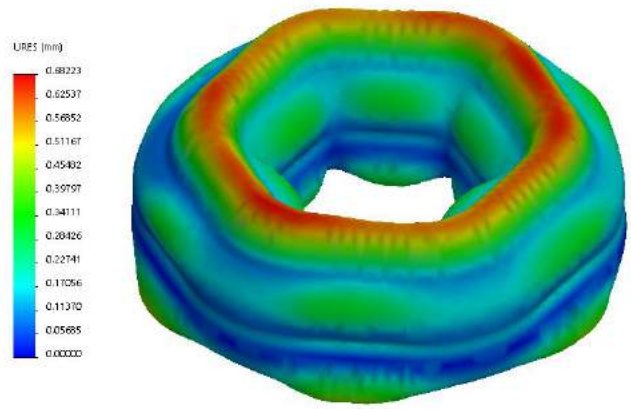


**Fig. 27.** The graphs of u = f($L_c$, T) for case 2

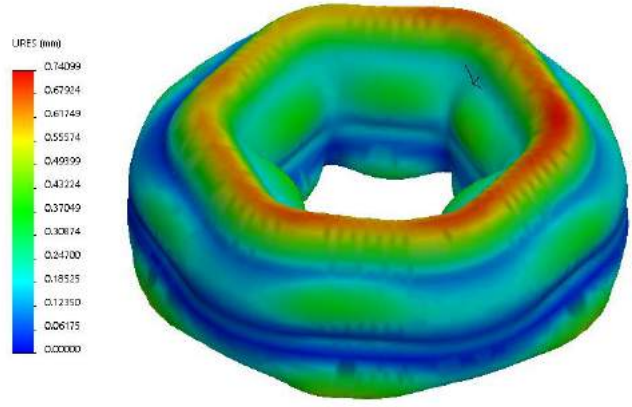


**Fig. 28.** The graphs of u = f($L_c$, T) for case 3

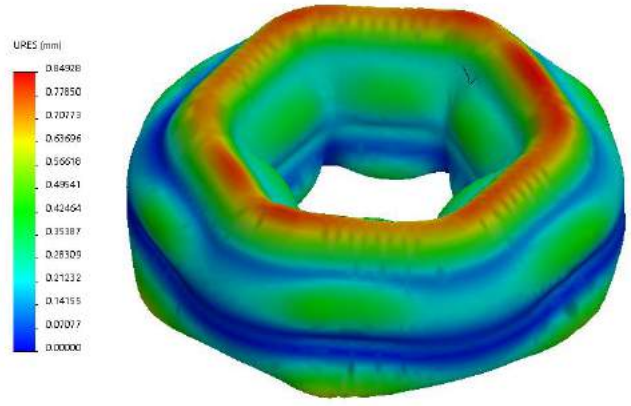


**Fig. 29.** The graphs of u = f($L_c$, T) for case 4

It was calculated the percentage variation of the resultant linear deformation $\Delta u$ ($L_c$, T) versus the resulting state of the non-deformed tank (for $u_{Lc}$= 0), using the following formula:

$$\Delta u = \frac{(u_{Lc=0} - u)}{u_{Lc=0}} \cdot 100 \ [\%] \tag{2}$$

The percentage variation of resultant linear deformation $\Delta u$ in relation to the initial value was calculated in table 5 and the corresponding graphs are given in fig. 30.

**Table 5:** The percentage variation of resultant liniar deformation Δu for $n_a$= 0, 5, 10 and 15 years

| Lc [mm] | T [$^0$C] | | | | T [$^0$C] | | | |
|---|---|---|---|---|---|---|---|---|
| | -30$^0$ | 0$^0$ | 30$^0$ | 60$^0$ | -30$^0$ | 0$^0$ | 30$^0$ | 60$^0$ |
| | $n_a$ = 0 [years] | | | | $n_a$ = 5 [years] | | | |
| | Δu [%] | | | | Δu [%] | | | |
| 1 | -25.02 | -21.16 | -16.65 | -11.88 | -24.42 | -20.84 | -16.90 | -12.79 |
| 2 | -31.45 | -27.95 | -24.06 | -19.95 | -28.01 | -24.42 | -20.39 | -16.13 |
| 3 | -28.82 | -24.98 | -20.73 | -16.26 | -28.30 | -24.93 | -21.21 | -17.30 |
| 4 | -28.41 | -24.55 | -20.29 | -15.56 | -25.30 | -21.33 | -17.00 | -12.45 |
| 5 | -28.17 | -24.93 | -21.32 | -17.45 | -26.97 | -23.48 | -19.65 | -15.42 |
| 6 | -28.90 | -25.15 | -20.94 | -16.35 | -27.99 | -24.50 | -20.65 | -16.32 |
| 7 | -28.92 | -25.37 | -21.27 | -16.87 | -31.35 | -29.66 | -27.43 | -23.98 |
| 8 | -31.19 | -27.82 | -24.12 | -21.33 | -28.39 | -24.88 | -20.90 | -16.73 |
| 9 | -30.69 | -27.21 | -23.35 | -19.03 | -25.55 | -22.40 | -18.85 | -15.17 |
| 10 | -29.40 | -25.77 | -21.71 | -17.38 | -25.40 | -22.15 | -18.51 | -14.67 |
| | $n_a$ = 10 [years] | | | | $n_a$ = 15 [years] | | | |
| | Δu [%] | | | | Δu [%] | | | |
| 1 | -16.92 | -13.58 | -10.45 | -7.07 | -21.14 | -19.16 | -17.17 | -22.15 |
| 2 | -29.64 | -26.65 | -23.59 | -20.35 | -28.78 | -26.46 | -23.88 | -21.06 |
| 3 | -27.11 | -23.28 | -19.36 | -15.25 | -29.80 | -26.83 | -23.73 | -20.39 |
| 4 | -27.70 | -25.23 | -22.13 | -18.88 | -24.57 | -22.17 | -19.57 | -16.75 |
| 5 | -25.38 | -21.86 | -18.41 | -14.82 | -25.06 | -22.35 | -19.54 | -16.56 |
| 6 | -25.99 | -23.63 | -21.49 | -19.34 | -26.92 | -24.37 | -21.71 | -18.68 |
| 7 | -30.01 | -27.16 | -24.37 | -21.14 | -28.39 | -27.24 | -26.13 | -24.72 |
| 8 | -25.28 | -22.84 | -19.54 | -16.09 | -27.22 | -25.22 | -23.01 | -20.44 |
| 9 | -20.99 | -19.15 | -15.36 | -16.04 | -26.60 | -25.12 | -23.43 | -21.55 |
| 10 | -24.74 | -21.73 | -18.85 | -15.76 | -23.84 | -22.32 | -20.79 | -19.19 |

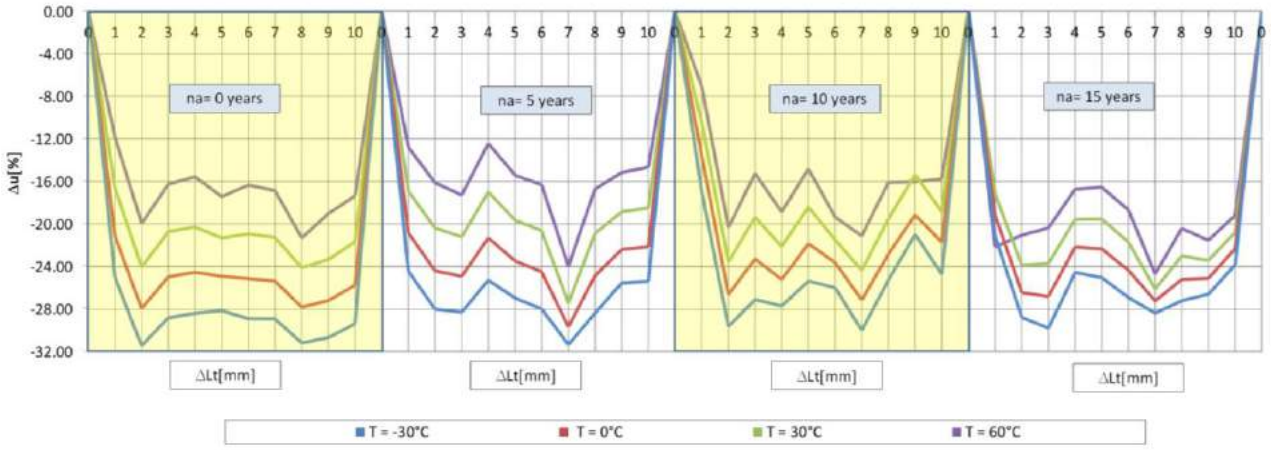


**Fig. 30.** The graphs of Δ*u* = ($L_c$, T) for: T = {-30 $^0$C, 0 $^0$C, 30 $^0$C, 60 $^0$C} and $n_a$= {0, 5, 10 and 15 years}

## 3. Conclusions

Following the numerical analyses and the resulting graphs it has been found that:
- for $n_a$= 15 years, $\sigma_{max}$ = 789.42 MPa > $\sigma_a$ = 710 MPa. Also, the state of efforts are amplified with the increase of corrosion and traction loads, and by the decreasing of the working temperature;
- the increase of the working temperature determines the decrease of the stress state, while the traction and corrosion process increase the stress state;

- $\Delta\sigma$ [%] $\cong$ 25.02% for T = 30 $^0$C and $n_a$= 10 years, while $\Delta\sigma$ [%] $\cong$ -24.02% for T = -30 $^0$C and $n_a$= 0 years;
- the highest values of resulting linear deformations and the Von Mises stress occur in the middle area of the torus sides. Also, the resultant linear deformation *u* is amplified with the increase of corrosion, traction loads, and the working temperature;
- $u_{max} \cong$ 1.1 mm for T = -30 $^0$C and $n_a$= 10 years. $\Delta u_{max}$ [%] $\cong$ 31.45% for T = -30 $^0$C and $n_a$= 0 years;
- for $\Delta$L < 1.33% of the diameter of the torus, the stress state increases by $\Delta\sigma \cong$ 25.02% and the percentage variation of resultant linear deformation $\Delta$u = 31.5%.

**References**

[1] Ghiţă, C. Mirela, Anton C. Micu, Mihai Ţălu, and Ştefan Ţălu. "Shape optimization of a thoroidal methane gas tank for automotive industry." *Annals of Faculty of Engineering Hunedoara - International Journal of Engineering,* Tome X, Fascicule 3 (2012): 295-297.
[2] Ghiţă, C. Mirela, Anton C. Micu, Mihai Ţălu, and Ştefan Ţălu. "Shape optimization of vehicle's methane gas tank." *Annals of Faculty of Engineering Hunedoara - International Journal of Engineering,* Tome X, Fascicule 3 (2012): 259-266.
[3] Ghiţă, C. Mirela, Anton C. Micu, Mihai Ţălu, Ştefan Ţălu, and Ema I. Adam. "Computer-Aided Design of a classical cylinder gas tank for the automotive industry." *Annals of Faculty of Engineering Hunedoara - International Journal of Engineering,* Tome XI, Fascicule 4 (2013): 59-64.
[4] Ghiţă, C. Mirela, Anton C. Micu, Mihai Ţălu, and Ştefan Ţălu. "3D modelling of a shrink fitted concave ended cylindrical tank for automotive industry." *Acta Technica Corviniensis – Bulletin of Engineering,* Tome VI, Fascicule 4 (2013): 87-92.
[5] Ghiţă, C. Mirela, Anton C. Micu, Mihai Ţălu, and Ştefan Ţălu. "3D modelling of a gas tank with reversed end up covers for automotive industry." *Annals of Faculty of Engineering Hunedoara - International Journal of Engineering,* Tome XI, Fascicule 3 (2013): 195-200.
[6] Ghiţă, C. Mirela, Ştefan C. Ghiță, Ştefan Ţălu, and Simona Rotaru. "Optimal design of cylindrical rings used for the shrinkage of vehicle tanks for compressed natural gas." *Annals of Faculty of Engineering Hunedoara - International Journal of Engineering,* Tome XII, Fascicule 3 (2014): 243-250.
[7] Bică, Marin, Mihai Ţălu, and Ştefan Ţălu. "Optimal shapes of the cylindrical pressurized fuel tanks." *Hidraulica Magazine*, no. 4 (December 2017): 6-17.
[8] Vintilă, Daniela, Mihai Ţălu, and Ştefan Ţălu. "The CAD analyses of a torospheric head cover of a pressurized cylindrical fuel tank after the crash test." *Hidraulica Magazine*, no. 4 (December 2017): 57-66.
[9] Ţălu, Ştefan, and Mihai Ţălu. "The influence of deviation from circularity on the stress of a pressurized fuel cylindrical tank." *Hidraulica Magazine*, no. 4 (December 2017): 34-45.
[10] Ţălu, Mihai. "The influence of the corrosion and temperature on the Von Mises stress in the lateral cover of a pressurized fuel tank." *Hidraulica Magazine*, no. 4 (December 2017): 89-97.
[11] Ţălu, Mihai, and Ştefan Ţălu. "Analysis of temperature resistance of pressurized cylindrical fuel tanks." *Hidraulica Magazine*, no. 1 (March 2018): 6-15.
[12] Ţălu, Mihai, and Ştefan Ţălu. "Design and optimization of pressurized toroidal LPG fuel tanks with variable section." *Hidraulica Magazine*, no. 1 (March 2018): 32-41.
[13] Ţălu, Ştefan, and Mihai Ţălu. "Algorithm for optimal design of pressurized toroidal LPG fuel tanks with constant section described by imposed algebraic plane curves." *Hidraulica Magazine*, no. 2 (June 2018): 14-21.
[14] Ţălu, Mihai, and Ştefan Ţălu. "The optimal CAD design of a 3D hexagonal toroid with regular hexagonal cross-section used in manufacturing of LPG storage tanks." *Hidraulica Magazine*, no. 2 (June 2018): 49-56.
[15] Ţălu, Mihai, and Ştefan Ţălu. "The influence of corrosion and temperature variation on the minimum safety factor of a 3D hexagonal toroid with regular hexagonal cross-section used in manufacturing of LPG storage tanks." *Hidraulica Magazine*, no. 3 (September 2018): 16-25.
[16] Ţălu, Ştefan, and Mihai Ţălu. "The influence of corrosion and pressure variation on the minimum safety factor of a 3D hexagonal toroid with regular hexagonal cross-section used in manufacturing of LPG storage tanks." *Hidraulica Magazine*, no. 3 (September 2018): 39-45.
[17] Ţălu, Mihai, and Ştefan Ţălu. "The influence of corrosion and temperature variation on a CNG storage tank with a combined form consisting of a torus and a sphere." *Hidraulica Magazine*, no. 4 (December 2019): 93-104.
[18] Ţălu, Mihai, and Ştefan Ţălu. "Optimal design of a CNG storage tank with a combined form consisting of a torus and a sphere." *Hidraulica Magazine*, no. 4 (December 2019): 73-82.
[19] Ţălu, Mihai, and Ştefan Ţălu. "Study of temperature–corrosion–torsion affecting factors on the shape of a toroidal LPG tank using the finite element method." *Hidraulica Magazine*, no. 1 (March 2020): 21-32.

[20] Ţălu, Ştefan, and Mihai Ţălu. "Numerical analysis of the influence of uniaxial compression loads on the shape of a toroidal LPG tank." *Hidraulica Magazine*, no. 1 (March 2020): 47-58.
[21] Ţălu, Mihai, and Ştefan Ţălu. "Stress and deformation analysis under bending and torsional loads of a toroidal LPG tank based on the finite element analysis." *Hidraulica Magazine*, no. 1 (March 2020): 88-101.
[22] Patel, Pankit, and Jaypalsinh Rana. "Design & optimization of LNG-CNG cylinder for optimum weight." *IJSRD - International Journal for Scientific Research & Development* 1, no. 2 (2013): 282-286.
[23] Oprițoiu, Petre. "Comparative study of the effect of the compression and traction loads on the stress and deformation of a toroidal LPG tank." *Hidraulica Magazine*, no. 2 (June 2021): 15-28.
[24] Ţălu, Mihai, and Ştefan Ţălu. “3D geometrical solutions for toroidal LPG fuel tanks used in automotive industry.“ *Advances in Intelligent Systems Research* 151 (2018): 189-193. DOI: 10.2991/cmsa-18.2018.44.
[25] Ţălu, Ştefan, and Mihai Ţălu. “Constructive CAD variants of toroidal LPG fuel tanks used in automotive Industry.“ *Advances in Intelligent Systems Research* 159 (2018): 27-30. DOI: 10.2991/mmsa-18.2018.7.
[26] Ţălu, Ştefan, and Mihai Ţălu. “The Influence of corrosion on the vibration modes of a pressurized fuel tank used in automotive industry.“ *DEStech Transactions on Materials Science and Engineering* (2018): 1-6. DOI: 10.12783/dtmse/icmsa2018/20560.
[27] Ţălu, Mihai, and Ştefan Ţălu. “Optimal engineering design of a pressurized paralepipedic fuel tank.“ *Annals of Faculty of Engineering Hunedoara - International Journal of Engineering,* Tome XVI, Fascicule 2 (2018): 193-200.
[28] Ţălu, Ştefan, and Mihai Ţălu. “CAD generating of 3D supershapes in different coordinate systems.“ *Annals of Faculty of Engineering Hunedoara - International Journal of Engineering,* Tome VIII, Fascicule 3 (2010): 215-219.
[29] Ţălu, Ştefan, and Mihai Ţălu. “A CAD study on generating of 2D supershapes in different coordinate systems.“ *Annals of Faculty of Engineering Hunedoara - International Journal of Engineering,* Tome VIII, Fascicule 3 (2010): 201-203.
[30] Oprițoiu, Petre. "Analysis of stresses and displacements in the deformed bent 3D hexagonal toroid with regular hexagonal cross-section used in manufacturing of lpg storage tanks." *Hidraulica Magazine*, no. 2 (June 2020): 15-26.
[31] Ţălu, Ştefan. *AutoCAD 2017*. Cluj-Napoca, Napoca Star Publishing House, 2017.
[32] Oprițoiu, Petre. *Research on heat transfer and pressure losses through porous metal heat exchanger / Cercetări privind transferul termic și a pierderilor de presiune la un schimbător de căldură din metal poros.* PhD thesis, Technical University of Cluj-Napoca, Romania, Faculty of Mechanics, 2014.
[33] Oprițoiu, Petre. “Fluid flow and pressure drop simulation in aluminium foam heat exchanger.” *Acta Technica Napocensis: Civil Engineering & Architecture*, no. 50 (2007): 101-112.
[34] Oprițoiu, Petre. "Heat transfer performance analysis in porous heat exchanger." *Hidraulica Magazine*, no. 3 (September 2015): 32-41.
[35] Oprițoiu, Petre. "Rans simulation of combined flow and heat transfer through open-cell aluminum foam heat sink." *Hidraulica Magazine*, no. 3 (September 2013): 15-25.
[36] Oprițoiu, Petre. "Prediction of turbulent flow using upwind discretization scheme and k-ε turbulence model for porous heat exchanger." *Hidraulica Magazine*, no. 2 (June 2016): 88-97.
[37] Oprițoiu, Petre. “Validation of porous heat exchanger simulation model.” Paper presented at 21st International Conference and Exhibition of Hydraulics and Pneumatics HERVEX 2014, Călimănești-Căciulata, Romania, November 5-7, 2014.

# Efficacy of Using the Loss Factor to Estimate the Power Requirements of Wind and Water Tunnels with Varying Cross Sections

PhD. Student Eng. **Alexander BARON VON HOHENHAU**[1,*]

[1] Department of Mechanical Engineering, Technical University of Cluj-Napoca

[*] alex@edesigns.co.uk

***Abstract**: Estimations of power requirements in wind tunnels are based on the assumption that pressure losses are proportional to the square of the flow velocity. This assumption is invalid for certain flow conditioners, particularly honeycombs and wire screens. Therefore, current methods of estimating power requirements across a range of flow velocities are, theoretically, prone to errors. This paper will review the existing approaches and show that the resulting inaccuracies are small. Furthermore, best-practice suggestions are given to further minimise the impacts of these errors on wind tunnel design.*

***Keywords**: Power requirements, loss factor, wind tunnel, water tunnel*

## 1. Introduction

In the design stage of building a wind or water tunnel, it is essential to predict the power requirements and pressure losses of the facility. Without an accurate estimation of these characteristics, designers run the risk of including the wrong size or even type of flow fan.
The source of energy losses in wind tunnels are diverse but generally come in two categories: losses caused by the facility's geometry and losses due to the flow conditioners placed within the machine. The former includes components such as nozzles (contracting sections), diffusers (expanding sections), turns and straight sections. Flow conditioners are devices used to modify flow characteristics to improve the experimental environment. For instance, wire screens are used to increase flow uniformity, honeycombs are used to decrease turbulence, and turning vanes decrease energy losses within turns.
Extensive literature exists on the pressure losses of all of these flow conditioners. Barlow's "Low-Speed Wind Tunnel Testing" in particular, is an invaluable source of information [1]. While existing publications consider the impact of varying cross-sectional areas, they assume that losses are proportional to the square of the flow velocity. However, this relationship is only valid for certain types of flow conditioners. The work herein will assess the impact on real-world power requirements when this assumption is invalid.

## 2. Adapting the Pressure Loss Factor

As flow passes through various components in a wind tunnel, static pressure (potential energy) is converted to heat through drag and turbulence. This change in pressure is said to be energy that is *lost* to the system. The amount of energy lost by a specific component can be described by the loss factor. The relationship between the drop in pressure ($\Delta p$), loss factor ($K$), fluid density ($\rho$), and velocity ($U$) is shown in equation (1).

$$\Delta p = \frac{1}{2} K \rho U^2 \tag{1}$$

If there is a change in velocity or area, as is the case in diffusers and nozzles, the upstream conditions should be used as a basis for calculations. Multiplying both sides of the equation above by the volumetric flow rate ($Q$) yields equation (2).

$$Q\Delta p = \frac{1}{2} Q K \rho U^2 \tag{2}$$

Equation (5) is derived by substituting the relationships for power ($P$) and volumetric flow rate ($Q$) into equation (2), where $A$ is the cross-sectional area.

$$P = Q\Delta p \tag{3}$$

$$Q = AU \tag{4}$$

$$P = \tfrac{1}{2}\rho KAU \tag{5}$$

If there are multiple components in a flow circuit, with various areas, velocities, and loss values, the total power requirement can be estimated using equation (6), assuming incompressible flow. Different subscripts represent distinct wind tunnel locations.

$$P = \sum_{i=1}^{n} \frac{1}{2}\rho K_i A_i U_i^3 \tag{6}$$

As wind and water tunnels can have a large variety of different cross-sectional areas, it is advantageous to introduce the concept of a generalised local area ratio ($\mathcal{R}$). This is simply the ratio between a local area ($A_i$) and the area of the test section ($A_1$) as shown in equation (7).

$$\frac{A_i}{A_1} = \mathcal{R} \tag{7}$$

The generalised area ratio can then be used to express local areas ($A_i$) and velocities ($U_i$) in terms of test section velocity ($U_1$) and area ($A_1$).

$$A_i = A_1\mathcal{R}_\mathrm{i} \tag{8}$$

$$U_i = \frac{U_1}{\mathcal{R}_\mathrm{i}} \tag{9}$$

Substituting these ratios into equation (6), all terms can be expressed as a factor of area ratio, as shown in equation (10) and the simplified equation (11).

$$P = \sum_{i=1}^{n} \frac{1}{2}\rho K_i A_1 \mathcal{R}_i \left(\frac{U_1}{\mathcal{R}_i}\right)^3 \tag{10}$$

$$P = \sum_{i=1}^{n} \frac{1}{2}\rho A_1 U_1^3 \left(\frac{K_i}{\mathcal{R}_i^2}\right) \tag{11}$$

Rearranging these relationships in terms of main velocity results in equation (12), which indicates the flow velocity in the test section for a specific power input.

$$U_1 = \sqrt[3]{P \div \frac{1}{2}\rho A_1 \div \sum_{i=1}^{n} \frac{K_i}{\mathcal{R}_i^2}} \tag{12}$$

Keeping these relationships in mind, the following sections will detail more accurate ways of predicting pressure losses for wire screens and honeycombs.

## 3. The Loss Factor in Wire Screens

The pressure loss through a wire screen is largely dependent on the screen's porosity. The wire screen porosity ($\phi$) can be calculated using equation (13), where $d_{wt}$ is the wire thickness and $d_{wp}$ is the wire pitch.

$$\phi = \left(1 - {d_{wt}}/{d_{wp}}\right)^2 \tag{13}$$

The way the wires are woven also has a slight impact on performance, but this work will focus on the standard plain weave type screens. Based on the screen's porosity and weave-type, the method outlined by Wu et al. can be used to estimate the pressure loss [2]. This approach ignores the sinusoidal structure of the wires caused by weaving the screen and therefore slightly underestimates porosity. In addition to porosity, the surface area to volume ratio ($S_v$) has to be found using equation (14), where $d_{wn}$ is the number of wires per linear metre.

$$S_v = \sqrt{\frac{1}{d_{wn}^2} + d_{wt}^2} \times d_{wn}^2 \tag{14}$$

Furthermore, the equivalent spherical diameter ($D_P$) has to be calculated using equation (15). It is essentially an estimation of the size of the sphere required to influence the flow to the same extent as the particular wire screen.

$$D_P = 6/S_v \tag{15}$$

Once these parameters have been determined, the specific Reynolds Number ($Re_w$) of the wire screen may be calculated using equation (16). As per usual, $U$, $\rho$ and $\mu$ represent fluid velocity, density and dynamic viscosity respectively.

$$Re_w = \frac{(1-\phi)D_P U \rho}{\mu} \tag{16}$$

After $Re_w$ has been obtained, and the mesh thickness $d_m$ has been measured, the pressure drop $\Delta P$ can be found by estimating the viscous ($\mathrm{K_{SD}}$) and inertial ($\mathrm{K}_{SF}$) porous resistance.

$$\Delta P = K_{SD} + K_{SF} \tag{17}$$

$$K_{SD} = \left[250\frac{1-\phi}{Re_w}\right] \times \left[\frac{d_m U^2 \rho (1-\phi)}{\phi^3 D_P}\right] \tag{18}$$

$$K_{SF} = \left[1.69\left(\frac{1-\phi}{Re_w}\right)^{0.71}\right] \times \left[\frac{d_m U^2 \rho (1-\phi)}{\phi^3 D_P}\right] \tag{19}$$

From a dimensional analysis of equations (18) and (19) it is clear that the pressure loss in wire screens is not proportional to the square of the velocity. The viscous resistance is proportional to $u$, while the inertial resistance is proportional to $u^{1.29}$. As will be shown later, assuming a constant standard loss factor can lead to a slight underestimation of pressure loss.

## 4. The Loss Factor in Honeycombs

Honeycombs for flow conditioning come in various shapes and sizes as shown in Fig. 1. For these honeycombs, given a ratio of tube length ($L$) to hydraulic diameter ($D_H$) of $L/D_H = 6.0$, the loss factors are 0.30, 0.22, and 0.20 respectively [1]. As these loss factors are limited to specific honeycomb lengths, a more thorough exploration of the loss factor will follow.

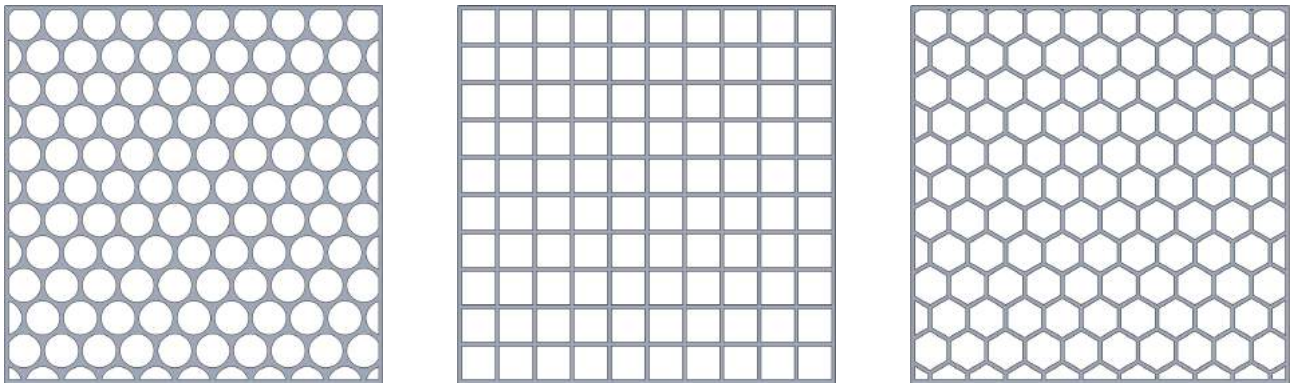

**Fig. 1.** Tubular honeycomb (left), rectangular honeycomb (centre), and hexagonal honeycomb (right).

The analysis herein will be based on the common tubular honeycomb, which is comprised of thin-walled tubes arranged in a hexagonal pattern. The main geometric characteristics of this honeycomb type are shown in Fig. 2.

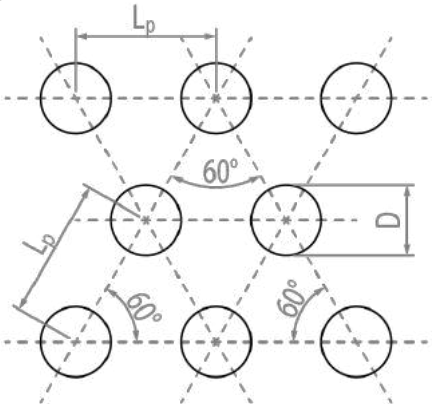


**Fig. 2.** Geometry of a honeycomb consisting of thin-walled tubes in a hexagonal arrangement, with internal diameter ($D$) and pitch ($L_p$).

Using tube pitch ($L_p$) and tube internal diameter ($D$) the porosity of the honeycomb ($\phi$) can be calculated using equation (20) [3].

$$\phi = 0.9069 \times D^2 \div L_p^2 \tag{20}$$

Various methods can be used to predict the pressure drop across honeycombs. The work herein will focus on the publications of Innocentini et al. [4], as well as Eckert et al. [5].

### 4.1 Adapting Innocentini's approximations to Tubular Honeycomb

Innocentini approximation is an adaption of Ergun's equation, which itself is used to predict the pressure drop across densely packed granular media, such as crushed glass filters. In contrast, Innocentini investigates web-like filament structures and therefore aimed to replace mean particle diameter ($d_p$) with the specific surface ($S_V$), i.e., the total particle surface per unit volume of the particle. However, tubular honeycomb is more structured and its hydraulic cylinder ($d_c$), the cylindrical form of the hydraulic diameter, can easily be calculated as shown in equation (21).

$$d_c = 4\frac{V_{flow}}{S_w} \tag{21}$$

Here, $V_{flow}$ is the volume available for the flow (i.e., within the confines of the honeycomb, but not occupied by honeycomb material), and $S_w$ is the total wetted surface. In equation (22), this result is equated with the alternative equation for hydraulic diameter, resulting in equation (23).

$$d_c = 4\frac{1-\phi}{\phi S_V} \tag{22}$$

$$\frac{V_{flow}}{S_w} = \frac{1-\phi}{\phi S_V} \tag{23}$$

The total wetted area is the surface area of a single tube, while the volume available for flow is the imaginary *hexagonal* volume the tube occupies within the honeycomb. The specific surface can be isolated as shown in equation (24).

$$S_V = \frac{1-\phi}{\phi} \times \frac{S_w}{V_{flow}} \tag{24}$$

This results in a new expression for particle diameter, shown in equation (25).

$$d_p = \frac{6}{S_V} = 6 \times \frac{\phi}{1-\phi} \times \frac{V_{flow}}{S_w} \tag{25}$$

With this new expression for particle diameter, the viscous ($K_{HD}$) and inertial ($K_{HF}$) terms for pressure loss can be evaluated as shown in equations (26) and (27). Some literature states these terms in the way they are shown here, however, other sources show them as the fractional inverse.

$$K_{HD} = \frac{150(1-\phi)^2}{\phi^3 d_p^2} \tag{26}$$

$$K_{HF} = \frac{1.75(1-\phi)}{\phi^3 d_p} \tag{27}$$

These terms can then be used to evaluate the pressure drop, based on the length of the honeycomb ($L$), using equation (28), where $\phi$ is porosity, $d_p$ is the particle diameter, $\rho$ is the fluid density, $\mu$ is the dynamic viscosity and $U$ is the fluid velocity.

$$\Delta P = L(K_{HD}\mu U + K_{HF}\rho U^2) \tag{28}$$

Once again, it is clear that the loss factor is not proportional to the square of the velocity, but to a combination of $U$ and $U^2$ [4].

### 4.2 Adapting Tubular honeycomb losses based on Eckert's approximations

Eckert's approach is fundamentally different to the previous method and is based on empirical data of thin-walled flow straighteners (i.e., actual honeycomb structures). First, a Reynolds Number ($Re_\varepsilon$) has to be calculated based on flow velocity ($U$), honeycomb surface roughness ($\varepsilon$) and kinematic viscosity ($\nu$), as shown in equation (29).

$$Re_\varepsilon = \frac{U\varepsilon}{\nu} \tag{29}$$

A friction factor ($f_e$) can then be found based on the hydraulic diameter ($D_H$) of a single honeycomb tube using either equation (30) or equation (31).

$$f_e = 0.375\, Re_\varepsilon^{-0.1} \left(\frac{\varepsilon}{D_H}\right)^{0.4} \quad when \quad Re_\varepsilon \leq 275 \tag{30}$$

$$f_e = 0.214 \left(\frac{\varepsilon}{D_H}\right)^{0.4} \quad when \quad Re_\varepsilon > 275 \tag{31}$$

Once the friction factor has been computed, the loss factor ($K$) can be determined using (32), where $L$ and $\phi$ represent honeycomb length and porosity respectively.

$$K = f_e \left(3 + \frac{L}{D_H}\right)\left(\frac{1}{\phi}\right)^2 + \left(\frac{1}{\phi} - 1\right)^2 \tag{32}$$

The loss factor generated by this approach, once again, is not proportional to $U^2$. Below a surface roughness Reynolds number of 275, the loss factor is proportional to $U^{-0.1}$. Above said this threshold, the loss factor is assumed to be constant [5].
The main drawback of this method is its dependency on surface roughness. It is the base of the Reynolds number and is also used in every single term of the final equation. Hence, a small error in surface roughness has a large impact on the final pressure drop prediction.

### 4.3 Loss Factors in Computational Fluid Dynamic Codes

Interestingly, common computational fluid dynamics (CFD) codes such as OpenFOAM and Ansys Fluent do not use the experimentally proven methods estimations outlined above. Instead, they use the traditional Darcy-Forchheimer equation [6]. This formulation also involves a viscous ($\mathrm{K}_D$) and inertial ($K_F$) term, commonly known as the Darcy and Forchheimer terms respectively [7], and are shown in equation (33).

$$\Delta \mathrm{P} = \mathrm{K}_D \mu U + K_F \frac{1}{2} \rho U^2 \tag{33}$$

This relationship is used to estimate the pressure drop of both honeycombs and wire screens. The main difference between wire screens and honeycombs is merely the implementation. To simulate a wire screen, CFD simulations usually use a virtual internal boundary and multiply the pressure drop obtained from the Darcy-Forchheimer equation by some virtual length $L$. Honeycombs on the other hand, are simulated by declaring that certain zones within the simulation are honeycomb zones and an additional multiplication with the length of the honeycomb is not needed.

## 5. Evaluation and Discussion

The previous sections outlined more precise methods of estimating pressure losses in honeycombs and wire screens. These predictions can be used to evaluate the efficacy of estimating pressure losses based on the assumption that the loss factor is proportional to the square of the velocity. Power requirements have been calculated based on a wind tunnel cross-section of 1m$^2$.

### 5.1 Honeycombs

Some of this section is based on the honeycomb geometry used in the Deep Ocean Basin in Singapore (DOBS). The honeycomb used in this facility consists of polycarbonate tubes, with an inner diameter of 6.8mm, and a wall thickness of 0.1mm, resulting in a pitch of 7.0mm. Some experimental pressure analysis has been conducted by Agency for Science, Technology and Research (A*STAR). The length of the tubes has been assumed to be 42mm, and is therefore in line with the literary values, which are given for $L/D_H = 6.0$. Four methods of estimating the loss factor and pressure drop are compared:

- The standard method of assuming that the pressure loss factor is constant and proportional to the square of the velocity. A loss factor of 0.22 has been used as suggested by Barlow et al. [1].
- Using the Darcy-Forchheimer equation, based on the experimental findings of A*STAR. They estimated $\mathrm{K}_D = 7 \times 10^5$ and $\mathrm{K}_F = 5$.
- Using Eckert's approximation and assuming a surface roughness of 0.0025mm, which is standard for plastic Perspex and drawn tubing.
- Using Innocentini's approximation, which does not require the specification of any additional constants.

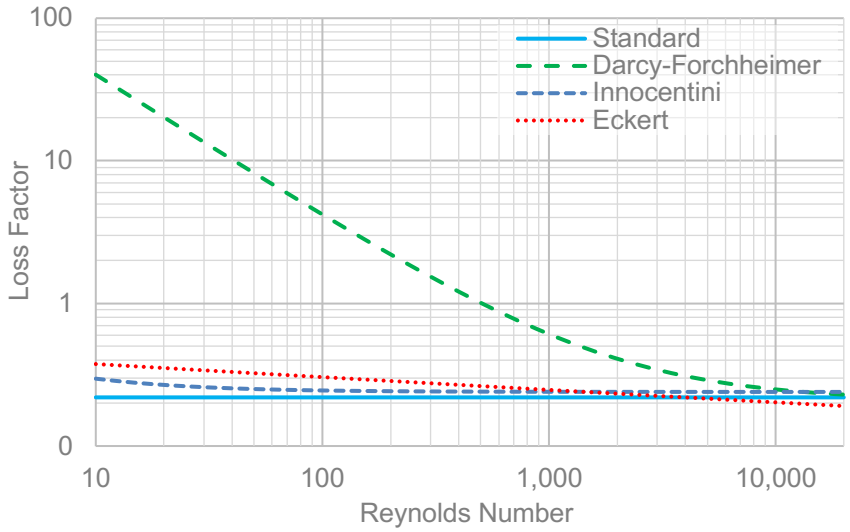


**Fig. 3.** Loss factor with increasing Reynolds number based on honeycomb tube diameter.

The change in loss factor at various flow speeds is shown in Fig. 3. It is evident, that the loss factor predicted by the Darcy-Forchheimer equation varies substantially from the other prediction. However, the predictions do converge at a Reynolds number of approximately 20,000. At this point, the standard approach, the Darcy-Forchheimer equation and Innocentini's approximation predict loss factors of 0.220, 0.230 and 0.240 respectively. The loss factor predicted by Eckert's approximation is notably lower at 0.191.
The impact of the lower loss factor generated using Eckert's approximation is clearly seen in Fig. 4. The estimated power requirements are approximately 20% lower than the other three predictions. To bring Eckert's approximation in line with the other predictions, the surface roughness would have to be increased from 2.5μm to 5.1μm. This micrometre-scale adjustment highlights the strong dependency on the surface roughness of this approach.

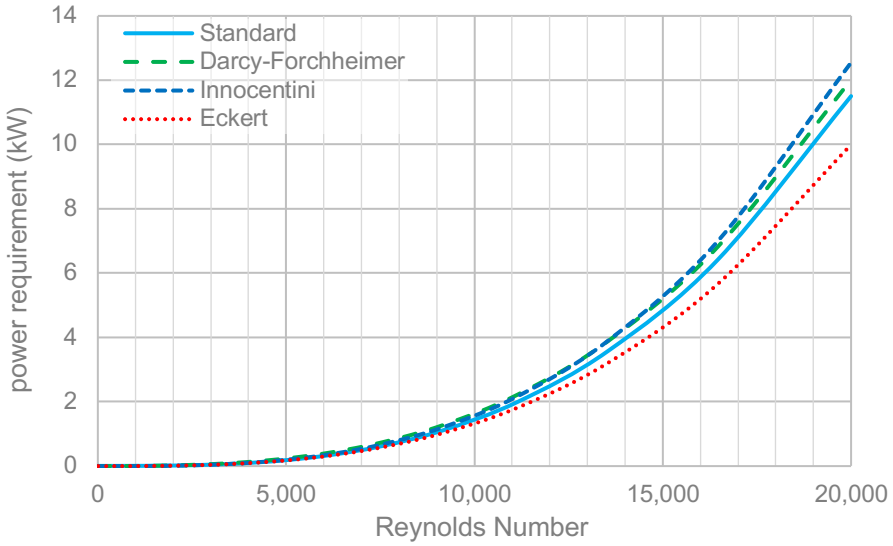


**Fig. 4.** Power requirement with increasing Reynolds number based on honeycomb tube diameter.

Both the Darcy-Forchheimer equation and standard constant loss factor prediction were based on some experimental data. Considering that the estimates generated with Innocentini's method are purely theoretical, it is remarkable how close they are to the experimental results. The proximity of these results also reaffirms the validity of using the standard loss factor to estimate pressure losses and power requirements of honeycombs in wind and water tunnels.

### 5.2 Wire Screens

The pressure drop approximation for wire screens presented by Wu et al. is an empirical equation based on a meta-analysis of various publications. As shown in Fig. 5, this loss factor does not scale with the square of the velocity. When estimating wind or water tunnel performance, it is usually most important to find the power requirements at the top flow speed of the facility, where they will be highest. Therefore, estimating the loss factor at the maximum flow velocity using Wu's approximation and assuming this value is constant throughout the various velocities, is a decent compromise. This approach is labelled as "Standard" Fig. 5.

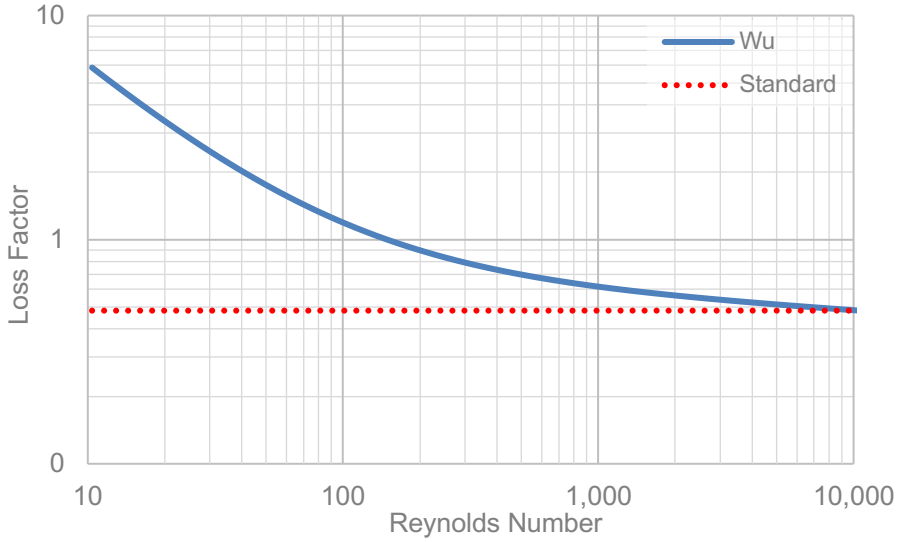


**Fig. 5.** Loss factor with increasing wire screen Reynolds Number ($Re_w$)

For the estimation of power requirements, the size of the wire screen was set at 1m$^2$. The wire thickness was assumed to be 1mm, the wire pitch is 5mm and the resulting gap is 3mm. This results in a pressure loss coefficient of 0.48 at a wire-based Reynolds number of 10,000. As is evident from Fig. 5, this is an underestimation of the loss factor below this flow speed. Nevertheless, Fig. 6 shows

that this is barely noticeable in the resulting estimation of power requirements. Therefore, it is clear that the standard approach of using the loss factor can also be used to estimate the power requirements of screens.

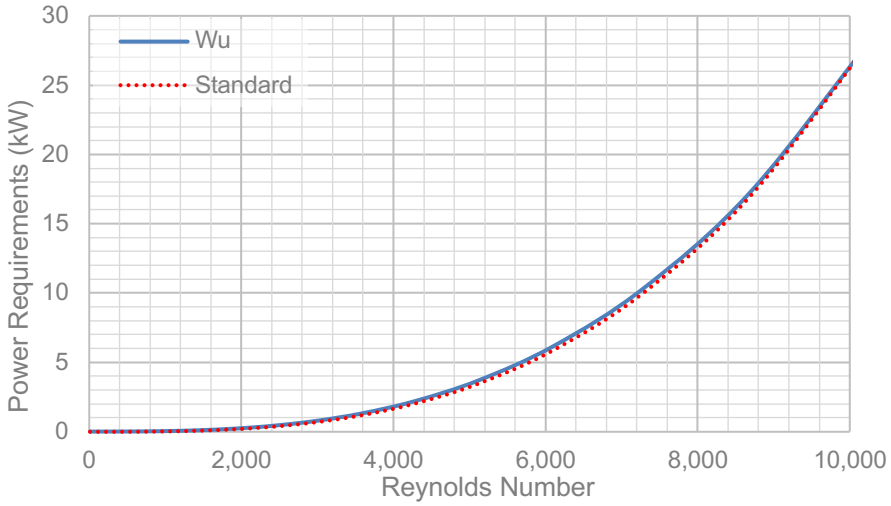


**Fig. 6.** Power requirement with increasing wire screen Reynolds Number ($Re_w$)

## 6. Conclusions

It has been shown that pressure losses and power requirements can accurately be estimated based on a standard loss factor approach. Some errors are caused by the fact that the real loss factor does not scale perfectly with the square of the velocity. To minimise these errors, the loss factor should therefore be estimated at the maximum desired flow velocity of the particular wind tunnel section. Thus, two geometrically identical wire screens would have different loss factors if they were situated in sections with different flow velocities.
The pressure loss estimations by Wu et al. are highly accurate as they are empirical equations based on a meta-analysis of multiple publications and flow velocities. Unfortunately, the same does not exist for honeycombs. If no experimental data exists, and the $L/D_H$ ratio is not equivalent to the standard 6.0, then Innocentini's approximation is a fairly accurate alternative. Eckert's approximation might be improved with a better estimation of the exact surface roughness of the honeycomb material, although further research is required to confirm.

### References

[1] Barlow, J. B., W. H. Rae, and A. Pope. *Low-Speed Wind Tunnel Testing.* New York, John Wiley & Sons, 1999.
[2] Wu, W. T., J. F. Liu, and W. H. Hsieh. "Measurement and correlation of hydraulic resistance of flow through woven metal screens." *International Journal of Heat and Mass Transfer* 48, no. 14 (2005): 3008-3017.
[3] Williams, R. *The Geometrical Foundation of Natural Structure: A Source Book of Design.* Mineola, Dover Publications, 1979.
[4] Innocentini, M. D. M. , V. R. Salvini, A. Macedo, and V. C. Pandolfelli. "Prediction of Ceramic Foams Permeability Using Ergun's Equation." *Materials Research* 2, no. 4 (1999): 283-289.
[5] Eckert, W. T., K. W. Mort, and J. Jeau. *Aerodynamic Design Guidelines and Computer Program for Estimation of Subsonic Wind Tunnel Performance*. Washington DC, National Aeronautics and Space Administration (NASA), 1976.
[6] "Darcy Forchheimer," *OpenFOAM Wiki*, March 10, 2022. Accessed February 27, 2023. https://openfoamwiki.net/index.php/DarcyForchheimer.
[7] Bejan, A. *Convection Heat Transfer.* New Jersey, John Wiley & Sons, 2013.

# Wind Action on Specific Building Structure Models of Reduced Height

Associate Professor PhD. Eng. **Fănel Dorel ȘCHEAUA**[1,*]

[1]"Dunărea de Jos" University of Galați

* fanel.scheaua@ugal.ro

***Abstract:*** *Wind action on building structures represents a real requirement on their resistance and there is a real concern on design made by the civil engineers building designers, especially when a multi-storey structure with a considerable height is considered for construction. Information provided in the design codes that specify the specific wind action values are used in the design activity. Analysis tools are also used based on the scale model of the structure being tested in the wind tunnel. The numerical analysis of air flow on the three-dimensional structure virtual model of a certain shape and size is a handy tool that can provide useful information in the design activity. This method is highlighted in this paper, which based on building models presents the results obtained from the air flow for different values of the displacement speed in the fluid region. The numerical analysis is carried out with the Ansys CFX program, and the results are presented in terms of velocity and pressure of the working fluid.*

***Keywords:*** *Air flow, 3D modelling, computational fluid dynamics (CFD)*

## 1. Introduction

The wind action on the construction structures represent a constant concern of structural engineers because it is an important parameter for these structures stability, especially if a high altitude regime is considered.
In the direction of the wind action, the idea of substituting the dynamic action of wind gusts with an action in a static regime that coincides with the positioning of the action field of distributed hydrostatic pressure on the exposed building facade was early adopted.
On the other hand, the wind dynamic effects on the construction must also be considered so that the results obtained to be comprehensive.
The direct action of the wind on the building elements is illustrated in order to identify the efforts that are formed at the level of their frontal plane positioned in the direction of action.
The cases of different constructive forms of the construction are exemplified, namely the classic building model, as well as the semi-cylindrical model in section to see the differences that appear at the level of the front wall.
The theoretical aspects are presented that show the plane potential air movement model, which involves the principles of fluid mechanics, followed by the numerical analysis carried out on virtual models of buildings of different shape, so that the hydrodynamic effort values on each individual model could be identified, depending on the specific results recorded from the air flow analyses on the specific presented cases.

## 2. Wind action in terms of velocity

The action of the wind on a structure of any shape involves an energy conversion, so that part of the total energy induced within the structure is further dissipated by the subjected structure by the direct wind action.
This energy dissipation is carried out directly through the resistance structure of the building, but special dissipation and isolation devices can also be used precisely to prevent the devastating effects that can follow the destructive actions of the wind at very high speeds in the case of violent storms or tornadoes.
The value of the reference wind speed, acting in a certain area, which has the ability to generate a reference pressure at the level of a building positioned in a direction perpendicular to the main direction of wind action, must be taken into account.
The following relation can be written that considers the air density (approximately 1.25 kg/m3) 0:

$$p_r = \frac{1}{2}\rho_a \cdot v_v^2 \quad (1)$$

If we refer to the wind action on the constructions in the Romania area, we must take into account the specific speed values with which the air masses move at certain altitudes in relation to the sea level.

It should be noted that based on the studies carried out, the recorded wind regime for the Romanian area can be described, based on the data collected over the last 50 years, of the influence that appears due to the oscillations in the North-Atlantic area, using aggregated records from the majority of meteorological stations located in function.

Based on the recorded values, the multiannual average values recorded over time were thus calculated, following the existing correlation between altitude and wind speed (r = 0.87), making it possible to compose a map of average annual speeds with specific values presented in Table 1 0.

**Table 1:** Specific wind velocity values recorded for specific areas

| **Wind energy potential on specific Romanian regions** | **Wind action specific velocity (m/s)** | |
|---|---|---|
| | Min | Max |
| Mountain region (Carpathians) – mountain peaks | 7 | 10 |
| Mountain region (Carpathians) depressions and valleys | 3 | 7 |
| Sea side | 5 | 7 |
| Plain areas | 3 | 5 |

As expected, the highest wind potential is presented in the area of the Carpathian Mountains, as well as for the Black Sea coast area, where also the highest values of wind turbulence are recorded.

Other specific areas are represented by the plains regions, where medium-intensity wind actions with lower turbulence values are recorded, thus being suitable for the installation of wind turbines.

The highest wind speed values are recorded in spring (March), and the lowest in summer in (August).

For buildings of a certain shape, we expect to obtain different wind action depending on the shape of the building façade that the wind meets, and to exemplify these aspects, the cases shown in figure 1 are considered.

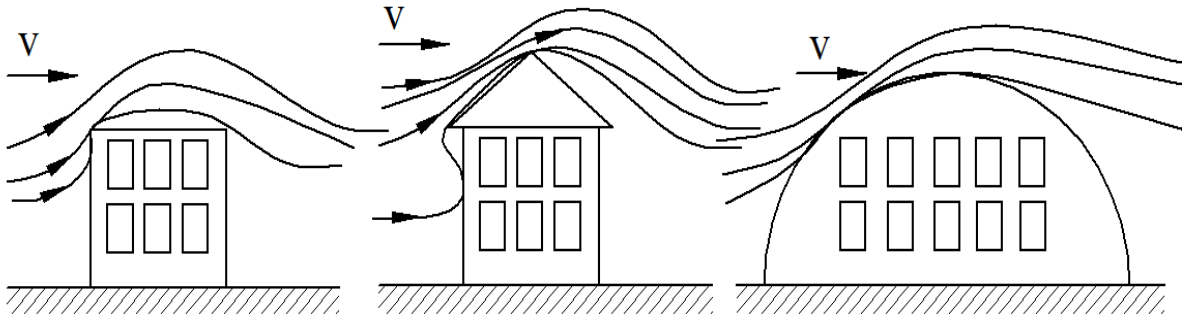


**Fig. 1.** The main building models considered for analysis

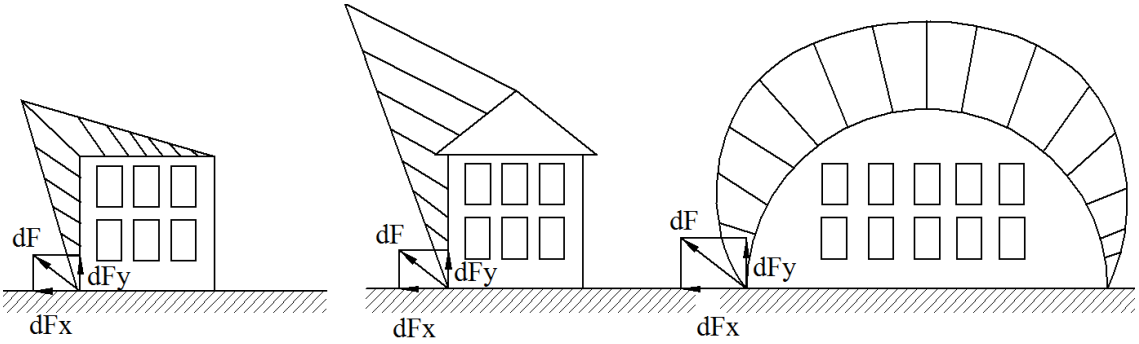


**Fig. 2.** Efforts considered and formed at the level of building models

The force acting on the front wall of the construction is actually the resultant of all the forces $d\bar{F}$ acting on the elemental surface level dS 0.

$$\bar{F} = \int_A d\bar{F} \tag{2}$$

The distribution of pressure values that form on the wall subjected to the action of the wind must be considered, as well as the velocity values recorded on the exposed contour.
The total velocity can be described by means of the following relations:

$$v = v_x + iv_y \tag{3}$$

$$v = \sqrt{v_x^2 + v_y^2} \tag{4}$$

Stagnation points located on the ground where the velocity is zero are thus considered, as well as the areas where the velocity has a maximum value, being represented by the points of maximum exposure located on the building façade.
The distribution of pressure values on the surface of the building on which the wind acts can be illustrated by writing Bernoulli's equation between a stagnation point located at the base of the building characterized by values $(p_0, v = 0)$ and some point on the surface of the pediment of values $(p, v)$, neglecting mass forces 0, 0:

$$p_o = p + \rho\frac{v^2}{2} \tag{5}$$

$$p_o - p = \rho\frac{v^2}{2} \tag{6}$$

### 3. The turbulent character of air masses circulation

The action of the wind implies a strongly turbulent movement of the air masses, resulting in a continuous mixture of them, which implies frictional forces between the layers but also with the land that manifests itself from the surface of the land up to approximately 1000 m altitude.
These turbulent movements of the atmospheric masses register changes in the speed values, and by following the action directly on the buildings, it can be considered an intensity of action in the turbulent field on them.
The wind turbulence intensity value is related to the geometric elevation and can be defined as a ratio between the change in the instantaneous speed values and the average wind action values 0, 0:

$$I_{tv}(z) = \frac{\Delta_v}{v_m(z)} \tag{7}$$

Since the action of the wind undergoes substantial changes over time, it is important to establish the maximum pressure value that can be applied to a structural model located on the main direction of action. And this phenomenon is obtained in gusts of wind.
We will also see on the results of the numerical analyzes that are carried out for the air flow on a virtual model how the pressure values are obtained at the level of the exposed facade, while on the opposite facade pressure values that coincide with a depression (low pressure values) are recorded.

**4. Interaction between wind and structure**

A wind action of a certain magnitude can produce a response close to resonance, especially for structures that benefit from increased flexibility.
It can be considered that for this wind action on a specific building with a certain degree of height, the resultant force, acting on the facade in the static domain at a reference height measured from the ground, receives a structure response quantified by the dynamic response coefficient of the construction being described by the relation 0, 0:

$$F_r = \gamma_{ex} \cdot c_r \cdot c_f \cdot p_d(z) \cdot A_s \tag{8}$$

where:

$\gamma_{ex}$ - represents the exposure factor;

$c_r$ - the response coefficient of the building in dynamic mode;

$c_f$ - aerodynamic coefficient of the construction;

$p_d(z)$ - dynamic pressure as a function of elevation;

$A_s$ - the area exposed to the action.

**5. Mathematical modeling of the air masses movement**

Concerns about modeling aspects of fluid flow have existed over time, but in the 18th century flow models for ideal fluids were established by researchers such as Bernoulli and Euler 0, 0:

$$\frac{\partial v}{\partial t} + v \cdot \nabla v = -\frac{\nabla p}{\rho} \tag{9}$$

Later in the 19th century, Navier and Stokes introduced the viscosity factor into the equation of fluid motion 0, 0:

$$\frac{\partial v}{\partial t} + v \cdot \nabla v = -\frac{\nabla p}{\rho} + \nu \nabla^2 v \tag{10}$$

The English physicist Osbourne Reynolds introduces the concept of flow with average and fluctuating fluid velocity values, which led to the RANS (Reynolds Averaged Navier-Stokes) turbulent flow model 0, 0:

$$u(x,t) = \bar{u}(x) + u'(x,t) \tag{11}$$

And based on this consideration, the Reynolds stress is introduced within the fluid flow, which has the possibility to appear at the level of the surface of the particle in motion, being described as follows 0, 0:

$$\tau_{ij} = \rho \cdot \overline{u_i'} \overline{u_j'} \tag{12}$$

Based on these considerations, several mathematical models have been developed that are currently used to analyse fluid dynamics, such as $k-\varepsilon$ turbulence models, which is the most used in numerical fluid flow analysis (CFD), being based on 2 equations of transport for turbulent kinetic energy and dissipation rate of turbulent kinetic energy. The $k-\omega$ and $k-\omega SST$ models are also used for numerical flow analysis [5-11].

## 6. Air flow analysis on virtual structure model

In order to illustrate the characteristics of air movement at the buildings front area, a numerical analysis was carried out on virtual structure models, with the $k-\varepsilon$ turbulence model, considering three constructive types of structure.
Two of these models have a planar frontal plane and the third model has a semi-circular structure in section.
For the numerical analysis, air is considered as the working fluid, at atmospheric pressure, and the wind speed values are declared in three variant values, namely 3, 5 and 7 m/s.
Three distinct cases are analysed with three sets of values of the atmospheric air circulation speed resulted, being shown in Table 2.

**Table 2:** Specific information on main analysed cases and air velocity

| Structure model | Frontal area (m2) | Flow velocity (m/s) | | |
|---|---|---|---|---|
| | | Case number | | |
| | | I | II | III |
| Rectangular frontal plane | 0.09 | 3 | 5 | 7 |
| Rectangular frontal plane with roof | 0.15 | | | |
| Semicircular | 0.09 | | | |

It is expected that at the modification of air flow velocity at each structure model will result in specific pressure values registered at the structure interface at each analysed region.
The building models considered for analysis were launched into flow numerical analysis using ANSYS CFX software to highlight the air flow parameters when the air is circulated for each structure model in part.
The results are presented in terms of air velocity and pressure, specific values being recorded at the building model interface within analysed fluid regions.

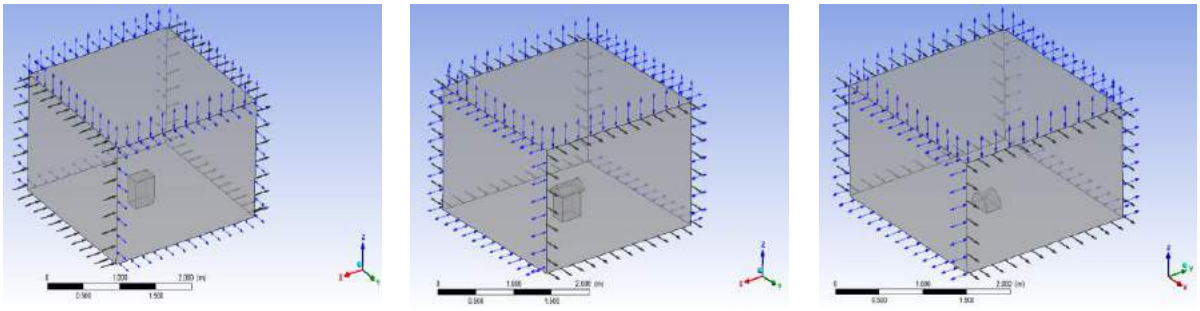

Rectangular frontal plane | Rectangular frontal plane with roof | Semicircular

**Fig. 3.** The main fluid regions considered for analysis

The flow analysis was made for air circulation at 25 degrees Celsius, with the declared velocity values (Table 1), while the reference pressure was 1 atm. Three sets of result values were obtained for the parameters that describe fluid flow through the model enclosures, being represented by pressure and velocity specific values on each analysed fluid region. The obtained numerical results are presented for the three cases in the following figures 4-6.

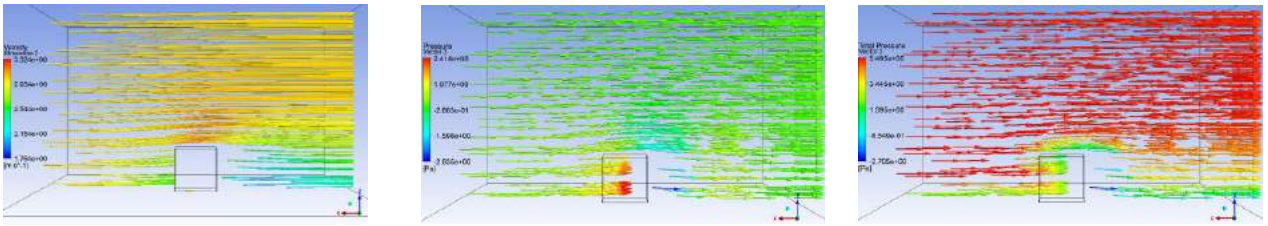

a) Rectangular structure model

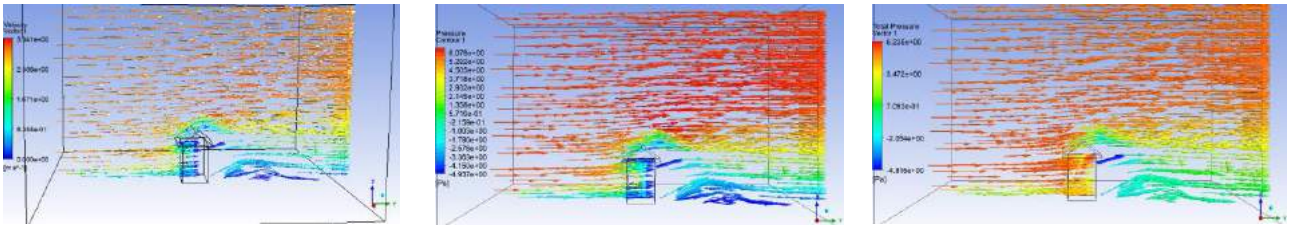

b) Rectangular structure model with roof

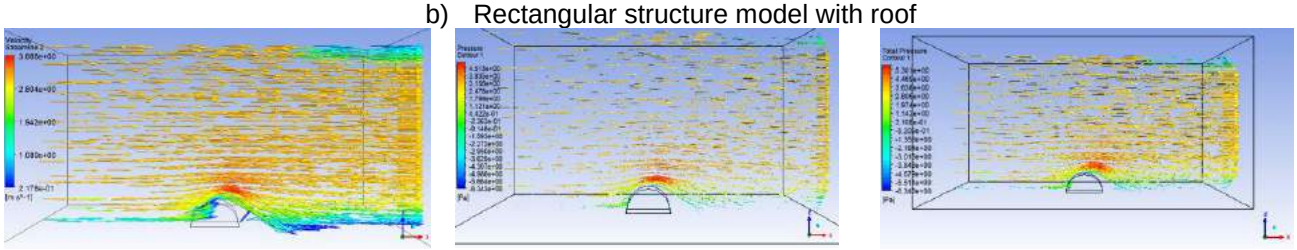

c) Semicircular structure model

**Fig. 4.** Case I (air velocity of 3 m/s)

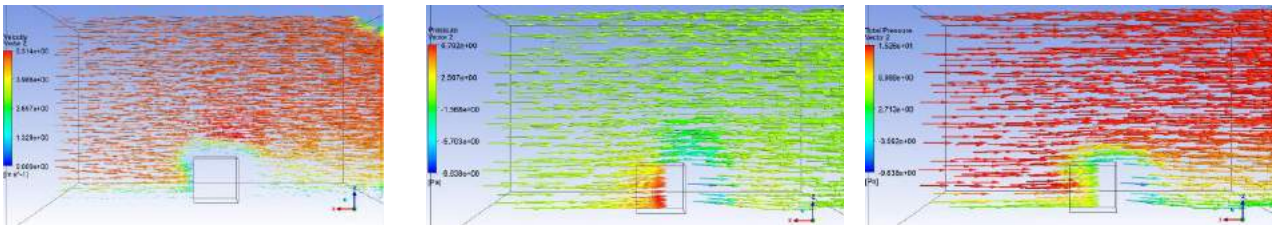

a) Rectangular structure model

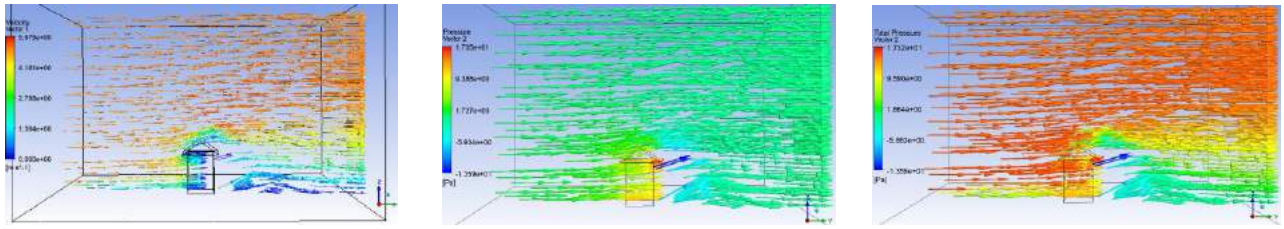

b) Rectangular structure model with roof

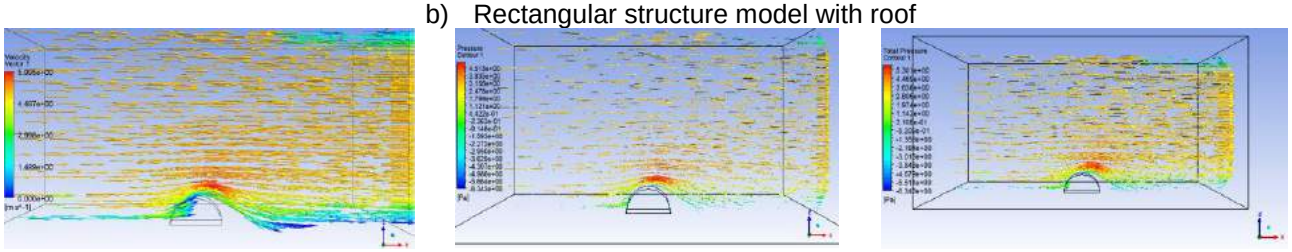

c) Semicircular structure model

**Fig. 5.** Case II (air velocity of 5 m/s)

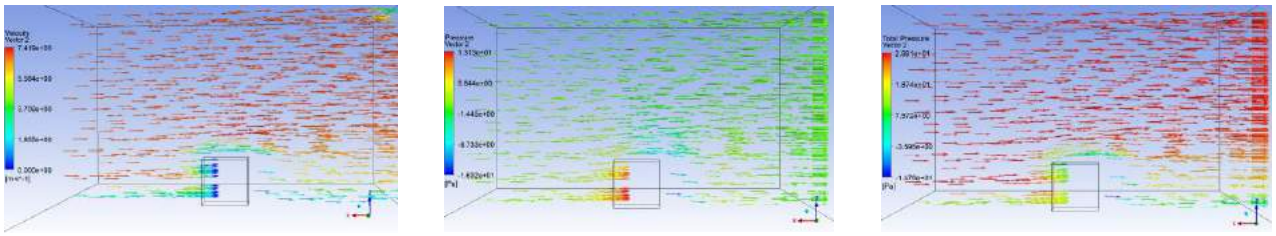

a) Rectangular structure model

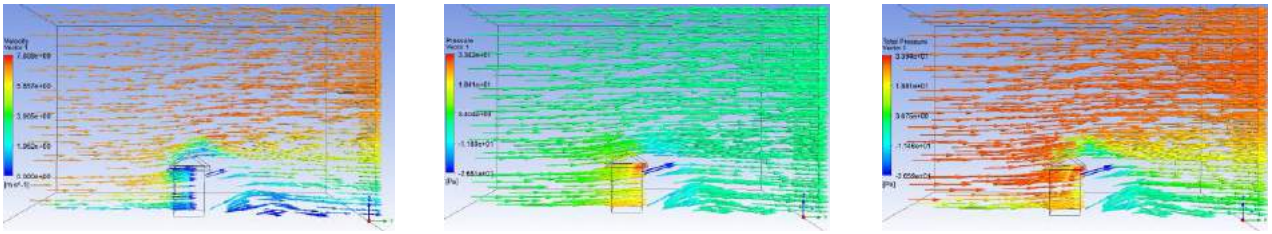

b) Rectangular structure model with roof

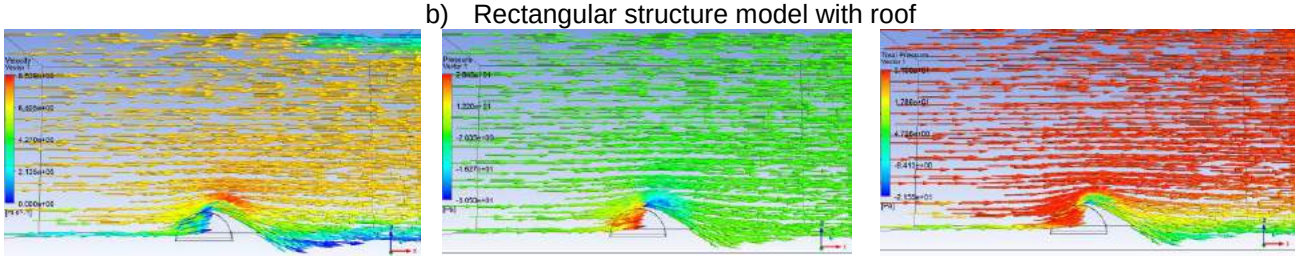

Velocity values Static pressure Total pressure

c) Semicircular structure model

**Fig. 6.** Case III (air velocity of 7 m/s)

The obtained results show the specific recorded values for the static and total pressure formed as well as for air flow velocity being noted the differences that appear between the models of the analysed structure but also between the modified values of higher velocity declared on the inlet area.
Also highlighted are the specific current lines that are formed once the air current meets the structure model analysed in part.
All these results provide results regarding the level of wind action on the respective structure model depending on the specific wind speed, thus making it possible to determine the specific efforts that can demand the structure during the direct action of the wind.

## 7. Conclusions

Theoretical aspects related to the wind action on building structures are presented in this paper and their importance in the structure design activity is highlighted, especially for buildings involving a high height regime.
Also, a numerical analysis presenting three distinct cases of building models is carried out to identify the specific parameters of the wind action at the level of the building plan when it acts with specific speed values that have been recorded over time for the wind action.
The results are presented in terms of static and dynamic pressure at the wall of the analysed building model, as well as circulation speed around the contour of the analysed building model, according to the three analysed cases with the same declared values of air input velocity.
It is thus possible to identify the differences recorded for the analysed structure models, depending on the specific values of air circulation speed declared and recorded for each individual case.
Based on the two components of static and dynamic pressure, the direct action of the wind on the respective structure model can be highlighted, and it is also possible to determine the main demands that may appear on the main action direction of the air stream on the respective model.

**References**

[1] Vasilescu, Al. A. *Fluid Mechanics* / *Mecanica fluidelor*. Galati, Ministry of Education, University of Galati, 1979.

[2] Vespremeanu-Stroe, Alfred, Sorin Cheval, and Florin Tatui. “The Wind Regime of Romania – Characteristics, Trends and North Atlantic Oscillation Influences.” *Geographic forum. Geography and environmental protection studies and research* / *Forum geografic. Studii și cercetări de geografie și protecția mediului* 11, no. 2 (December 2012): 118-126.

[3] Blaga, F. G. *The dynamic action of wind on multi-storey metal structures* / *Acțiunea dinamică a vântului asupra structurilor metalice multietajate*. Doctoral thesis. Technical University of Cluj-Napoca, Faculty of Civil Engineering, 2022.

[4] Vita, G., A. Šarkić-Glumac, H. Hemida, S. Salvadori, and C. Baniotopoulos. “On the wind energy resource above high-rise buildings.” *Energies* 13, no. 14 (2020): 3641.

[5] Micallef, D., and G. Van Bussel. “A review of urban wind energy research: aerodynamics and other challenges.” *Energies* 11, no. 9 (2018): 2204.

[6] Olabi, A. G., T. Wilberforce, K. Elsaid, T. Salameh, E. T. Sayed, K. S. Husain, and M. A. Abdelkareem. “Selection guidelines for wind energy technologies.” *Energies* 14, no. 11 (2021): 3244.

[7] Žegarac Leskovar, V., and M. Premrov. “A review of architectural and structural design typologies of multi-storey timber buildings in Europe.” *Forests* 12, no. 6 (2021): 757.

[8] Toja-Silva, F., C. Peralta, O. Lopez-Garcia, J. Navarro, and I. Cruz. “On roof geometry for urban wind energy exploitation in high-rise buildings.” *Computation* 3, no. 2 (2015): 299-325.

[9] Hemida, H., A. Šarkić Glumac, G. Vita, K. Kostadinović Vranešević,s and R. Höffer. “On the flow over high-rise building for wind energy harvesting: An experimental investigation of wind speed and surface pressure.” *Applied Sciences* 10, no. 15 (2020): 5283.

[10] Ying, X., Y. Wang, W. Li, Z. Liu, and G. Ding. “Group layout pattern and outdoor wind environment of enclosed office buildings in Hangzhou.” *Energies* 13, no. 2 (2020): 406.

[11] Kuo, C. Y., C. T. Tzeng, M. C. Ho, and C. M. Lai. “Wind tunnel studies of a pedestrian-level wind environment in a street canyon between a high-rise building with a podium and low-level attached houses.” *Energies* 8, no. 10 (2015): 10942-10957.

# Computer Modelling of an Aquatic Fauna Complex Concrete Passage at a River Barrage

Assoc.prof. dr.eng. **Albert Titus CONSTANTIN**[1,*], Assoc.prof. dr.eng. **Gheorghe I. LAZĂR**[1], PhD.stud. eng. **Cristian BRATANOVICI**[2], Lecturer dr.eng. **Șerban-Vlad NICOARĂ**[1]

[1] Politehnica University Timişoara; * albert.constantin@upt.ro

[2] Romanian Waters National Administration, Mureș Water Basin Administration

***Abstract:*** *The paper presents a 2D computer structure modelling and discharge simulation for an improved aquatic fauna passage consisting on a three compartments stepped concrete channel and considered as a side appurtenant for a small head dam on a river upper course. The foreseen structure aims to reduce the barraging environmental impact by offering optimum flow conditions under given water discharging circumstances, meaning even for ensuring the minimum required sanitary/ecological river discharge as split by the main path through the gate dam and the side passage path. The hydraulic simulation looks to establish the side passage discharge development and in the same time to estimate the extreme values of water velocity, especially at narrowing sections. In case there is necessary, the numerical results would point to further geometrical optimisation by adjusting the existing structural details or by considering additional constructive elements in order to fulfil specific requirements (usually with respect to the maximum water velocities) as indicated by in-force regulations.*

***Keywords:*** *Fish ladder, hydraulics, numerical model.*

## 1. General presentation of the studied structure

The water arrangement on the Livezeni–Bumbești mountainous sector of Jiu River [1,2], Hunedoara County, Romania, is mainly designated for hydro-power harnessing. The considered developed river area is situated between the East Jiu and West Jiu Rivers confluence (right south of Petroșani Town) and the confluence with left side Valea Sadului River tributary (towards the Town of Bumbești Jiu), stretching over about 31km in the Jiu Gorges. The Livezeni hydro-power development consists from the Livezeni Dam – a three radial gate controlled 12m gaps spillway barrage of 9m height and about 45m wide, creating an about 130000m$^3$ accumulation and endowed with water power dissipater and a left side fish ladder channel – placed on the gorges upstream entry, the water-power catchment with an underground silting basin, the 6900m length headrace of 3.80m diameter, the underground 24m height surge-tank, the gate house sheltering a high capacity butterfly valve, the 142m length and 2.95m inner diameter steel penstock and the 36m3/s installed flow and 24.5MW installed power Dumitra Power Station (surface) fitted with three Francis groups. The sanitary flow required on the river sector immediately downstream of the dam for ecological conditions is 2.70m$^3$/s.
As designed by S.C. ISPH Project Development S.A. (Hydropower Designing and Studies Institute), Bucharest, the fish passage is a concrete structure accomplished by three zones (counting in the flow direction) [1,2], the third one, as considering the upstream fish migration, being designed for fauna comfort and accommodation. At its lowest end, the side passage is connected by a rectangular free side window (about 1.95m wide by 2.40m height at the level of 539.60mSL) to the staggered blocks apron of the water energy dissipater (fig.1).
The further on presented numerical discrete modelling of the flowing phenomenon by the Livezeni Dam side fish ladder aimed to detail and enhance its initial general geometry for the structure elements, based on water velocity development as revealed over the entire 2D domain and with a closer look towards the path narrowing sections.

## 2. Accomplishment of the computer numerical model

The spatial geometrical structure, as designed and AutoCAD presented by S.C. ISPH Project Development S.A., was adopted and processed as a 2D development. The structure was than

handled in AutoCAD 3D for meshing purpose and to reveal the most concerning geometrical points, as necessary to build its numerical model. The figure 2 presents a general view of the essential structural elements, meaning the transversal stepping walls with their perpendicular opened diaphragms, defining the designed spatial geometry which was already employed by Bratanovici et al., 2019, in order to produce a 1D numerical model of the Livezeni Dam accompanying fish ladder [2]. This 1D flow phenomenon model represented a meandering path divided in numerous linear sections by vertical cross sections, path perpendicular, along the spatial structure. The numerical data of the geometrical elements and all the dividing cross sections were graphically obtained in AutoCAD 3D and the general view of the entire path was generated for the 1D model by the help of HEC-RAS v.4.1 [3], a software version that allows to consider in the background (with respect to the x0y reference system) the plane image as created and stored in a .dxf extension file (see Fig. 3).

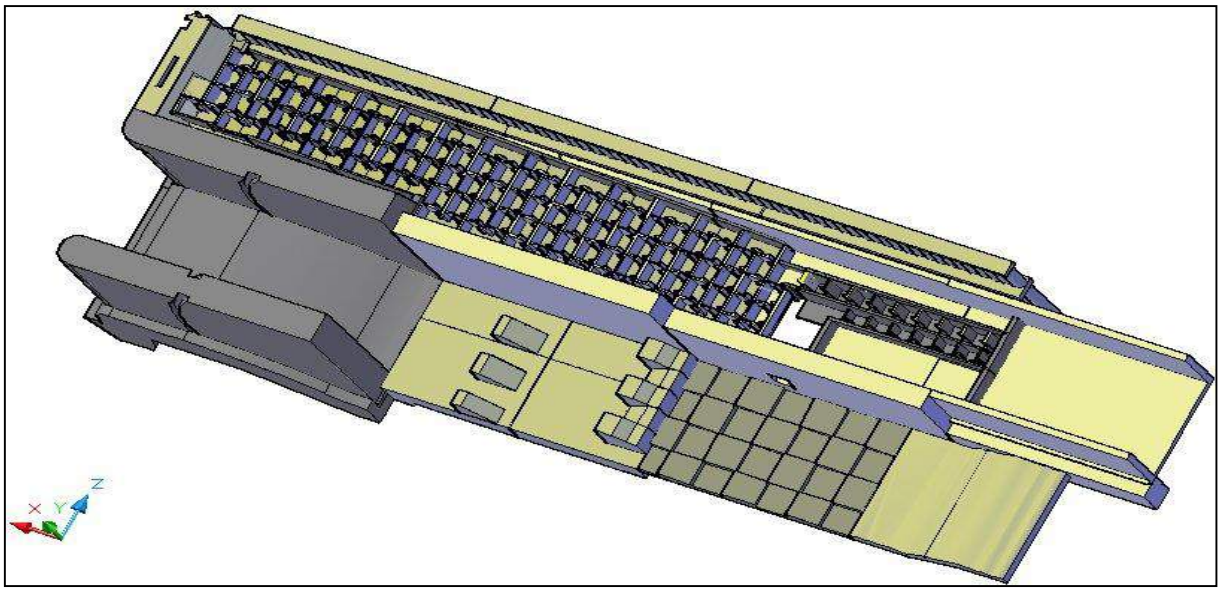

**Fig. 1.** General configuration of the fish concrete ladder aside of Livezeni Dam, partially showing the spillway barrage with its stilling basin and staggered blocks apron

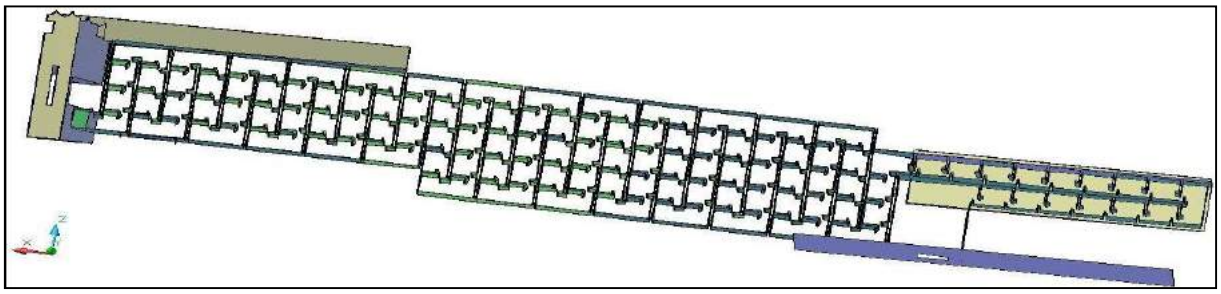

**Fig. 2.** General view of the three compartments fish ladder essential elements

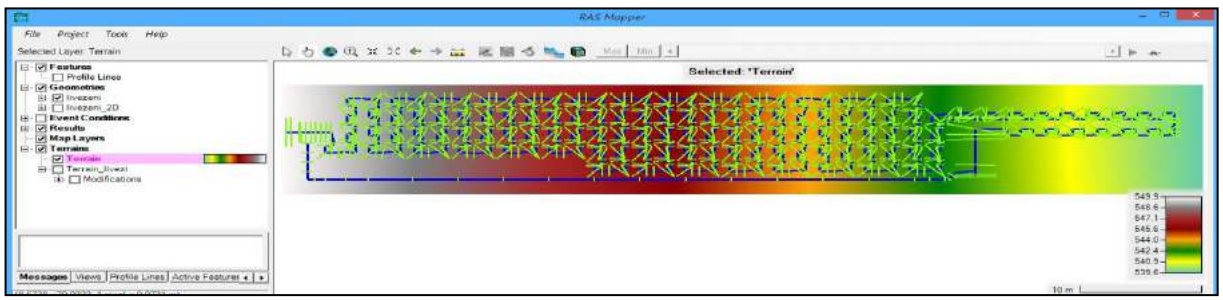


**Fig. 3.** Cross sections divided meandering flow path against the developed plan view of the 3D fish passage

As taking the modelling forward, at first the 1D numerical model is uploaded by HEC-RAS vers.6.1 [4] and there is generated a plane surface brought in 3D, as it is visible in the RAS Mapper graphical view of figure 3. A new 2D geometry is than generated in the updated software, starting with defining the 2D numerical model domain contour and by considering the meshing discrete dimensions, dx=dy=0.1m, and the associated points level with respect to the 0z direction. The Manning roughness coefficient was set as n=0.02.
Further on, the well-known Break Line facility is employed for all the narrowing sections and the outgoing section of the third compartment (upper view in fig.4), and specific aligning and narrowing sections areas rearranging operations are performed (as shown by detailed view in figure 4).

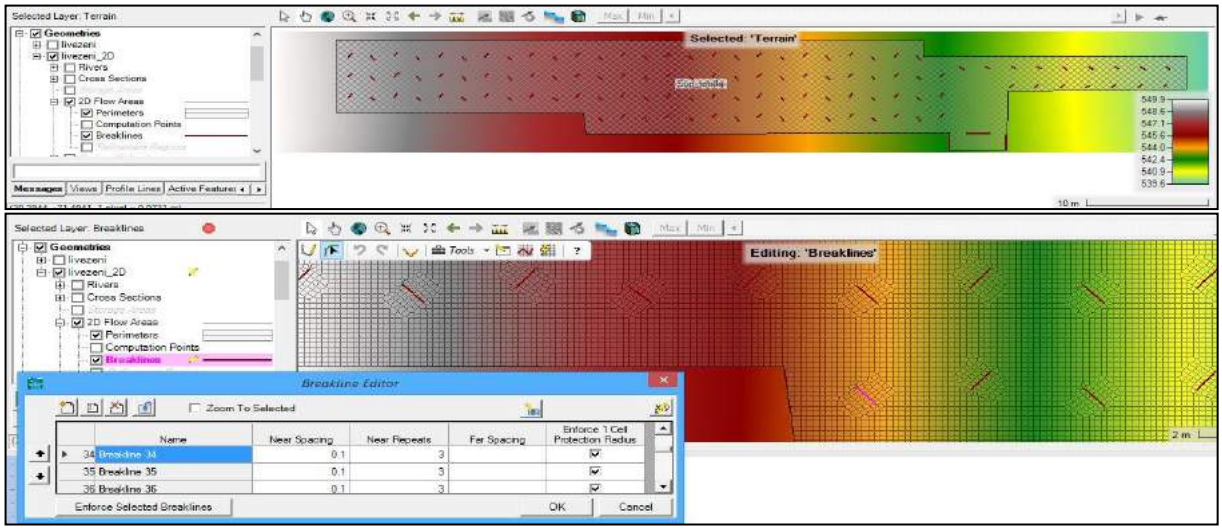


**Fig. 4.** Fish passage floor 3D development showing the 2D discrete meshing with the narrowing section assigned break lines (upper image) and the final rearranged and locally refined mesh of the flowing domain

The available background configuration as loaded for the 1D model [2] was also considered at the 2D model geometry generation. By maintaining the 1D path visible, each breaking line was one after the other introduced and the mesh was locally improved. In a similar way, by engaging the Modifications module, there were defined the contour and interior (transversal stepping) walls of each compartment (as in upper view of figure 5), the parting and narrowing diaphragms (straight and hook shape, figure 5) and the additional walls in the sides areas of the first two compartments (as in upper view of figure 6) or the floor connection area in the end of the third compartment (as in bottom view of figure 6).
There can be noticed in the bottom view of figure 5 the diaphragms adjusting way under a hook shape towards the narrowing gap (ladder compartments 1 and 2) in order to alter the water velocity range in the area. In the upper view of figure 6, one may notice the way of considering additional diaphragms on the sides of compartment 1, while the bottom view of figure 6 shows the way of adjusting the floor of the 3rd compartment as an improved connection with the 2nd compartment floor and to the weir staggered blocks apron. At this ladder downstream part, at the 3-2 compartments passing area as leaving the fauna comfort and accommodation pool, the position of a vertical wall was reconsidered (a previously designed wall got dropped, while another additional one was introduced). As a consequence, a significant drop in water velocity maximum values was reached also in this part of the fish passage. In the end, for the downstream passage entering part, a connection window – SA/2D Conn – was considered between the fauna comfort pool and the staggered blocks apron part of the Livezeni Dam water energy dissipater (the built numerical model covers just an apron part of ca. 1.60m wide which is downwards connected by a 1D linear segment of ca. 0.60m). The figure 7 presents the entire 2D discrete numerical model by which the ecological flow transition is simulated.

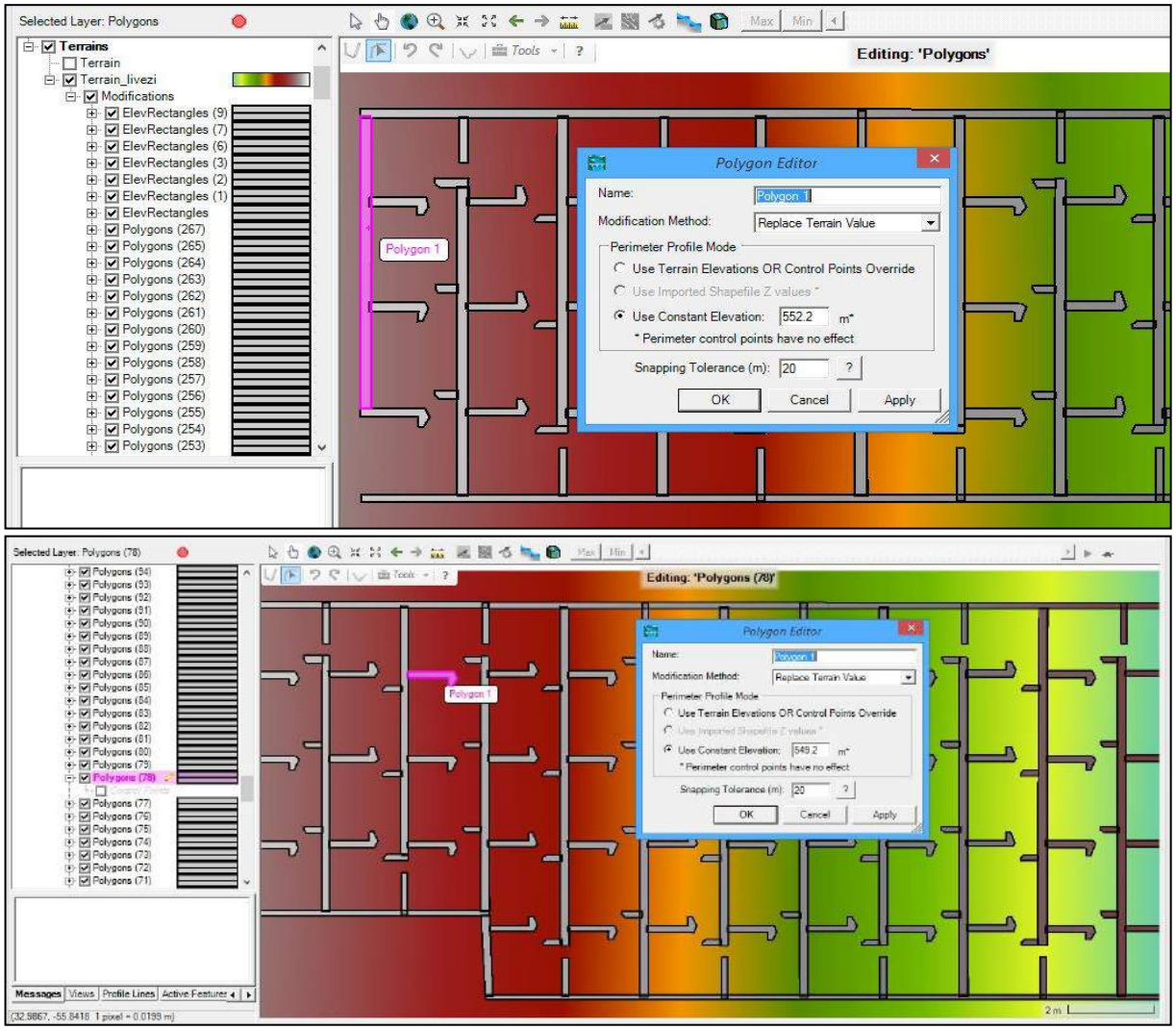


**Fig. 5.** Employment of Modification option for defining the contour and stepping walls (upper view), and the parting short and hook shape diaphragms (bottom view)

## 3. Boundary and initial conditions

As it is known for a usual study of the hydraulic phenomenon, the boundary conditions of the considered flow path are the transited discharge given as a time developed hydrograph and the total path hydrodynamic gradient. For this specific modelling, besides the transited discharge $Q_{tran}$ = 0.45m$^3$/s assigned as initial entering condition to the upper BC_Sup_total_1 edge, a complementary flow $Q_{compl}$ = 0.0935m$^3$/s was considered at the downward BC_S2D_2 edge at the passage connection with the energy dissipation basin (figure 8), also as an entering condition. In the same time, the hydrodynamic gradient from the 1D numerical model, as assigned to the downstream "0" cross section, is 0.0001035.

We have to mention that the complementary considered flow was estimated by the thumb rule as considering the enforced 2.70m$^3$/s sanitary discharge from which the 0.45m$^3$/s fish passage discharge was subtracted. As the total overflow dam crest opening is 38.5m, while the fish passage downstream basin connection gap is 1.60m wide, one can adopt $Q_{compl}$ = [(2.70-0.45)/38.5]×1.60 = 0.0935m$^3$/s.

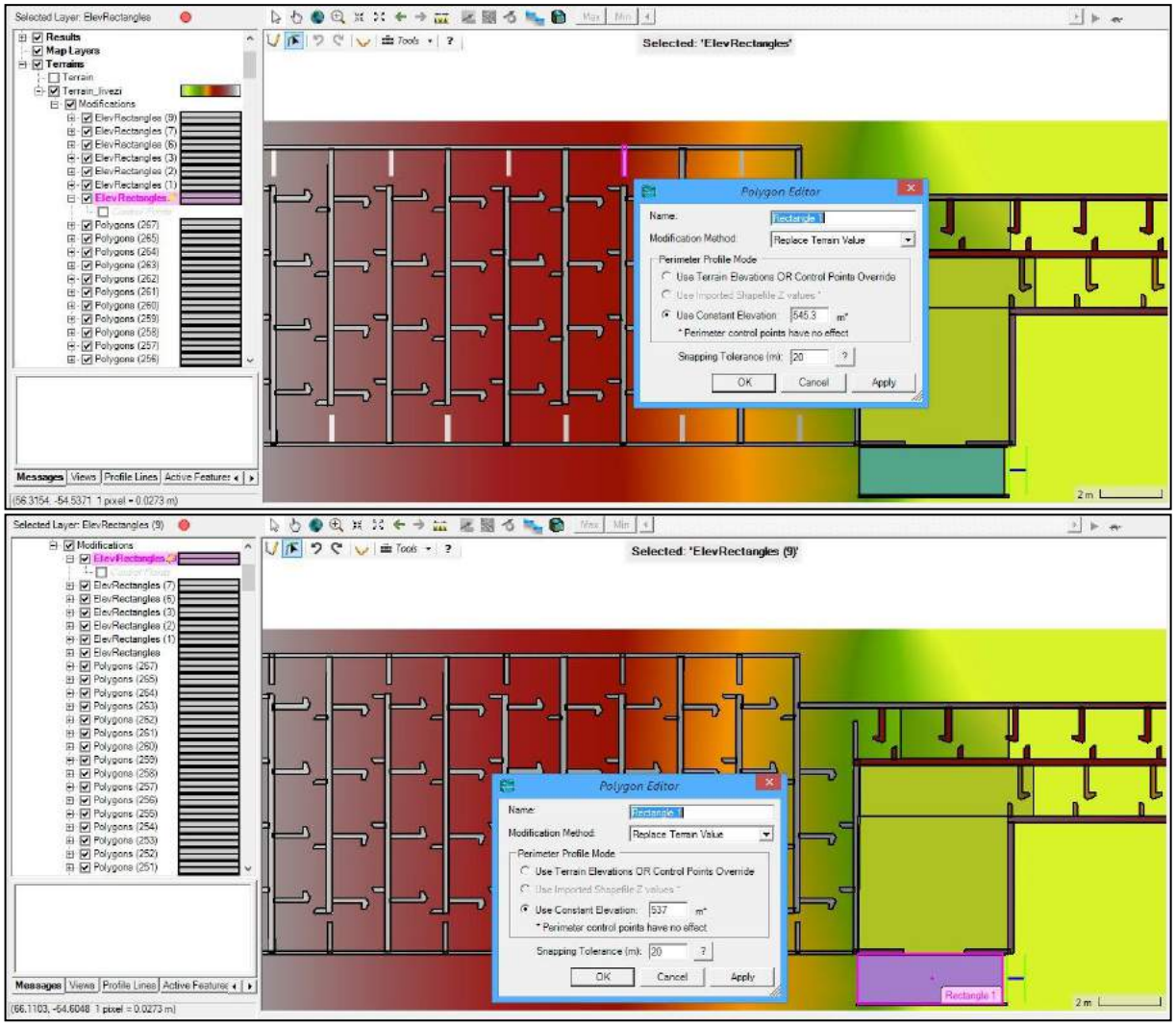


**Fig. 6.** Employment of Modification option for defining the sides narrowing walls in compartments 1 and 2 (upper view), and the walls and floor adjustments in compartment 3

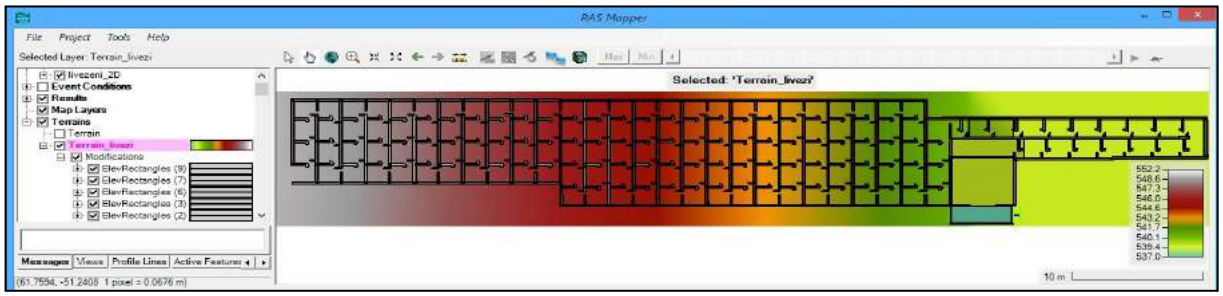


**Fig. 7.** General view of the developed Livezeni Dam associated fish ladder 2D discrete model

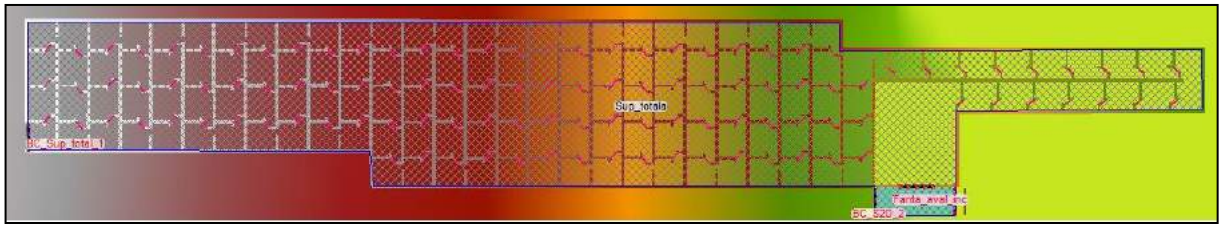


**Fig. 8.** The completed discrete model in RAS-Mapper module, showing its completed geometry against the 3D (coloured gradient) floor configuration

The actual flow transition numerical simulation by the developed discrete model was performed for a specific time interval of 1h and 40 minutes (corresponding to a given significant hydrologic phenomenon, explicitly from 01:00 to 02:40 on September 1st, 2008). The running time step was set to one second, while the mapping time was considered to 30 seconds and the resulting data storing to each 5 minutes.

## 4. Reached results of the flow phenomenon simulation

As following the computer simulation, constant and time depending values of phenomenon parameters – water levels, flow, velocity – were revealed, both for the 2D model and for the two cross sections on the 1D model.
After performing some post-processing operations, the results were organized by specific files that can be afterwards studied by graphic visualizations and by data spreadsheets.
Specifically, the following graphically processed results are presented here as corresponding to the ending moment of the simulation period: the particles trajectories against the water level development with respect to the channel floor (fig.9), the water velocity distribution revealing also its izo-lines of a 0.25m/s value step (fig.10), and the water level longitudinal development, both along a side straight profile and along the entire meandering path by the narrowing gaps (fig.11).

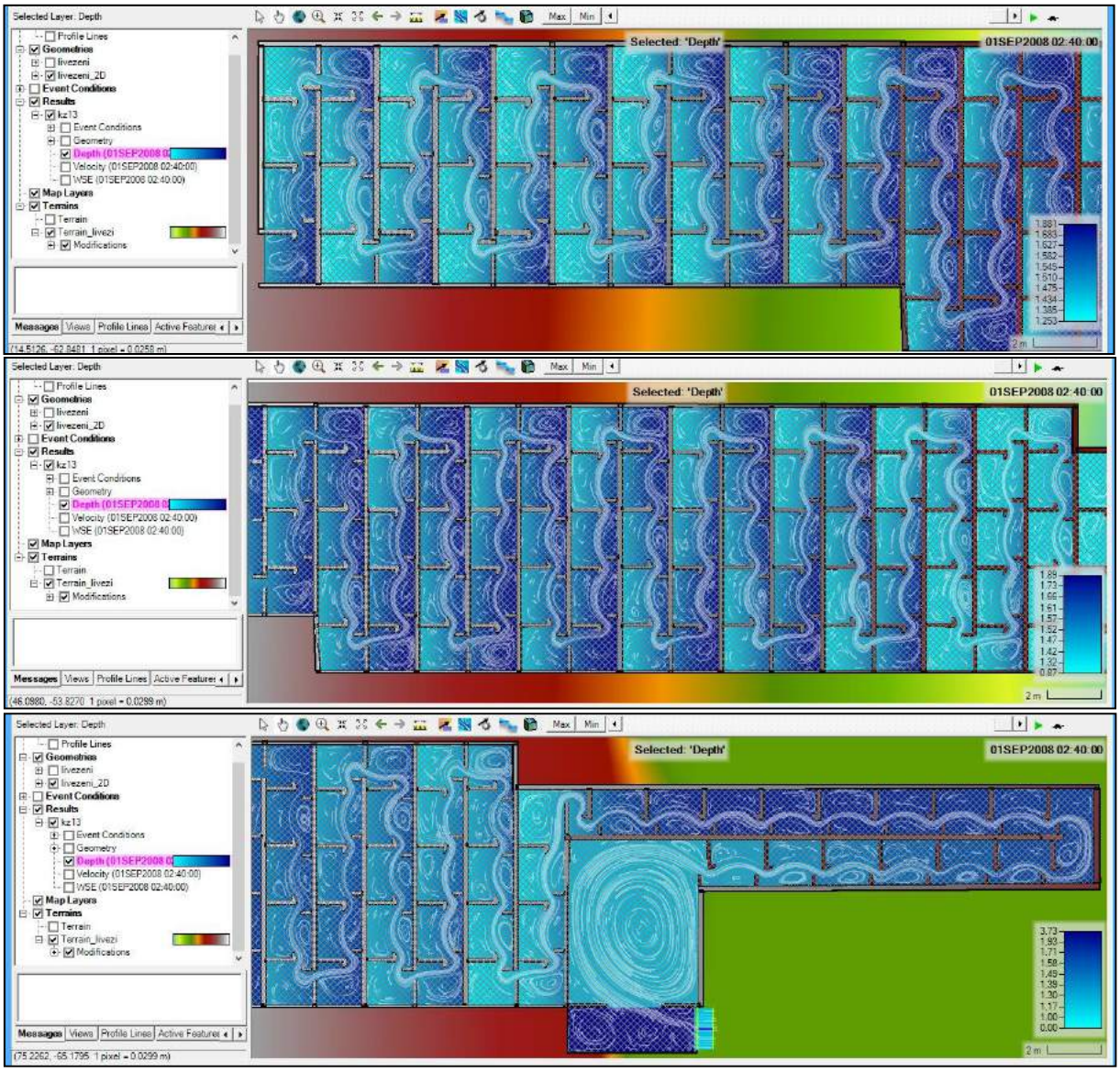


**Fig. 9.** Particles trajectories against water depth development by the three compartments (from up to down) of the modelled fish passage at the final moment of computer simulation time period

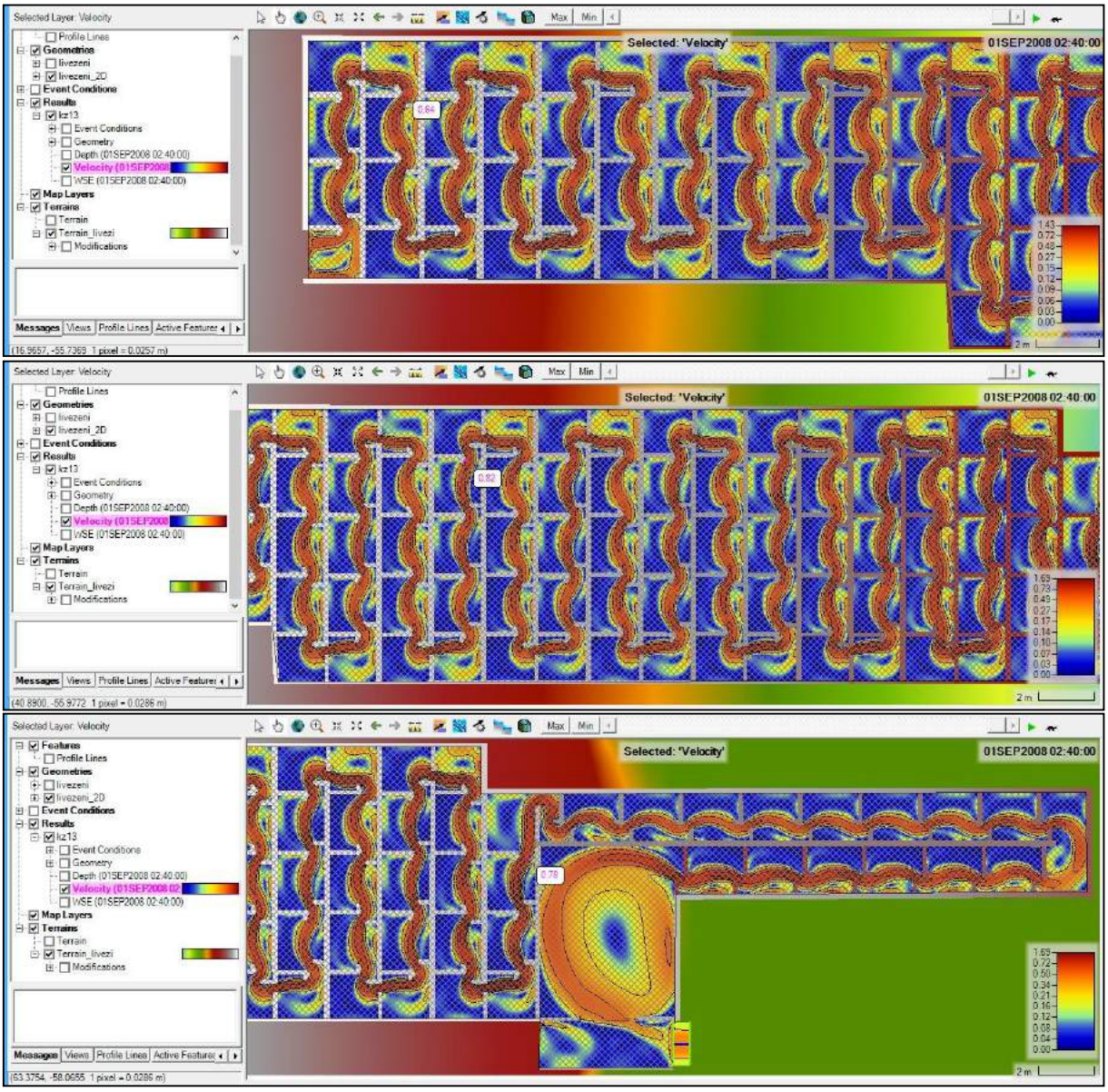


**Fig. 10.** Izo-velocity lines (0.25m/s value step) against the water velocity development by the three compartments (from up to down) of the modelled fish passage at the final moment of computer simulation time period

Some detailed views of the izo-velocity lines against the water velocity distribution, bringing up areas of extreme values in the three compartments, are presented by figure 12.

## 5. Analysis conclusions

As analysing the computer simulated water flow phenomenon by the modelled fish passage structure at Livezeni Dam, one can notice that the transition goes by a relatively slow regime along the entire meandering path. The water velocity values in the narrowing areas range generally from about 0.5 to 1.25m/s, punctually reaching a top value of 1.33m/s (fig.13). These ranging limits are to be similarly found at the narrow sections of all three compartments of the passage.
There is also mentioned that the adjustment of the hook shape at the edge of the flow transversal diaphragms on the first two modelled compartments, together with the addition of the short (90cm) narrowing diaphragms perpendicular to the sides walls (see figure 6), determine a decrease in water velocity values to about 0.5 … 0.85m/s (so better corresponding to the requesting conditions with respect to fauna) by the sides of the gaps.

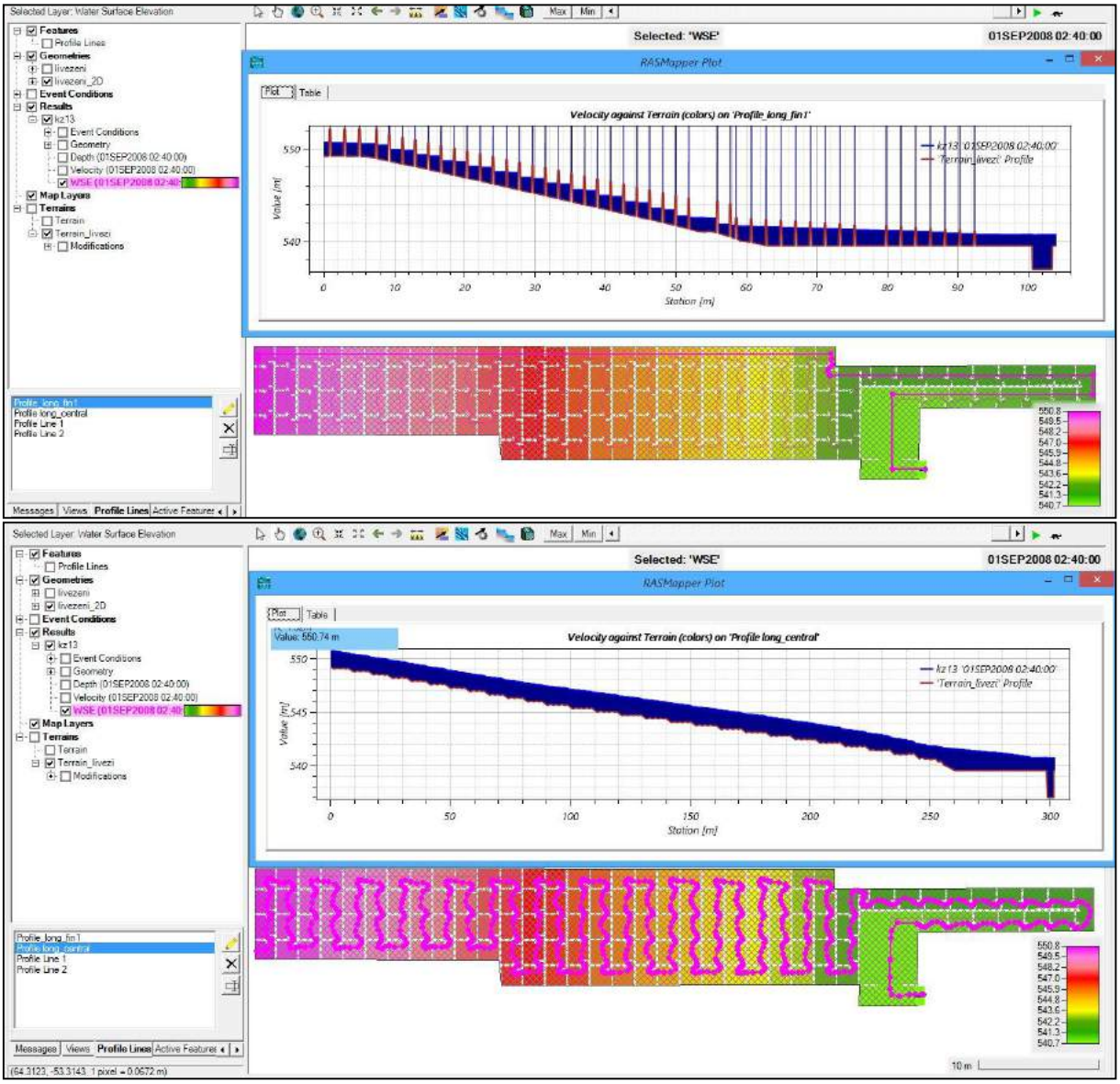


**Fig. 11.** Water level longitudinal development by the left side wall straight profile and along the entire meandering path by the narrowing gaps at the final moment of the computer simulation time period

In conclusion, we can estimate from the analysis of the computer modelling reached results that the considered fish passage structure configuration, adjusted after successively performed flow simulations under the ecological discharge of about 0.5435m$^3$/s, determines acceptable water velocity values, obeying the ranges required by nowadays regulations. Besides the necessity of the configured aquatic fauna passage as associate to Livezeni Dam, the performed study also comes in support of considering the adjoining of a micro-hydropower station to the retaining structure. As allowing it an installed discharge of about 2.40m$^3$/s under the given 12m gross hydraulic head, the hydropower equipment would show an installed power of about 220kW.

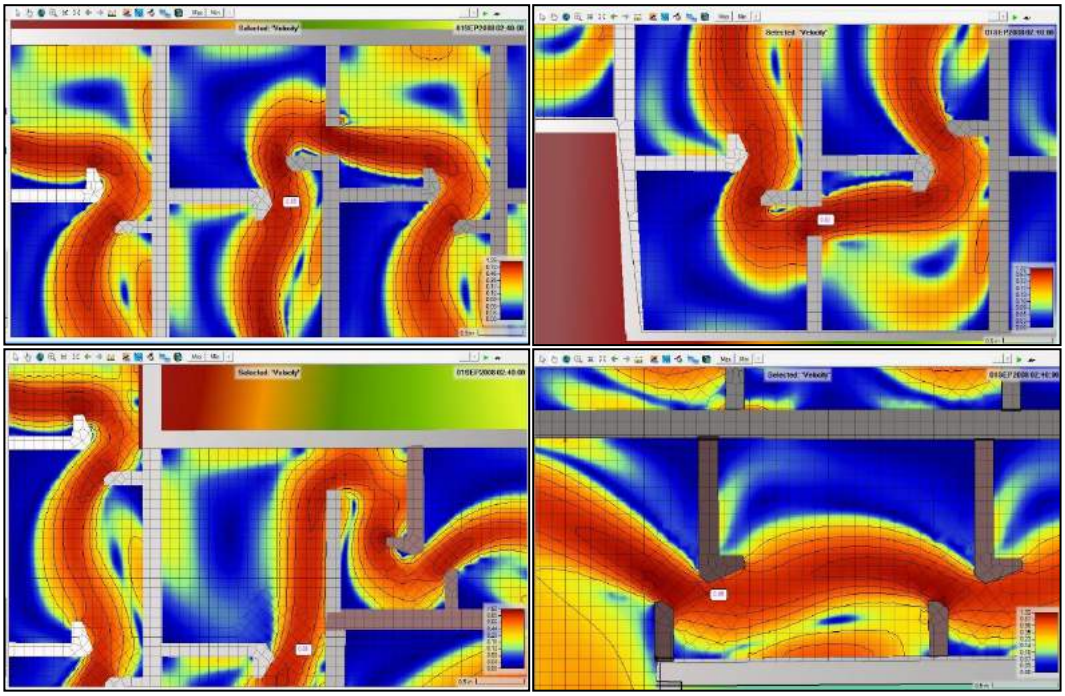

**Fig. 12.** Detailed views of specific areas of extreme water velocity values in the three compartments of the modelled fish passage: upper left – by the first compartment upstream (near the left side wall), upper right and lower left – by the second compartment (towards the right side wall and the left side one, respectively), lower right – by the third compartment (towards the downstream side of the apron structure)

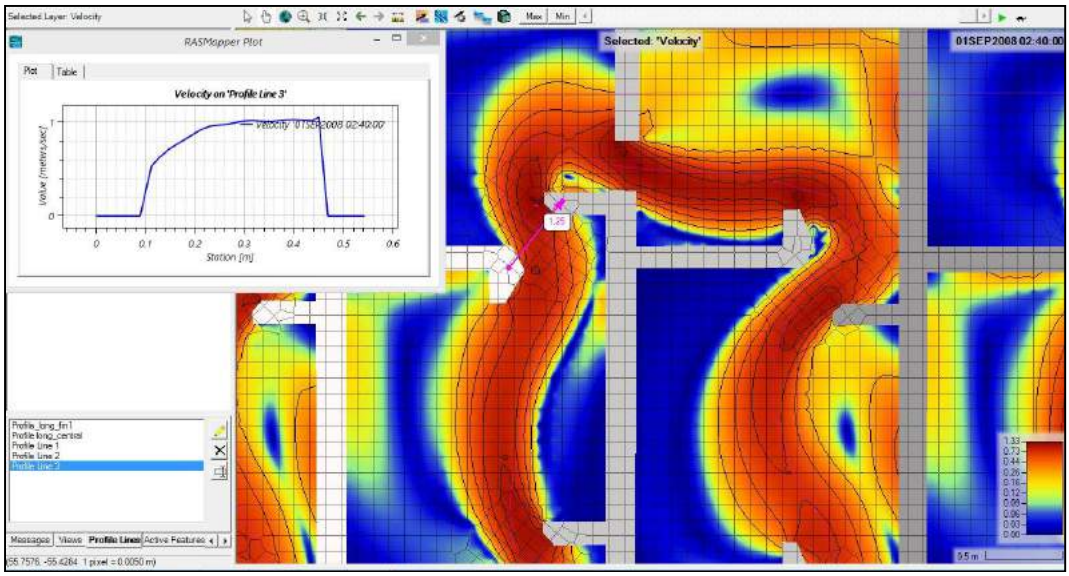


**Fig. 13.** Water velocity distribution detailed view at some narrowing areas in the upstream first passage compartment, near the left side wall

**References**

[1] ***. *Amenajarea hidroenergetică a râului Jiu pe sectorul Livezeni – Bumbești / The hydropower arrangement of Jiu River on Livezeni – Bumbești sector*. S.C. Hidroconstrucţia S.A., Bucharest, 2016.

[2] Bratanovici, C., I.A. Popescu-Buşan, Gh. Lazăr, A.T. Constantin, and Ș.V. Nicoară. “Numerical study of the water discharge on a fish stepped passage at a low head dam.” *IOP Conference Series: Earth and Environmental Science* 362 (2019): 012150. Paper presented at World Multidisciplinary Earth Sciences Symposium (WMESS 2019), Prague, Czech Republic, September 9–13, 2019.

[3] Brunner, G.W. *HEC–RAS 4.1 River Analysis System, Hydraulic Reference Manual*. US Army Corps of Engineers, 2002.

[4] ***. *HEC-RAS River Analysis System, Version 6.1*. US Army Corps of Engineers, Institute for Water Resources, Hydrologic Engineering Center. September 2021.

# Energy Efficiency from Sustainable Materials

PhD. Student Eng. **Elena SURDU[1,*],** PhD. Student Eng. **Dana-Claudia FARCAȘ-FLAMAROPOL[1]**

[1] Politehnica University of Bucharest; elena.surdu@yahoo.com; claudia.flamaropol@gmail.com

* elena.surdu@yahoo.com

***Abstract:*** *The environmental impact in the life cycle chain is significantly greater than that which occurs exclusively at the waste management stage. Recycling waste can help reduce greenhouse gas emissions and other emissions. Regarding the impact on the environment, sustainable constructions are those that meet certain criteria: the design, the management of the construction process and the performance materials used. From this perspective, the use of renewable energy resources and associated technologies in the actual construction, operation and subsequent management of the objectives and in the maintenance methods in order to reduce greenhouse emissions is also significant.*

***Keywords:*** *Sustainable material, recycling, bricks*

## 1. Introduction

Inadequate waste management contributes to climate change and air pollution and directly affects many ecosystems and species. Waste recovery can thus contribute to the reduction of greenhouse gas emissions [1].
Recycling can contribute even more to reducing greenhouse gas emissions and other emissions. When recycled materials replace new materials, the need to extract or produce new materials decreases.
Waste also has an indirect impact on the environment. Anything that is not recycled or recovered from waste represents a loss of raw materials and other production factors used within the chain, respectively in the stages of production, transport and consumption of the product. The impacts on the environment in the life cycle chain are significantly higher than those that occur exclusively in the waste management stage [1].
In terms of environmental impact, sustainable constructions are those that meet certain criteria, from the design and management of the construction process to the performance materials used at all stages. Also, from this perspective, the use of renewable energy resources and associated technologies in the actual construction, operation and subsequent management of the objectives and in the maintenance methods in order to reduce greenhouse gas emissions is of significant importance [3].
From an economic point of view, the sustainability of constructions means moving from the old, well-known model of the linear economy to a new, circular model, which involves renewable energy, recycling of materials and produced waste, according to figure 1.

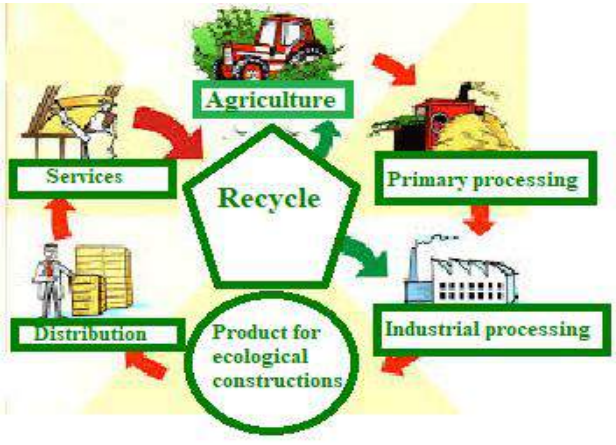


**Fig. 1.** Life cycle of a sustainable construction product [5]

The climate is changing and so are the construction requirements of future buildings, which must provide the necessary comfort for the occupants with a minimum of energy and environmental impact.

## 2. Sustainable material in construction

Materials used in construction represent one of the best methods of implementing sustainability. The progress of manufacturing technology allows the emergence of new generations of materials with properties at least identical to those of traditional materials. Also, the return to nature allowed finding solutions that, although used since ancient times, were overlooked for a long time [2].
These new construction materials are sustainable and ensure the protection of the environment as well as the reduction of the carbon footprint of the objectives of which they are part.
There are increasing efforts globally to develop new technologies, materials and non-conventional energy sources to reduce energy consumption and CO2 emissions associated with the buildings sector. Considering the impact that buildings have on energy consumption and on the environment, ceramic construction materials should be part of any ecological and responsible construction strategy. In order to preserve heat in natural buildings, good insulation is important, clay being optimal for storing heat. From the perspective of growing environmental concerns, the use of waste to develop bricks that exhibit appropriate characteristics attributed to the composition of the material are increasing [4].
The durability of the building depends on all the building materials used, without exception, but the wall material should be chosen with the greatest care, because even with an ideal place for construction, the poor choice of this component will make the building decay quite quickly. The material for the manufacture of walls can greatly influence the cost of the entire project, in addition, it can depend on some basic characteristics - for example, the thermal conductivity of the building.
Clay is a natural, sustainable and simple material, but with multiple properties (figure 2). It has been used since ancient times for pottery, writing pads, art objects, musical objects and especially, construction works.
Prehistoric people were the first to discover the useful properties of clay. Some of the earliest ceramic shards were found in Honshu, Japan and are dated to around 14,000 BC.
Clay as the defining ingredient in the composition of clay is one of the oldest building materials on earth, among other ancient natural geological materials such as stone and organic materials such as wood [3,4].
Between one-half and two-thirds of the world's population, in both traditional societies and developed countries, still live or work in buildings made with clay, often baked into brick or ceramic blocks, as an essential part of its load-bearing structure.
A primary ingredient in many natural building techniques, clay is used to create adobe structures.
Clay is an abundantly available natural material, it is very versatile, having been used for thousands of years in various industries. Recently, clay-based construction materials are beginning to capture more and more public attention, being considered a solution to reduce the impact that buildings have on the environment.

**Fig. 2.** Basic raw material for bricks [4]

Clay-based building materials are non-toxic, have a very low carbon footprint, contribute significantly to the regulation of humidity and indoor air quality, are resistant to fire and pests,

passively contribute to maintaining a constant temperature due to their high thermal mass and are also a good sound insulator.

### 3. Features for the use of natural materials in construction

Natural materials, either mineral (inorganic) or organic (of vegetable or animal origin), have particularly important common characteristics that make them clearly superior from an ecological point of view and the durability of synthetic materials used for insulation. Thus, natural materials, coming from and forming in the natural environment, are particularly resistant to the action of solar radiation and especially UVA and UVB components, which produce rapid degradation of any synthetic material (PVC, polystyrene, polyurethane, agglomeration resins, compounds of limes and synthetic paints, etc.). Also, natural materials have better durability and behaviour under the action of cyclical climatic factors, temperature, humidity, gelity, or the actions resulting from earthquake, fire, climatic accidents. So, it is necessary to understand that traditional techniques and local materials have proven their durability over time and are much healthier. Synthetic materials, foreign to the specific and polluting, do not represent a sustainable solution but, rather, can be the source of long-term problems.
Sun-dried unburnt brick, clay blocks mixed with straw, wool, cobs, walnut shells are sustainable materials that also have good energy efficiency.
The materials used in the production of bricks [3,4]:

❖ **sheep wool fibres** are used as a thermal and sound insulator both for wooden constructions and for brick or stone houses.
The qualities of sheep wool fibre insulation:

- ecological and healthy heat and sound insulating material, obtained from natural, renewable raw materials; accessible;
- resistant to mold and does not rot;
- the ability to absorb and release moisture from the surrounding air. Wool is a hygroscopic material, which means it can absorb up to 30% – 40% of its own weight in moisture, retaining its properties. Wool fibres naturally try to keep in balance with the changing humidity of the atmosphere. When the outside temperature drops and the air humidity increases, then wool takes in the extra moisture and releases heat in the process. Because of this, wool is said to "breathe" and act as a moisture and heat regulator.
- natural filter - naturally absorbs various air pollutants: volatile organic compounds, nitrogen dioxide and sulphur dioxide. Wool fibres absorb and irreversibly fuse with formaldehyde and other harmful substances.

❖ **straws** are based on the same substance as wood: cellulose. Due to the fact that the straws are hollow inside, the degree of thermal insulation is better than in the case of wood. By compressing the straw in the mixture it becomes resistant to compression, which means that it is suitable for the construction of solid walls. The earth and lime plaster allows the walls to "breathe", regulates humidity and provides a pleasant and healthy living environment. Straw constructions are very energy efficient due to their heat-insulating qualities.

❖ **hemp -** is a textile plant with many industrial uses. One of the applications for which the fibre of this plant with great regenerative power can be used is the creation of a material with the physical properties of concrete, but with a much reduced weight. The "bricks" made on the basis of hemp fibres are easy to transport, solid, insulate thermally and sound very well and have excellent fire resistance. In addition, hemp fibres continue to absorb carbon dioxide to a large extent.

❖ **bamboo wood -** being a plant with an amazing capacity for growth and regeneration (some species even grow up to 1 m in just 24 hours), bamboo is actually a herbaceous plant and not a tree, with an amazing spread over almost every continent, outside of Europe and the polar lands. Bamboo is a strong, resilient wood with considerable durability over time, especially if properly treated against pests and rot.

❖ **cork wood -** is an excellent soundproofing material, resistant to mechanical shocks and even thermal insulation. Cork resists fire well and even if it burns it does not emit toxic gases. In addition, it is a waterproof material and does not rot.

❖ **walnut shell -** is a granular material obtained from walnuts, it is hygroscopic, with little fermentation, which prevents the appearance of bacterial flora. This material is resistant even in humid conditions.

❖ **corn cobs** - they have high resistance and insulate well.

Brick is the most used material for building masonry. This has been used since ancient times when it was produced by hand.

The brick is usually produced industrially and is called pressed brick, but the brick can also be produced manually and is called hand brick [5].

With the advent of the industrial era, the production of burnt brick began to be technological, but its manual production did not stop.

## 4. Brick obtained industrially

**The technological process** (figure 3) by which the brick is obtained consists of the operations described below [6].

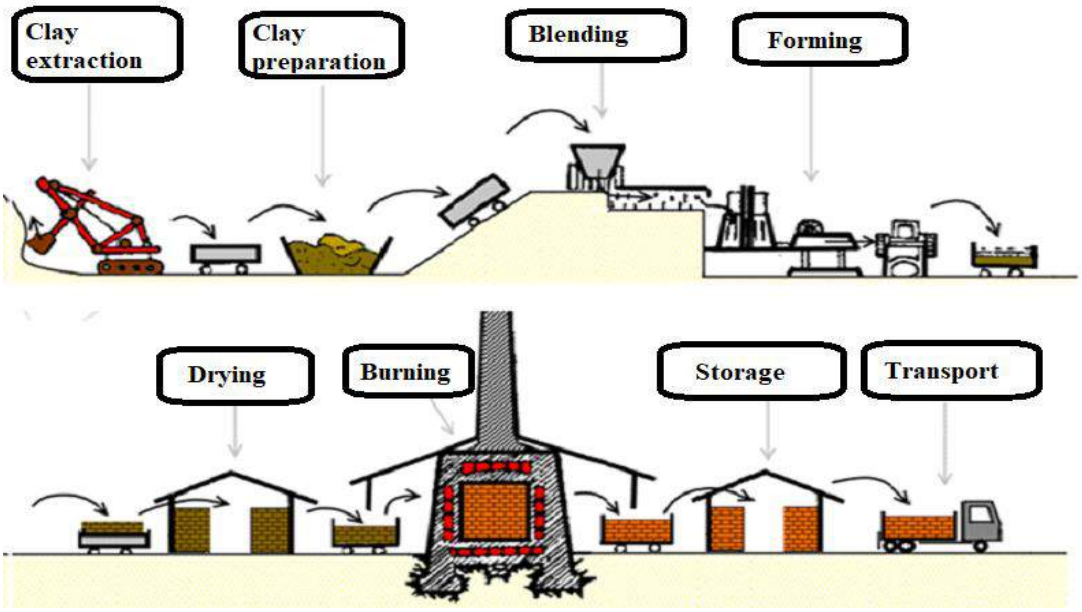


**Fig. 3.** Phases of the technological process of producing clay bricks [7]

The clay is extracted from the ground with the help of mechanical machines (figure 4) (excavators, grapples, etc.) and is transported to the brick factory. Sandy clay (clay) is used for the manufacture of bricks, it can contain lime in the form of dust up to 5%. The presence of lime granules in the composition of the clay is strictly prohibited. These granules are later extinguished, and this phenomenon leads, over time, to the deterioration of the bricks placed in the work.

**Fig. 4.** Clay extraction [9]

After the clay is mixed well with the help of mixers (figure 5), the paste is prepared. For this, sand and water are added in well-established quantities, according to the recipe. The paste obtained in this way is mixed with the help of a rolling mill with waves.

**Fig. 5.** Mixer for obtaining clay paste [10]

The shaping of the brick is done either with the help of patterns, or it is done mechanically, with the help of special presses (figure 6) and dies.

**Fig. 6.** Press for the production of ecological bricks [11]

After getting the shape, the bricks are taken to the dryers (figure 7). These dryers can be in the form of covered hoppers or in the form of special halls that have special rooms for drying bricks.

**Fig. 7.** Drying of bricks in special halls [12]

This last major step in the technological process of obtaining the brick is particularly important. Burning is done in tunnel furnaces (figure 8) or in special industrial furnaces, such as the circular furnace.

**Fig. 8.** Tunnel kiln for brick firing [8]

The process of burning bricks is carried out at temperatures between 900 and 1000°C.

## 5. Brick obtained by hand

The hand-made brick has not ceased to exist even today. Brick is produced from clayey, sandy soil called loam. This raw material is a mixture of clay and sand that also contains other materials, depending on the quality of the soil of the extraction area. The lower the percentage of materials, other than sand and clay, the better the quality of the brick [6, 14].
The clay used in the production of bricks (figure 9) may also contain a small amount of lime stone (limestone), but at most 5% and only in the form of dust. If there is limestone in the form of pebbles, it must be crushed.

**Fig. 9.** Clay used in the production of bricks [12]

If the pebbles are not crushed, they burn together with the clay and turn into quicklime. During masonry, these (slaked lime pebbles) absorb water from the mortar and turn into slaked lime, weakening the resistance of the brick, until it breaks.
**The technological process** of making the brick is [13]:
**a. Choosing and preparing clay**
After the soil is chosen, according to what was said before, it is taken out and deposited in a hole dug in the ground with a depth of approximately 30 cm. The surface of the pit is chosen depending on the amount of clay we want to process.
Once the soil is placed in the pit, mix with water and, if necessary, add sand and knead well.
**b. Placing the bricks in patterns**
The material thus obtained (clay) is added in patterns usually made of wood and lined with sheet metal or completely sheet metal. These patterns can have one or two meshes (figure 10), so one or two bricks can be made at once with a single pattern.

**Fig. 10.** Pattern for bricks and their formation [12]

So that the clay does not stick to the pattern, the walls of the pattern are sprinkled with water or dry sand is added.

**c. Drying of bricks**

After they have been removed from the patterns, the bricks are placed on a clean and level ground. They are positioned horizontally for better drying (figure 11). After drying on one side, the bricks are turned over for uniform drying.

**Fig. 11.** Drying of bricks [12]

After a drying that allows maneuverability and weight support, the bricks are stacked in the shelter for complete drying for up to 3-5 weeks. These being placed with spaces between them to allow air currents to circulate.

**d. Burning of handmade bricks**

After the complete drying period (3-5 weeks), the handmade brick is placed in the field oven (figure 12). Here, the bricks are stacked with spaces between them and cubes for fireplaces. Depending on the quantity of bricks, the kiln can have different sizes, reaching up to 40,000 bricks.

**Fig. 12.** Field furnace for burning bricks [8]

The brick oven can be burned with different fuels, such as: straw, cobs, sunflower stalks, soft wood, coal, gas.
During the burning process, the water in the brick structure is removed, producing pores (small voids). Once the water is removed, the volume of the brick is reduced. For this reason, the production of raw bricks must be done with slightly larger dimensions compared to the finished process (burnt brick). Burnt brick is 10% smaller than a raw brick [15].

## 7. Conclusions

Protecting the environment has become a highly discussed issue both nationally and internationally. The more we disrupt the climate, the greater the risk of dangerous changes, and the more difficult and costly it will be to limit future changes and adapt to the inevitable impacts.
Sustainable constructions can completely change the classic way of thinking about projects in the field. Sustainability is increasingly becoming a mandatory course of action as the negative impact of climate change increases at an ever-increasing pace.
The benefits of sustainable construction could pave the way to a cleaner future. Big construction companies aren't the only ones who could change their practices to benefit the environment. Ordinary people working on their personal projects can also focus on using sustainable building methods.
Thus, bricks made from sustainable materials can be a viable alternative that satisfies domestic comfort and environmental protection. They can be made of: clay, wool, wheat straw, corn cobs, walnut shells, hemp, bamboo wood, cork wood, etc.

### References

[1] Rusu, Tiberiu, and Mircea Bejan. *Waste – Source of income / Deşeul – sursă de venit*. Cluj-Napoca, Mediamira Publishing House, 2006.
[2] Hopu, V. *The Bricklayer's Handbook* / *Manualul zidarului*. Bucharest, M.C.I.M.C. Publishing House, 1972.
[3] The Romanian Order of Architects (Ordinul Arhitecților din România). "Architectural guide for fitting into the local specifics of the rural environment. Bran area" / "Ghid de arhitectură pentru încadrarea în specificul local din mediul rural. Zona Bran". September, 2017. Accessed February 14, 2023. https://www.patrimoniu-brasov.ro/admin/upload/homepage_informations/7/ghid_de_arhitectura_zona_bran_compressed.pdf.
[4] NIDUS Home. "The impact of buildings on the environment" / "Impactul clădirilor asupra mediului". April 8, 2020. Accessed February 6, 2023. https://www.nidushome.com/post/impactul-cladirilor-auspra-mediului.
[5] Georgescu, Claudiu. "Sustainable construction products for the energy efficiency of buildings" / "Produse de construcții sustenabile pentru eficientizarea energetică a clădirilor". Accessed February 7, 2023. http://www.euroconferinte.ro/prezentari/Tema1-13.pdf.
[6] ***. "Manufacturing clay bricks with their own hands - Line of equipment, brick manufacturing technology" / "Fabricarea de cărămizi din lut cu mâinile lor - Linie de echipamente, caramidă tehnologie de fabricație". Accessed February 6, 2023. https://ro.tutkrabov.net/articles/fabricarea-de-caramizi-din-lut-cu-mainile-lor.html.
[7] Rombadconstruct.ro. "Clay brick manufacturing" / "Fabricarea caramizilor din argila". April 10, 2020. Accessed February 7, 2023. https://www.rombadconstruct.ro/fabricarea-caramizilor-din-argila.html.
[8] ***. "The operating principles of a brick bake tunnel kiln" / "Principiile de funcționare a unui cuptor de tunel pentru coacerea cărămizilor". Accessed February 7, 2023. https://materiale.pvgazeta.info/utilizator-212/principiile-de-functionare-a-unui-cuptor-de-tunel.html.
[9] M. Equipment. "Soils, excavated rock and sand – how can they be managed on site?" / "Soluri, roci excavate și nisip – cum pot fi gestionate pe șantier?". July 27, 2021. Accessed February 8, 2023. https://www.mequipment.ro/soluri-roci-excavate-si-nisip-cum-pot-fi-gestionate-pe-santier/.
[10] Interceram. "Mixer Shimpo NVA 04S, with vacuum pump" / "Malaxor Shimpo NVA 04S, cu pompa vid". Accessed February 7, 2023. https://webshop.interceram.ro/malaxor-shimpo-nva-04s-cu-pompa-vid.html.
[11] ***. "LEGO-type ecological brick press" / "Presa, caramida ecologica de tip LEGO". April 9, 2016. Accessed February 8, 2023. https://www.bizcaf.ro/presa-caramida-ecologica-de-tip-lego_bizcafAd_1387063.dhtml.

[12] DecorexPro. “Features and production technology of raw bricks” / “Caracteristici și tehnologie de producție a cărămizilor brute”. Accessed February 10, 2023. https://ro-n.decorexpro.com/kirpich/vidy/syrcovoj/.
[13] ***. “What is clay?” / “Ce este argila?”. Accessed February 9, 2023. https://casasidesign.ro/ce-este-argila.html.
[14] Craven, Jackie. “All about Adobe - Sustainable and Energy Efficient” / “Totul despre Adobe - Sustainable and Energy Efficient”. Accessed February 9, 2023. https://ro.eferrit.com/totul-despre-adobe-sustainable-and-energy-efficient/ .
[15] Techirdalian, Claudia. “Eco-friendly materials (Part 1)” / “Materiale eco-friendly (Partea 1)”. *Casa Magazin*. April 27, 2021. Accessed February 8, 2023. https://www.casamagazin.ro/stiri/materiale-eco-friendly-partea-1--511.html.

# Laboratory Equipment for "Hot Air Generator with Forced Draft Fan Based on the TLUD Principle"

Dipl. Eng. **Ioan PAVEL**[1,*], PhD. Eng. **Gabriela MATACHE**[1], Dipl. Eng. **Valentin BARBU**[1], Res. Assist. **Ana-Maria POPESCU**[1], Tech. **Kati PAVEL**[1]

[1] National Institute of Research & Development for Optoelectronics / INOE 2000 – Subsidiary Hydraulics and Pneumatics Research Institute / IHP, Bucharest, Romania

* pavel.ihp@fluidas.ro

***Abstract:*** *The issues related to the optimization of energy consumption in heating equipment have emerged in recent years, when research has been intensified for a more ecological, more modern and more efficient combustion achievable, for example, by addressing new combustion solutions or technologies, such as the use of the Top-Lit Updraft (TLUD) principle for heating equipment. The article presents a laboratory equipment piece for a "Hot air generator with forced draft fan based on the TLUD principle" that operates in the loop to maintain the temperature at 180°C at the chimney outlet, which is recommended for boilers with biomass gasification, to avoid tar deposition. Also, the equipment can control the temperature of the hot air produced, by controlling the gasification air flow rate and adjusting the working power. The combustion quality can be optimized by controlling the $CO_2$ emissions or other unburned gases and suspended particulate matter (SPM) at the chimney outlet.*

***Keywords:*** *Gasification, Top-Lit Updraft (TLUD), biomass, biochar, greenhouse gases, stoichiometric combustion*

## 1. Introduction

Energy consumption in developing countries for cooking and heating is mainly based on biomass fuels. An estimated 40% of the global population relies on burning solid biomass fuel to meet some or all of their household energy needs [1] which is very inefficient and produces harmful emissions through incomplete combustion.
A growing number of publications suggest that incomplete combustion by-products and noxious emissions from traditional biomass burning have contributed significantly to climate change [2, 3].
Combustion technologies are fairly well-defined for equipment that burns biomass cleaner and more efficiently [4]. However, it has been noted that not all solutions are supported by research and market demands [5]. For this reason, it is important that equipment is tested before being released to the market to ensure that new models offer significant improvements given the cooking or residential heating practices prevalent in a particular area with a particular type of biomass [5].
The reduced fuel consumption of modernized combustion equipment is linked to increased efficiency, therefore, assessing their thermal performance is essential for the development of more efficient technologies [6,7]. The energy performance of various combustion equipment has been achieved by some researchers by using biomass fuel as a renewable energy resource, $CO_2$ neutral and a viable alternative to fossil fuel [8-11].
The practice of using renewable biomass resources to generate bioenergy has increased significantly recently [12,13]. Among the various technological options, biomass gasification is a relatively simple solution in process/reactor design and implementation [14]. After gasification, two components result: synthesis gas and biochar. Biochar is known for its carbon-rich nature that provides valuable benefits to the environment [15].
Top-lit updraft (TLUD) gasification has the potential to simultaneously produce biochar and syngas from biomass. It was found that some models of TLUD gasifiers have relatively high yields in the production of biochar and synthesis gas [16,17].
Gasification is a process by which solid fossil fuels are converted into a synthetic fuel gas called syngas (mainly a mixture of carbon monoxide and hydrogen); is a thermochemical degradation process that takes place at high temperatures (800-1000°C) in an environment where the amount of oxygen is lower than that required for complete combustion. In order for the biomass gasification

combustion process to be complete, it is necessary that the air required for complete combustion and the resulting gas (syngas) be mixed in a certain ratio under appropriate conditions of turbulence and temperature. If the combustion is incomplete, either due to a lack of oxygen, or if the excess oxygen cools the vapors below the optimal point at which they will burn, unwanted pollutant emissions and energy waste result [18].
Forced draft gas cookstoves have been shown in laboratory studies [19-21] to reduce CO and PM emissions by 90% compared to free combustion (as one can see in Figure 1).

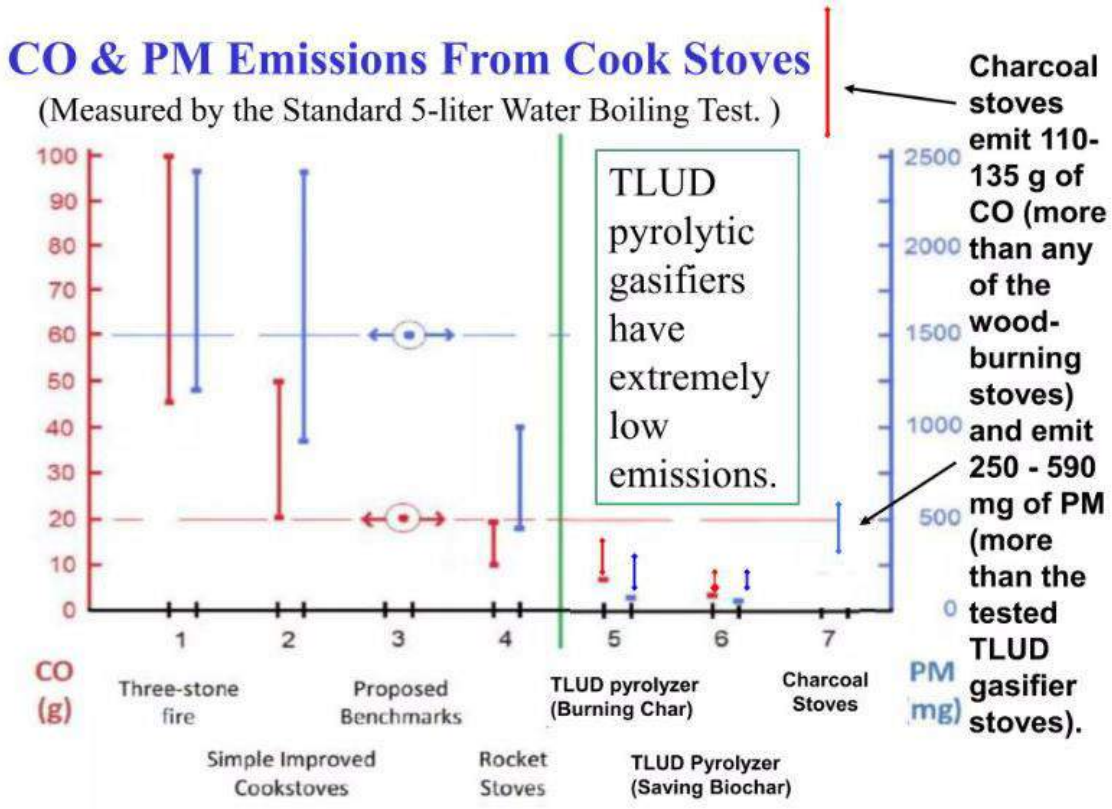


**Fig. 1.** Comparison of CO and PM emissions from various combustion technologies and systems [22]

Materials considered waste (bark, residues from forest wood cutting, residues from secondary agricultural production, etc.) can be used effectively to produce thermal energy and store carbon in biochar. Virtually any chopped and dried or densified wood material can be fuel for TLUD installations.

## 2. Presentation of the "TLUD hot air generator" laboratory equipment

### 2.1 General characteristics of the TLUD principle

The TLUD process implies a fixed layer of biomass (the pyrolytic front advances in the biomass layer) and as a result the gasifier works in a batch mode with recharging. The gasification process is done with a reduced intensity with specific hourly consumption of 80 – 150 kg.bm/m²h; this fact results in reduced specific reactor powers of 250–350 kW/m². Due to the slow gasification process, the surface velocity of the produced gas has very low rates, namely below 0.06 m/s, which ensures a reduction in the rate of entrainment of free ash at concentrations below PM 2.5 at the burner outlet, to a maximum of 5 mg/MJbm. This value is at least five times lower than the current norms imposed for solid fuel thermal generators.
Limiting the air speed in the reactor to ≤ 0.06 m/s has to be observed so that any entrained particulates do not advance through the chimney towards the atmosphere. In our case, the reactor has a diameter of Ø100 and the primary air flow rate is 25 l/min.

$$D_{react} = \phi 100 \tag{1}$$

$$Q_{primary\ air} = 25 l/min \tag{2}$$

It results that the air speed in the reactor is:

$$V = \frac{Q}{A} = \frac{25 l/min}{\frac{0.1^2 \cdot 3.14}{4} m^2} = \frac{0.025/60\ \cancel{m^3}/s}{0.00785\ \cancel{m^2}} = 0.053\, m/s < 0.06\, m/s \tag{3}$$

The research endeavours at the level of the INOE 2000-IHP Institute to study this combustion process have taken the shape of a laboratory equipment. A series of tests will be carried out on it that could transform the classic cooking equipment into a forced draft hot air generator, with pollutant emissions below the norms proposed by 2030, with a conversion efficiency of up to 85%, which also produces – in an amount of about 10...20% of the initial amount of biomass - residual charcoal, not converted into gas, known as biochar.

### 2.2 Presentation of the laboratory equipment

The laboratory equipment (Figure 2) consists of frame <1>, electronic scale <2>, gas generator <3>, combustion chamber <4>, heat exchanger <5>, draft regulator <6>, forced draft subassembly <7>, chimney temperature sensor <8>, grip for noxious emissions sensor <9>, grip for particulate matter sensor <10>, hot air temperature sensor <11>, combustion air manual control throttle <12>, secondary air servo valve <13>, secondary air flow meter <14>, primary air flow meter <15>, primary air throttle <16>, primary air servo valve <17>, pressure sensor <18>, laptop <19>, acquisition board <20>, temperature controller <21> and PLC <22>.
The equipment works in a loop to maintain a temperature of 180°C at the chimney outlet, which is recommended for boilers with biomass gasification, to avoid the deposition of tar. The equipment can also control the temperature of the hot air produced, by controlling the gasification air flow rate and adjusting the working power. The combustion quality can be optimized by controlling the $CO_2$ emissions or other unburned gases and suspended particulate matter (SPM) at the chimney outlet.

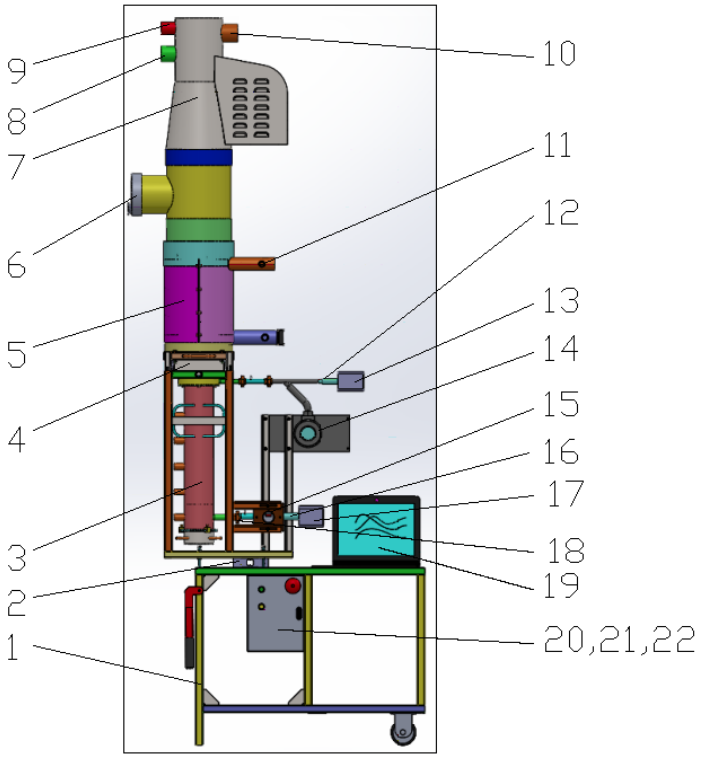


**Fig. 2.** "TLUD hot air generator" laboratory equipment – 3-D design

### 2.3 The principle of operation

As one can notice in Figure 3, the equipment is provided with a computer (2) and a data acquisition program developed in LabView, with a friendly graphic interface, which displays and records all acquired parameters and their graphs in real time, a controller (3) for monitoring the temperature on the chimney and a PLC for controlling the pneumatic servo valves (11). The temperature sensors (5) monitor the temperature in various points of the reactor (6) during the gasification and combustion process.
To initiate combustion, the heat exchanger (13) is disconnected from the reactor (6). After ignition, the forced draft fan (15) is switched on again; in this way a depression is created and the required amounts of gasification and combustion air are provided. This air flow can be adjusted by varying the fan speed and by means of the draft regulator (14). These flow rates are monitored by using the flow transducers (9), and the depression value at the gas generator inlet is monitored by using the transducer (8). Right after ignition, the gasification and combustion air flow rates will have maximum values so that the temperature on the chimney reaches the value of 180°C read by the sensor (18) as quickly as possible. When the value is reached, the sensor sends a control signal, through the controller and the PLC, for the proportional closing of the servo valves (11), thereby reducing the air flow rate. The hot air temperature at the outlet of the exchanger is monitored by using the temperature sensor (12). The quality of the combustion is monitored by means of a gas analyzer (17) and a SPM analyzer (16) at the chimney outlet. Biomass consumption is monitored in real time by using the electronic scale (7).
As the laboratory equipment is fitted out in a complex manner, it allows the monitoring of the TLUD combustion process and its quality, and thus the optimal operating parameters and control loops for this type of equipment can be determined.
The main purpose of this paperwork is to present a hot air generator solution based on the TLUD principle, with forced draft fan, and a solution for optimizing combustion by maintaining the chimney temperature at 180°C to avoid the formation and deposition of tar, by setting the maximum speed of the main (gasification) air flow rate so as to avoid PM emissions in the atmosphere and by dosing the secondary (combustion) air flow rate so as to reduce the noxious emissions.

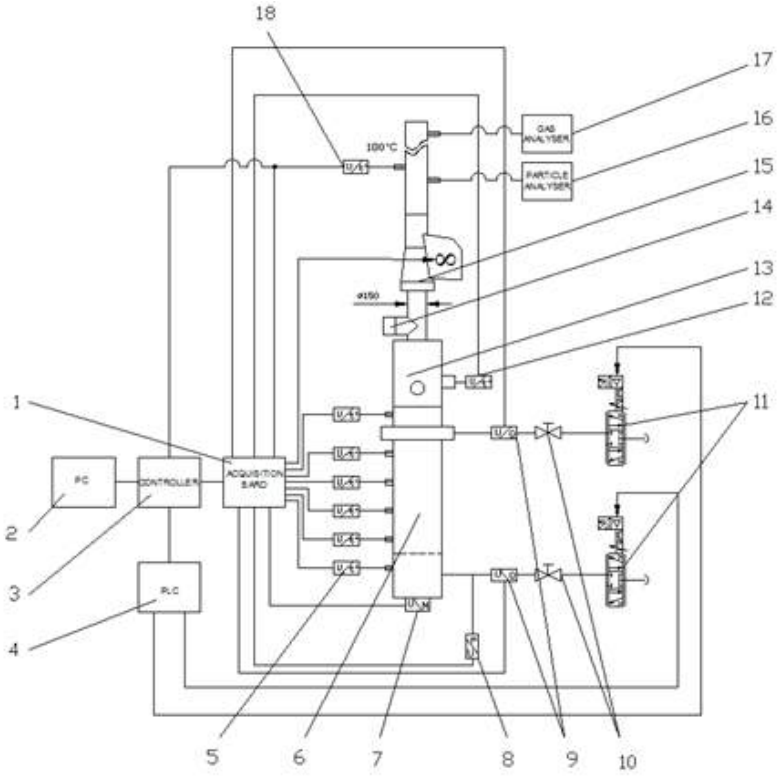


**Fig. 3.** Operating diagram of the laboratory equipment "hot air generator based on the TLUD principle"

The amount of hot air required is monitored by the temperature sensor (12), and through the acquisition board of the controller and the PLC (or the dedicated PC software) the primary and secondary air flow rates can also be adjusted in order to control the power of the gas generator and implicitly the amount of hot air required.

## 3. Conclusions

The most important benefit that the gas generator working on the TLUD principle offers is that it provides clean energy compared to any of the other combustion methods; it offers environmental protection solutions by storing carbon in biochar and by PM and $CO_2$ emissions at the chimney below the values imposed by European legislation, thus contributing to the reduction of greenhouse gas emissions, to the effective protection of the environment and to ensuring a sustainable energy development.
By continuing research with the TLUD hot air generator laboratory equipment, it is possible to deepen the study of the combustion quality and control at the TLUD equipment, which can move these devices from the category of food preparation equipment to the category of automated heating equipment similar to gasification boilers, and this can be a solution for replacing heating equipment operating on outdated, less cost-effective and less environmentally friendly combustion systems.

**Acknowledgments**

This work was carried out through the Core Program within the National Research Development and Innovation Plan 2022–2027, carried out with the support of MCID, project no. PN 23 05. This research was also supported by a project funded by the Romanian Ministry of Research, Innovation and Digitalization through Programme 1—Development of the national research & development system, Sub-programme 1.2—Institutional performance—Projects financing the R&D&I excellence, Financial Agreement no. 18PFE/30.12.2021.

**References**

[1] Bonjour, S., H. Adair-Rohani, J. Wolf, N.G. Bruce, S. Mehta, A. Prüss-Ustün, M. Lahiff, E.A. Rehfuess, V. Mishra, and K.R. Smith. "Solid fuel use for household cooking: country and regional estimates for 1980–2010". *Environmental Health Perspectives* 121, no. 7 (July 2013): 784-790.
[2] Johnson, M., R. Edwards, A. Ghilardi, V. Berruta, D. Gillen, C.A. Frenk, and O. Masera. "Quantification of carbon savings from improved biomass cookstove projects." *Environmental Science & Technology* 43, no. 7 (2009): 2456-2462.
[3] Smith, K.R., R. Uma, V.V.N. Kishore, J. Zhang, V. Joshi, and M.A.K. Khalil. "Greenhouse implications of household stoves: An analysis for India." *Annual Review of Energy and the Environment* 25 (November 2000): 741-763.
[4] Masera, O., R. Edward, C. Armendáriz Arnez, V. Berrueta, M. Johnson, L. Rojas Bracho, H. Riojas-Rodríguez, and K.R. Smith. "Impact of Patsari improved cookstoves on indoor air quality in Michoacán, Mexico." *Energy for Sustainable Development* 11, no. 2 (June 2007): 45-56.
[5] Adkins, E., J. Chen, J. Winiecki, P. Koinei, and V. Modi. "Testing institutional biomass cookstoves in rural Kenyan schools for the Millennium Villages Project." *Energy for Sustainable Development* 14 (2010), 186-193.
[6] Berrueta, V.M., R.D. Edwards, and O.R. Masera. "Energy performance of wood-burning cookstoves in Michoacan, Mexico." *Renewable Energy* 33, no. 5 (May 2008): 859-870.
[7] Fang, Y., Q. Wang, X. Bai, W. Wang, and P.A. Copper. "Thermal and burning properties of wood flour-poly (vinyl chloride) composite." *Journal of Thermal Analysis and Calorimetry* 109 (September 2012): 1577-1585.
[8] Pandey, A.K., V.V. Tyagi, S.R. Park, and S.K. Tyagi. "Comparative experimental study of solar cookers using exergy analysis." *Journal of Thermal Analysis and Calorimetry* 109 (July 2012): 425-431.
[9] Tyagi, S.K., A.K. Pandey, S. Sahu, V. Bajala, and J.P.S. Rajput. "Experimental study and performance evaluation of various cook stove models based on energy and exergy analysis." *Journal of Thermal Analysis and Calorimetry* 111 (March 2013): 1791-1799.
[10] Tyagi, V.V., A.K. Pandey, S.C. Kaushik, and S.K. Tyagi. "Thermal performance evaluation of a solar air heater with and without thermal energy storage: an experimental study." *Journal of Thermal Analysis and Calorimetry* 107 (March 2012): 1345-1352.

[11] Magdziarz, A., and M. Wilk. "Thermal characteristics of the combustion process of biomass and sewage sludge." *Journal of Thermal Analysis and Calorimetry* 114 (November 2013): 519-529.
[12] Casler, M.D., R. Mitchell, J. Richardson, and R.S. Zalesny. "Biofuels, bioenergy, and bioproducts from sustainable agricultural and forest crops." *BioEnergy Research* 2 (August 2009): 77-78.
[13] McCord, J., V. Owens, T. Rials, and B. Stokes. "Summary report on the 2012 Sun Grant National Conference: Science for biomass feedstock production and utilization." *BioEnergy Research* 7 (July 2014): 765-768.
[14] Hasan, J., D.R. Keshwani, S.F. Carter, and T.H. Treasure. "Thermochemical conversion of biomass to power and fuels." Cheng, J. (Ed.). *Biomass to Renewable Energy Processes*. 1st edition. Boca Raton, CRC Press, 2009, 437-489.
[15] Lorenz, K., and R. Lal. "Biochar application to soil for climate change mitigation by soil organic carbon sequestration." *Journal of Plant Nutrition and Soil Science* 177, no. 5 (October 2014): 651-670.
[16] Birzer, C., P. Medwell, J. Wilkey, T. West, M. Higgins, G. MacFarlane, and M. Read. "An analysis of combustion from a top-lit up-draft (TLUD) cookstove." *Journal of Humanitarian Engineering* 2, no. 1 (August 2013): 1-7.
[17] Tryner, J., B.D. Willson, and A.J. Marchese. "The effects of fuel type and stove design on emissions and efficiency of natural-draft semi-gasifier biomass cookstoves." *Energy for Sustainable Development* 23 (December 2014): 99-109.
[18] Pavel, I., R.I. Rădoi, G. Matache, A.-M.C. Popescu, and K. Pavel. "Experimental research to increase the combustion efficiency in the Top-Lit Updraft principle based gasifier." *Energies* 16, no. 4 (February 2023): 1912.
[19] Jetter, J., and P. Kariher. "Solid-fuel household cook stoves: Characterization of performance and emissions." *Biomass Bioenergy* 33, no. 2 (February 2009): 294-305.
[20] Jetter, J., Y. Zhao, K.R. Smith, B. Khan, T. Yelverton, P. DeCarlo, and M.D. Hays. "Pollutant emissions and energy efficiency under controlled conditions for household biomass cookstoves and implications for metrics useful in setting international test standards." *Environmental Science & Technology* 46, no. 19 (2012): 10827-10834.
[21] MacCarty, N., D. Still, and D. Ogle. "Fuel use and emissions performance of fifty cooking stoves in the laboratory and related benchmarks of performance." *Energy for Sustainable Development* 14, no. 3 (September 2010): 161-171.
[22] Anderson, P.S. "The Future of Micro-gasifier Stoves: Meeting the Goals of the Global Alliance for Clean Cookstoves." Paper presented at the 2012 ETHOS conference, Seattle-Kirkland, Washington, USA, January 28, 2012. *Slideshare*. February 6, 2012. Accessed February 8, 2023. https://pt.slideshare.net/bitmaxim/ethos-keynote-2012.

# Sludge Dewatering Installations

PhD. Student Eng. **Dana-Claudia FARCAȘ-FLAMAROPOL[1,*], ** PhD. Student Eng. **Elena SURDU[1],** PhD. Student **Ramona MARE[1]**

[1] Politehnica University of Bucharest; claudia.flamaropol@gmail.com; elena.surdu@yahoo.com; ramona_mare@yahoo.com

* claudia.flamaropol@gmail.com

***Abstract:*** *In this article, we aimed to present the theoretical concepts, from the specialized literature, related to the dewatering of sludge resulting from the wastewater treatment process, focusing on the dewatering facilities used in our country and around the world. Emphasis is placed on mechanical dewatering, but also on other sludge dewatering procedures.*

***Keywords:*** *Wastewater sludge, dewatering, dewatering facilities*

## 1. Introduction

At the basis of all sludge treatment processes are two distinct technological processes, namely sludge stabilization through fermentation and sludge dewatering. Between these two main processes, various variants or combinations of procedures can occur, whose application is differentiated depending on local conditions, the amount and quality of sludge, the existence of lands for installing drying and storage facilities, or the intended use of the sludge, etc. Normally, at present, fresh sludge from urban wastewater treatment plants is preprocessed through anaerobic fermentation (to obtain biogas), followed by natural or artificial dewatering processes and finally its utilization in agriculture as fertilizer, but only if it complies bacteriologically. Dewatering is a physical (natural or mechanical) operation used to reduce the moisture content and volume of sludge. Its main objectives are [1]:

- Increase the dry substance content of the sludge by 3-40%;
- Reduce transportation costs due to volume reduction;
- Improve handling and transportation of sludge;
- Avoid odors;
- Increase calorific power by reducing humidity.

The main way to reduce the amount of sludge after treatment is to reduce the amount of water present in the sludge through thickening and dewatering. There is a limit to the amount of water that can be removed from the sludge by mechanical means and most dewatered sludge (for example, using belt press, filter press, centrifuge, etc.) have a dry substance content ranging from 15% to 40%. Any of the waste management alternatives also requires thermal drying of the waste [2,3].

## 2. Natural Dewatering

Drying beds for sludge ensure the dehydration of the sludge, allowing the liquid to drain both through gravity through a permeable medium on which the sludge is located and to evaporate in ambient conditions. Drying beds are uncomplicated in design and operation, as they simply involve spreading the sludge as a thin layer (up to 300 mm) on a porous bed of sand and gravel. The water is then allowed to drain through the bed and into a network of incorporated drainage pipes to allow for its collection (fig. 1). Further removal of water is ensured through evaporation from the surface of the sludge [2,3,4].

While most drying beds are uncovered, and therefore their performance is subject to local weather conditions, water evaporation rates can be increased by sheltering the layers in a glass structure (a greenhouse).

This modification is usually referred to as a solar drying bed and is used in warmer climates.

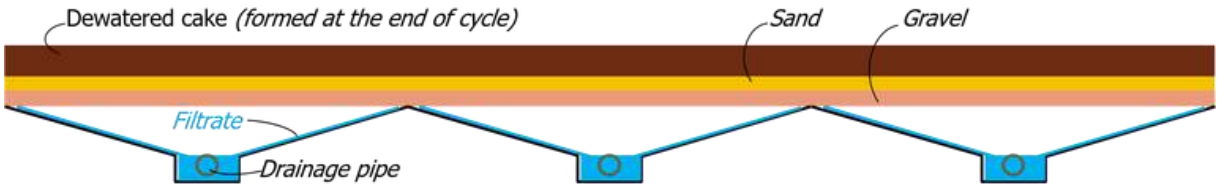


**Fig. 1.** Drying bed for sludge [4]

Sludge ponds, also known as lagoons, are located in natural depressions where the depth is greater than 2 meters, creating as much space for sludge as possible. Sludge is introduced into these ponds for fermentation, drying, or long-term storage. A lagoon contains a shallow, tight-bottomed reservoir to prevent the infiltration of sludge water into groundwater or other water bodies in the environment. The lagoon is filled with sludge and the solids are allowed to settle. During the drying/dehydration operational cycle, which is approximately a few months, water is lost through evaporation while the solids form a thick layer at the bottom of the lagoon, stabilized by anaerobic biological processes.

## 3. Mechanical Dehydration

According to the dehydration principle, there are three methods to do that [5]:

- Dehydration through vacuum filtering
- Dehydration through pressure filtering
- Dehydration through spinning

Artificial dehydration of sludge is performed through static procedures (vacuum filters, pressure filters) or dynamic procedures (centrifugation).

- The main advantages of artificial dehydration processes are [6, 7]:
- Short process duration
- Small area required for equipment

Lack of influence of inhibitors on dehydration processes.
The disadvantages include [6, 7]:

- Preconditioning of sludge
- No influence on pathogenic potential
- Limitation of incineration application due to increased mineral content of sludge, in case of conditioning with mineral salts
- Low fertilizing value of dehydrated sludge.

### 3.1. Press Filter

**The press filter** is a piece of equipment used for dewatering sludge from various wastewater treatment processes (e.g. industrial wastewater treatment plants, household wastewater treatment plants, etc.). Using this equipment, we can obtain a cake-like, highly-dried sludge with a high solid content.

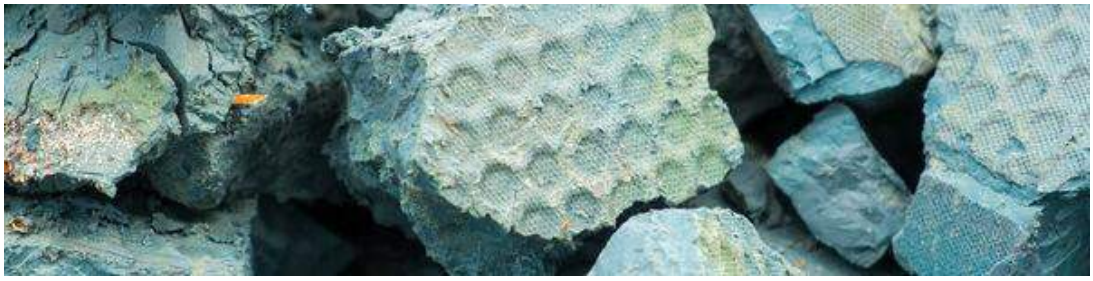

**Fig. 2.** The cake produced by the press filter, which has chunks of dehydrated sludge solids with an imprint of the filter cell membrane [8]

The pressure filter is the most efficient solid/liquid separation system and the most widely used filtering system in various industrial applications [8, 9]. According to [9], the pressure filter operates

by slowly filling the spaces between the plates with sludge before applying 7-20 bar pressures for 1-2 hours. Water is forced out of the sludge under the applied pressure, and the filtrate is returned to the influent of the treatment plant. Air is then washed through the system for 5-15 minutes to remove most of the residual water from the cake formed in the depressions. The filter cake can also be washed at this point to remove contaminants. The plates are then separated and the solid filter cake, 25-40 mm thick, is allowed to fall. The complete operating cycle of filling, filtering, emptying, and washing the press can take up to five hours.
Advantages [9]:

- High productivity: due to fine filtration under high pressure,
- High capacity: are designed to ensure maximum capacity for utilisers,
- Safe functioning: press filters are designed variable alternatives for user's safety,

### 3.2. Belt press filter

A belt filter press (BFP) ensures sludge dewatering by pressing the sludge to force water to pass through a permeable medium. The process produces a cake (the dehydrated product) with a dry solid (DS) content of 30% or more in the case of primary sludge. Modern belt presses are based on a combination of chemical conditioning, gravity drainage and mechanical pressure in a continuous feeding system for sludge dewatering. The sludge is squeezed between tensioned spiral belts and a series of decreasing diameter rolls (to increase pressure) to remove moisture and create a dehydrated sludge cake. A BFP combines sequential drainage and mechanical pressure to remove water. The equipment normally includes 2-3 recirculation belts (figure 3), with two belts combining at one point to compress the sludge and squeeze out the water. Conditioned sludge is first transported along a gravity drainage section of one of the porous belts, as in the case of a gravity belt thickener. It then undergoes pressure as it is passed between two recirculation belts, forming a deposition area at the entrance, which moves over a roll. This squeezing action of the two belts in this pressure area releases more water. Many belt filter press technologies contain a second pressure area that comprises a series of rolls through which the two belts with solid sludges are retained between them. The rolls in this high-pressure area apply the stretching of the belts, exerting both shearing and compressive forces on the sludge, which releases even more water.

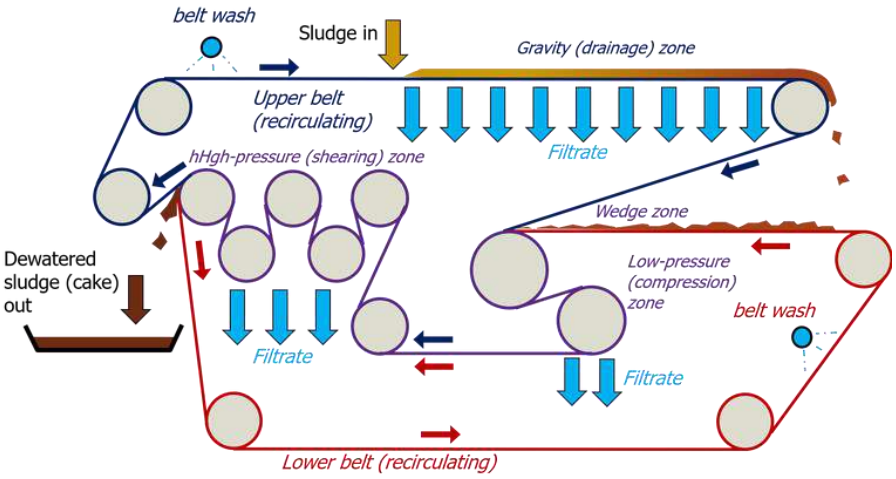


**Fig. 3.** Example of arranging the belts and rolls for a belt filter press, double belt system [3]

Advantages [10]:

- The personnel requirements are low, especially if the equipment is large enough to process solids in a single shift;
- Maintenance is relatively simple and is usually provided by the sewage treatment plant maintenance team;
- Belt replacement is the main reason for increasing maintenance costs;

- Belt presses can be started and stopped quickly compared to centrifuges, which require up to an hour to increase speed;
- The noise produced is lower compared to centrifuges.

Disadvantages [10]:

- Odors can be a problem, but can be controlled with good ventilation systems and chemicals such as potassium permanganate;
- Belt presses require more operator attention if the feed solids vary in concentration or organic matter;
- Waste water solids must be screened to minimize the risk of belt damage;
- Washing the belt at the end of each shift or more frequently can consume a lot of time and require large amounts of water.

### 3.3. Press filter with screw

A screw press (SP) (Figure 4) provides sludge dewatering by transporting it along the interior of a permeable cylinder. It relies on a slow-rotating Archimedes screw (~5 RPM) in a cylindrical screen (also referred to as a drum or basket). It is typically inclined by ~20° from horizontal to assist in draining the water into the basin. The screen typically has a nominal opening value under 0.5 mm and is based on mesh wire or occasionally perforated metal. Screens are less susceptible to clogging than the filtering media used for other thickening and dewatering processes. As a result, spray cleaning is applied only intermittently for approximately 2-4% of the operating time. As with all thickening and dewatering processes, the solids (or cake) content of the product depends on the quality of the feed sludge. The solids, cake content has been shown to be inversely proportional to the volatile solids (VS) in the feed sludge [1, 2, 11].

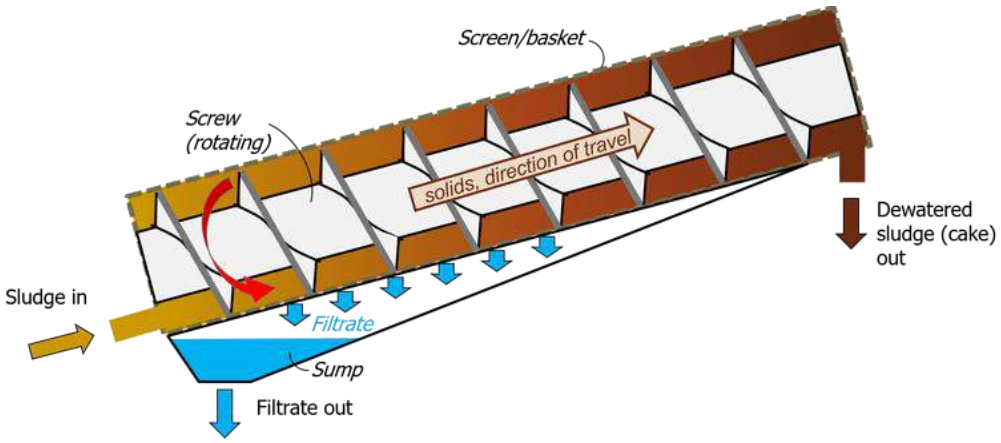


**Fig. 4.** Press with screw [11]

### 3.4. Rotary Press

A rotary press (RP) is a dewatering technology that removes water by passing sludge through a narrow, rotating, parallel-flow channel with porous walls. The rotary press provides dewatering using a cylindrical vessel that houses two circular screens that rotate slowly (< 2 rpm) and are positioned together. The sludge enters the channel formed between the two screens and follows a circular path around the channel at a low applied pressure (0.1-0.5 bar) (figure 5). The combination of the applied pressure, generated by creating a restriction at the outlet, and shear forces generated by the rotational action and moving solids encourage filtrate to pass through the two screens as the sludge moves around the channel [2,3,11].

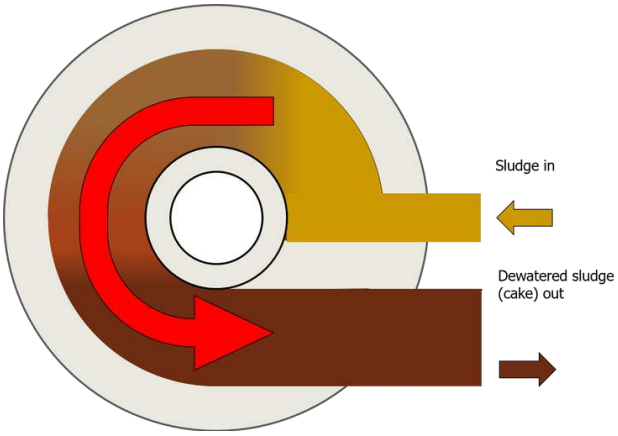


**Fig. 5.** Sludge flow through the rotary press [11]

### 3.5. Solid Bowl Centrifuge

According to [12], centrifugation is a phase separation process of particles with different specific weight (solid-liquid). Under the centrifugal force, the solid, heavy phase deposits on the interior walls of the rotating drum, where it is constantly scraped by the conical screw inside, which also directs the scraped material towards the conical end at the discharge opening. The liquid phase, separated by gravitational flow, is sent to the liquid discharge opening located opposite the solid material discharge opening. According to [2,3], compact concentrates with a higher solid material content: 22-25% DS are obtained through centrifugation. If the sludge has a high content of inorganic solid matter, the DS concentration can reach 33-35%. These types of equipment can be grouped into three categories, with specific application domains [2,3,11]:

- conical rotor centrifuges, which produce good dewatering and clear centrate, but are not suitable for fine solids;
- cylindrical rotor centrifuges, which generally produce clear centrate;
- cylindro-conical rotor centrifuges, which produce well-dewatered cakes and clear centrate.

The solid bowl centrifuge, according to [11], can be used to produce a relatively dry cake from separated solids and is flexible enough to handle a wide fluctuation in feed material and still achieve excellent clarification and dewatering performance. The centrifuge (figure 6) consists of a solid bowl, which rotates and contains the process. A screw conveyor, contained in the bowl, rotates at a slightly different speed from that of the bowl.

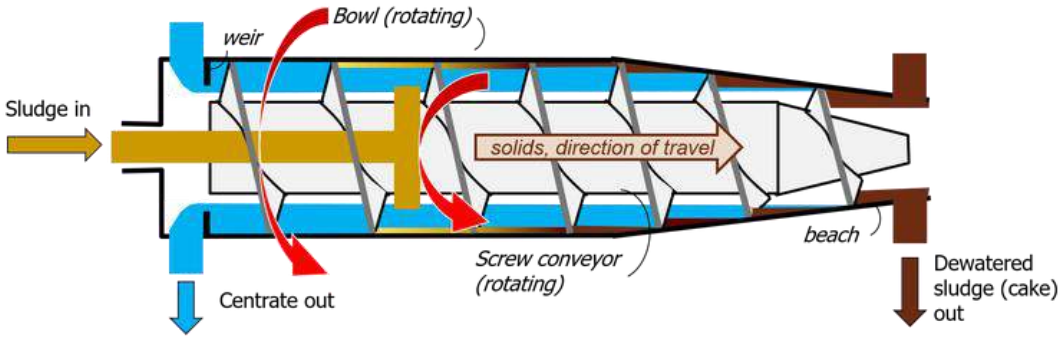


**Fig. 6.** Dehydration centrifuge with a strong bowl, countercurrent operation [11]

In practice, flocculated sludge is introduced into the centrifuge drum through an injection pipe. The drum has a high rotation speed (3500 rpm), the particles move towards its sides, in the clarification area. The particles are then pushed through an Archimedes screw towards the conical end of the drum, in the drying area, by the rotation of the sludge. The clarified liquid, called 'centrate', is discharged at the other end of the drum through an overflow. The decanter centrifuge will often produce better results than other dewatering equipment when secondary or biological sludge are present in the material to be processed. The main reason for this is that decanter centrifuges do

not use filtering media for separation and dewatering, which can often become blocked by biological sludge.
Advantages [13,14]:

- Centrifuges can provide lower overall operating and maintenance costs than conventional belt press filters;
- Centrifuges require a small operating space;
- Centrifuges are continuous operation equipment that can be incorporated into any technological process;
- Operators have low exposure to pathogens, aerosols, hydrogen sulfide, or other odors;
- Centrifuges are easy to clean;
- They increase the quality of the technology in the system they are incorporated into;
- Major maintenance components can be easily removed and replaced. Repairs are usually carried out by the manufacturer.

Disadvantages [13,14]:

- Centrifuges have high energy consumption and are quite noisy;
- Experience in using the equipment is necessary for optimizing performance;
- Special structural considerations must be taken into account;
- Replacement parts are expensive internal parts and are subject to abrasive wear;
- Start-up and shut-down can take an hour. The centrifuge is gradually brought up to maximum speed and slowed down for cleaning before shutdown.

### 3.6. Mechanical dehydration on vacuum filters

This is the most widely used process currently for artificial water drainage. The construction form of vacuum filters can be different (disc, hopper or drum), drum vacuum filters (figure 7) being the most commonly used for dewatering sludge from wastewater treatment.

**Fig. 7.** Vacuum – rotary drum filter [6]

According to [6], dehydrating sludge on vacuum filters has the advantages of continuous operation (unlike press filters) and high filtration capacity. There is also a flexible construction configuration (available discharge options, drum cells, construction materials, design - open or closed filter, airtight), which provides the possibility of adapting to process needs. Among the disadvantages, relatively rapid degradation of filter cloths, relatively high cake moisture (70-80%) and higher energy consumption than press filters can be mentioned.

## 4. Other Sludge Dewatering Processes

### 4.1. Electro-Dewatering

The Electro-Dewatering (EDW) technology removes water from sludge based on the principle of electro-osmosis.
According to source [15], electro-osmotic dewatering (EOD) is a technique that removes water by placing a colloidal material between two electrodes. This is based on the electrostatic effects of the double electric layer that forms at the water particle interface of the colloidal material. An EDW

device consists of a narrow horizontal channel through which the sludge is fed. A direct electric field is placed over the channel, with the anode at the top and the cathode and a filter cloth at the base. The cathode on which the filter cloth is placed is porous to allow water to pass through it [3,16]. The application of an electric field causes the water to be extracted from the sludge under the influence of the electro-osmotic force. No additional mechanical force is required: the water removal rate depends on the charge on the particle surface and the applied voltage. Through this method, a cake of up to 50% dry solids (DS) has been obtained, with a reduction in sludge volume of up to 75% at sludge loading rates of 75-150 kg DS/(m2.h) per m2 dewatering surface.

### 4.2. Liquid Sludge Treatment through Dewatering Technology

The dewatering technology mainly consists of a sludge treatment technique that, through progressive water removal, allows for their drying and therefore water removal. The process is carried out with "GTX Tube" structures made of composite materials: geogrids and geotextile-consolidated membranes, such as the filter system. The designed system minimizes the possibility of particles transported in the drainage water to leak out. The "GTX Tube" performs a simple and efficient technological dehydration, meaning that, being gradually filled with the treated sludge, an activity that takes place continuously through the pumping station to compensate for the loss of water that is removed, it gives at the end of the process a solid used as a dry material [17]. Therefore, it can be easily removed, disposed of or alternatively reused, for example to shape slopes, etc.

**Fig. 8.** GTX Tube System [17]

## 5. Conclusions

Comparing data obtained from mechanically dewatering sludge on the four types of equipment, the following conclusions can be drawn:

- Centrifuge or vacuum-filter dewatering produces sludge cakes with comparable moisture content;
- Belt filter press dewatering produces sludge cakes with lower moisture content;
- Dewatering of primary fermented sludge is more efficient than dewatering the fermented sludge resulting from the mixture of primary sludge and excess.

It is very important to treat the sludge resulting from wastewater treatment, but it is even more important to find the most efficient method both from an environmental and economic point of view.

#### References

[1] Condorchem Envitech. "Processes and technologies for sludge treatment". Accessed February 10, 2023. https://condorchem.com/en/blog/sludge-treatment/.
[2] Andreoli, C.V., M. von Sperling, and F. Fernandes (Eds.). *Sludge treatment and disposal*. London, IWA Publishing, 2007.
[3] ***. "Introduction to sludge dewatering". June 27, 2021. Accessed February 8, 2023. https://www.sludgeprocessing.com/sludge-dewatering/introduction-to-sludge-dewatering/.

[4] Metcalf & Eddy, Inc., George Tchobanoglous, H. Stensel, Ryujiro Tsuchihashi, and Franklin Burton. *Wastewater Engineering: Treatment and Resource Recovery*. 5th ed. New York, McGraw-Hill Book Company, Inc., 2014.
[5] Ungureanu, Vlad. “Schemes for the processing of sludge from wastewater treatment plants” / “Scheme de prelucrare a namolurilor provenite din stații de epurare a apelor uzate”. Accessed February 3, 2023. https://www.academia.edu/39069593/SCHEME_DE_PRELUCRARE_A_NAMOLURILOR_PROVENITE_DIN_STA%C8%9AII_DE_EPURARE_A_APELOR_UZATE20190509_58896_1952rey.
[6] Vidican, Alin Mihai. “The treatment and processing of sludge from sewage treatment plants” / “Tratarea şi prelucrarea nămolurilor din staţiile de epurare”. Accessed February 6, 2023. https://zdocs.ro/download/tratarea-i-prelucrarea-namolurilor-din-staiile-de-epuraredoc-8pgkrlex746x?hash=6450adf1dd1f2a7135c330a1772a09e3.
[7] Rojanschi, Vladimir, Florina Bran, and Gheorghita Diaconu. *Environmental protection and engineering* / *Protecţia şi ingineria mediului*. 2nd edition. Bucharest, Economic Publishing House, 2002.
[8] Abu-Orf, Mohammed, Robert Junnier, Joshua Mah, and Steven Dentel. “Demonstration of combined dewatering and thermal vacuum drying of municipal residuals.” *Journal of Residuals Science and Technology* 4, no. 1 (January 2007): 25-34.
[9] Cefain Construct. “Robust solid/liquid separation systems. Press filters” / “Sisteme robuste de separare a solidelor/lichidelor. Filtre presa”. Accessed February 8, 2023. http://www.cefain.ro/pdf/Filtre-presa.pdf.
[10] EPA U.S. Environmental Protection Agency. “Fact Sheet: Belt Filter Press”. September 2000. Accessed February 9, 2023. https://www.epa.gov/biosolids/fact-sheet-belt-filter-press.
[11] ***. “Screw presses for sludge dewatering”. June 18, 2020. Accessed February 8, 2023. https://www.sludgeprocessing.com/sludge-dewatering/screw-press/.
[12] S.C. Börger Aquatech S.R.L. “Sludge dewatering” / “Deshidratare namol”. Accessed February 7, 2023. https://borgeraquatech.ro/produse/tratare-namol/deshidratare-namol/.
[13] EPA U.S. Environmental Protection Agency. “Fact Sheet: Centrifuge Thickening and Dewatering”. September 2000. Accessed February 9, 2023. https://www.epa.gov/biosolids/fact-sheet-centrifuge-thickening-and-dewatering.
[14] Caccese, Jim. “How Does a Sludge Dewatering Centrifuge Work?”. *Handex Insights*. August 25, 2021. Accessed February 7, 2023. https://www.hcr-llc.com/blog/is-centrifuge-the-right-choice-for-my-sludge-dewatering-needs.
[15] ***. “What is electro-osmotic dehydration?”. Accessed February 6, 2023. https://lwvworc.org/ro/what-is-electro-osmotic-dewatering.
[16] The International Water Association (IWA). “Sludge Drying Overview - Treatment Methods and Applications”. Accessed February 7, 2023. https://www.iwapublishing.com/news/sludge-drying-overview-treatment-methods-and-applications.
[17] Energeia Nutechsys Ltd. “Dehydration”. Accessed February 9, 2023. http://www.energeianutechsys.it/home/index.php?option=com_content&view=article&id=46&Itemid=116&lang=ro.

# FLUIDAS

## NATIONAL PROFESSIONAL ASSOCIATION OF HYDRAULICS AND PNEUMATICS IN ROMANIA


fluidas@fluidas.ro